

**FEA Study on Strength Optimization of Hybrid Bolted/Bonded Composite Joints**

**Étude par éléments finis sur l'optimisation de la résistance des joints hybrides  
boulonnés/collés en composites**

A Thesis Submitted to the Division of Graduate Studies of the Royal Military College of Canada  
By

2Lt Raphaël Blier

In Partial Fulfillment of the Requirement for the Degree of Master of Applied Science in  
Mechanical Engineering

December 2022

© This thesis may be used within the Department of National Defence but copyright for open  
publication remains the property of the author

# Acknowledgements

I want to acknowledge the financial support provided by the Natural Sciences and Engineering Research Council of Canada (NSERC) and Defence Research and Development Canada (DRDC). Also, I would like to highlight the support provided by the Centre de recherche sur les systèmes polymères et composites à haute performance (CREPEC) which helped me gather the experimental results for this thesis. Finally, I also want to thank Dr. Habib Benabdallah, Dr. Masoud Mehrabian, Dr. Rachid Boukhili and Dr. Kodjo Moglo for their help during the research project.

# Abstract

The joining of composite materials remains challenging as bolted joints, consisting of a bolt, nut and washer assembly, that work well for metallic plates may induce considerable damage at the bolt hole in composite laminates. Bonded joints seem to be a good alternative to bolted joints avoiding potentially induced damage due to drilling of the laminate, as well as stress concentration effects. However, bonded joints are challenging to certify in the aerospace industry due to their considerable variation in performance. Hybrid bolted/bonded (HBB) joints were found to be a good compromise for a fail-safe bonded joint. Nevertheless, optimizing such joints by allowing the bolt assembly (bolt, nut and washer) to contribute to improving the strength rather than for satisfying the fail-safe design constraint requires a deep understanding of the joining mechanisms, such as the stress distribution in the laminate and the adhesive, as well as the interaction between the bolts and the adhesive. This research has permitted a further understanding of the behaviour of HBB joints loaded in tensile shear. Woven fabric carbon fibre reinforced polymer (CFRP) laminates in quasi-isotropic (QI) and cross-ply (CP) configurations were investigated. Using a finite element analysis (FEA) simulation, several critical design factors influencing the composite joint strength, failure conditions as well as load sharing mechanisms were assessed. The stiffness and plastic behaviour of the adhesive was found to be an important factor that defines the transition of the behaviour of the joint from a bolted type, where load sharing is predominant, to bonded. At the same time, the adhesive contributes to a significant decrease of the shear stress concentration factor at the holes in  $0^\circ$  plies. The simulation results confirmed the redundancy of the middle bolt in a 3 bolt joint observed by previous researchers for HBB joints. The load sharing potential, known as an indicator of the joint's performance, is improved by reducing the overlap length, using low stiffness, low yield strength adhesives and thicker laminates in the QI layup configuration. As for the influence of some design parameters of the joint on its strength; it is beneficial to increase the ratio of edge distance to hole diameter, but the increase of the washer size did not appreciably reduce the stress state in the adhesive layer in terms of shear and peel stresses.

# Résumé

L'assemblage de matériaux composites demeure difficile puisque les joints boulonnés, offrant de bonnes performances avec des plaques métalliques, sont non optimaux de par les dommages considérables provoqués aux trous des laminés de composites. Les joints collés semblent être une bonne alternative aux joints boulonnés puisque le laminé est assuré de ne pas être endommagé due au perçage des trous et l'absence de trou dans le laminé enlèvera une source de concentration de contrainte. Toutefois, dans le domaine de l'aéronautique, les joints collés sont difficiles à certifier puisque leur performance varie significativement. C'est pourquoi les joints hybrides boulonnés/collés ont été adoptés, en utilisant les boulons comme une redondance au joint collé. Par contre, l'optimisation de ce type de joint, en vue d'utiliser les boulons de manière plus efficace, demande une compréhension exhaustive des mécanismes des différents types de joint, tels que la distribution des contraintes dans le laminé et l'adhésif, et l'interaction entre l'assemblage boulonné (boulon, écrou et rondelle) et la couche d'adhésif. Des stratifiés de tissus à plis croisés et quasi-isotrope de polymère renforcé par des tissus de fibres de carbone ont été investigués. En utilisant un modèle par éléments finis, plusieurs paramètres de design influençant la résistance des joints de composites, leur mode de défaillance ainsi que leur mécanisme de partage de charge ont été étudiés. Il a été trouvé que la rigidité de l'adhésif ainsi que son comportement plastique est un facteur important définissant la transition entre un comportement similaire au joint boulonné, invoquant un partage de charge, à celui du joint collé. De plus, l'adhésif est identifié comme réduisant considérablement la concentration de contraintes de cisaillements aux trous dans les plis  $0^\circ$  en comparaison avec les joints boulonnés. La simulation a confirmé la redondance du boulon central dans les joints hybrides utilisant 3 boulons tel qu'observé par d'autres chercheurs pour les joints hybrides. La simulation a montré que le potentiel de partage de charge entre l'adhésif et les boulons, identifié par des chercheurs comme étant clé pour augmenter la résistance des joints hybrides, est augmenté pour les conditions suivantes: une distance de chevauchement plus faible, l'utilisation d'un adhésif moins rigide avec une faible limite élastique, une épaisseur de laminé plus épais et l'utilisation d'un stratifié à plis quasi-isotrope. Toutefois, bien que certains facteurs augmentent le potentiel de partage de charge, la réalisation de ce phénomène avant que le dommage soit initié dans le joint est peu probable et difficile. De ce fait d'autres facteurs permettant potentiellement d'augmenter la résistance des joints hybrides sans miser sur le partage de charge. Il a été trouvé qu'une diminution du ratio de la distance du bord extérieur par rapport au diamètre du trou réduit la résistance du joint et qu'une augmentation du diamètre de la rondelle aura un effet négligeable sur l'initiation du dommage dans l'adhésif à moins qu'elle couvre complètement l'extrémité du chevauchement.

# Contents

<b>Acknowledgements</b>	ii
<b>Abstract</b>	iv
<b>Résumé</b>	vi
<b>List of Figures</b>	xi
<b>List of Tables</b>	xii
<b>Nomenclature</b>	xiv
<b>1 Introduction</b>	1
1.1 Overview	1
1.2 Research Objectives and Sub-Objectives	2
1.3 Thesis Organization	3
<b>2 Literature Review</b>	4
<b>3 Theory</b>	7
3.1 Classical Laminate Theory	7
3.1.1 Basic Assumptions	7
3.1.2 Theory Development	7
3.2 Load Transfer Mechanism and Failure Modes in Single-Lap Joints	10
3.2.1 Bolted Joints	10
3.2.2 Bonded Joints	12
3.2.3 Hybrid bolted/bonded joints	13
<b>4 FEA Modelling Approach and Procedure</b>	15
4.1 Joint Geometry	16
4.2 FEA Solution Method and Solution Parameters	16
4.3 Mass Scaling	18
4.4 Contact Definitions	18
4.5 Materials Properties and Damage Modelling	19
4.5.1 CFRP Laminates	19
4.5.2 Modelling of the Bolts and Washers	25
4.5.3 Adhesive	25
4.6 Element Type and Mesh	30
4.6.1 OHT Case	30
4.7 Loading and Boundary Conditions	32
4.7.1 Bolt Clamping Load	33

<b>5</b>	<b>Material Model Calibration and Model Validation</b>	<b>35</b>
5.1	Experimental Procedure	35
5.1.1	Static Tensile Tests	35
5.1.2	Digital Image Correlation Measurements	35
5.2	OHT	36
5.2.1	Longitudinal Strain Field	36
5.2.2	Ultimate Failure Strength	37
5.2.3	Stress concentration Factor at the Hole	37
5.3	3OB and HBB Joints	39
5.3.1	Longitudinal Strain Field in 3OB and HBB Joints	40
<b>6</b>	<b>Design Optimization Study of HBB Joints</b>	<b>43</b>
6.1	Joining Methods Characterization	43
6.1.1	Joining Mechanisms	43
6.1.1.1	Bolted Joints	44
6.1.1.2	Adhesively Bonded Joint	46
6.1.1.3	Hybrid Bolted/Bonded Joints	46
6.1.2	Assessment of The Behaviour of Different Joining Methods	47
6.1.2.1	Out-Of-Plane Displacement for Different Joining Methods	48
6.1.2.2	Longitudinal Strain Field	49
6.1.2.3	Stress Concentration in the Laminate in HBB and 3OB Joints	51
6.1.2.4	State of Stress Comparison in the Adhesive in HBB and Bonded Joints	53
6.1.3	Summary of Effect of Hybridization	58
6.2	Investigation of Design Parameters to Optimize HBB Joints	58
6.2.1	Role of Middle Bolt in 3-Bolts HBB Joints	58
6.2.2	Load-sharing	60
6.2.3	Influence of $e/d$	66
6.2.4	Influence of Washer Size	70
<b>7</b>	<b>Conclusions</b>	<b>73</b>
7.1	Limitations	74
7.2	Recommendations	74
<b>A</b>	<b>Appendix</b>	<b>79</b>
A.1	Model Validation	79
A.2	Abaqus Energy Outputs	80
A.3	Mesh Convergence Studies	81
A.3.1	OHT	81
A.3.2	OB and HBB Joints	81
A.4	Model Energies	83
A.4.1	OHT	83
A.4.2	3OB Joints	83
A.4.3	HBB Joints	84

# List of Figures

1	Laminate and Laminae Coordinate System	7
2	(a) Forces Per Unit Length Acting On the Laminate (b) Moments Per Unit Length Acting On the Laminate	9
3	Load Transfer Mechanisms in Bolted Joints	10
4	Geometric Parameters of Bolted Joints	11
5	Bolted Joint Failure Modes	11
6	Adhesively Bonded Joint Failure Modes	13
7	Shear Stress Distribution in the Adhesive Along the Overlap Length in SLJ	13
8	Specimen Geometry and Dimensions for (a) OHT and (b) 3OB and HBB SLJ	15
9	Geometry of Open Hole Tensile Test Specimen	16
10	Geometry of OB and HBB Joints Specimen a) Side View b) Top View	16
11	Multi-scale Modelling Strategy	20
12	Woven Ply Simplification	21
13	VUMAT Flow Chart	22
14	Araldite® LY 8601/Aradur® 8602 Epoxy System Uniaxial Tensile Stress-Strain Curve	25
15	Linear Drucker-Prager Yield Surface	26
16	Test Assembly Sketch to Measure Back-Strain	27
17	Characteristic Back-Face Strain Curve of SLJ Adherent, Schematic Strain Curve Overall (Left) and in the Overlap Length Range for Different Load Cases (Right)	27
18	Cohesive Surface Positioning	28
19	Linear Traction Separation Cohesive Zone Model	29
20	First-Order Solid Hexahedral Reduced Integration (C3D8R) Elements	30
21	Mesh Plot for the OHT Models	31
22	Mesh Plot for the 3OB Joints	31
23	Mesh Plot for the HBB Joints	31
24	OHT Models Boundary Conditions (Shown for CP Layup)	32
25	OB and HBB Joints Models Boundary Conditions (Shown for QI Layup)	33
26	Nodes (in Red) at Which Reaction Forces Are Extracted	33
27	Washer Thermal Expansion Direction	34
28	Strain Field in the Loading Direction $\epsilon_{xx}$ at 25% of Ultimate Load for OHT CP12 and QI12 Laminates	36
29	FEA and Analytical Normal Stress ( $\sigma_x$ ) vs Y Position in the 0° External Layer For CP Layup OHT Specimen	38
30	Normal Stress Concentration Factor in 0° plies ( $\sigma_x/\sigma_x^\infty$ ) vs Y Position in OHT Models for QI12 and CP12	39
31	Nominal Stress-Displacement Curves for 3OB and HBB Joints, Case of CP Layup	40
32	Nominal Stress-Displacement Curves for 3OB and HBB Joints, Case of QI Layup	40
33	Longitudinal Strain Field for the CP Layup Away From the Washer, Comparison Between DIC Results and Simulation	41
34	Longitudinal Strain Field for the QI Layup Away From the Washer, Comparison Between DIC Results and Simulation	42
35	Joint Model	44
36	Classical Bypass-Bearing Relationship	45
37	Region Monitored for Bolt Load Measurement	46

38	Load-Displacement Curves for QI and CP Joints	47
39	Out-Of-Plane Displacement for Different Joining Method at Various Load Levels	48
40	Scaled Out-Of-Plane Deformation of 3OB and HBB Joints at 8 kN, Case of CP	49
41	Simulation Top Ply Strain Field Comparison Depending on the Joint Configuration, Case of CP Layup	50
42	Simulation Top Ply Strain Field Comparison Depending on the Layup, Case of HBB Joint	51
43	Maximum Longitudinal Stress $\sigma_x$ at the Different Holes in CP Joints	52
44	Maximum Longitudinal Stress $\sigma_x$ at the Different Holes in QI Joints	52
45	Shear Stress $S_{xy}$ in $0^\circ$ Plies for CP12 and QI12 Joints	53
46	Stress Distribution Along the Centerline of the Adhesive Layer for HBB Joint at 8.5 kN	54
47	Stress Distribution in the Laminate and the Adhesive in HBB Joints, Case of CP at 8kN	55
48	Effect of Secondary Bending on HBB Joint, Case of CP-HBB Joint at 8kN (Deformation Scale 50x)	55
49	Peel $\sigma_z$ and Shear Stress $S_{xz}$ Distribution along the Adhesive Edge in QI HBB and Bonded Joints at 12.5 kN	56
50	Comparison of Stresses in the Adhesive Layer for QI and CP HBB Joints	57
51	Comparison of the Out-of-Plane Displacement for QI and CP HBB Joints	57
52	Relative Displacement Between the Laminates for QI and CP HBB Joints	58
53	Tensile $\sigma_x$ and Shear Stress $S_{xy}$ Distribution Around the Critical Hole in CP-HBB Joints at 14 kN	59
54	Peel $\sigma_z$ and Shear Stress $S_{xz}$ at the Overlap Ends in CP-HBB Joints at 14 kN	60
55	Tensile Stress-Strain Curves of the Adhesives Used in the load-sharing Study	61
56	Hole Overclosure for Different Overlap Length and Adhesive	62
57	Peel $\sigma_z$ and Shear $S_{xz}$ Stresses at the Overlap End in CP-HBB Joints Using Araldite® LY 8601/Aradur® 8602 Epoxy at 10 kN	63
58	Hole Overclosure for Different Overlap Lengths and Adhesives	64
59	Hole Overclosure for Different Joint Parameters and Adhesive With an Overlap Length of 114.3 mm	65
60	Longitudinal Elongation of the Critical Hole in HBB Joints For Different Layups	65
61	Out-of-Plane Displacement Near the Free Side in QI-HBB Joints With Different $e/d$ ratio at 12.5 kN	67
62	Peel $\sigma_z$ and Shear $S_{xz}$ Stresses at the Overlap End in QI-HBB Joints at 12.5 kN	67
63	Out-of-Plane Displacement Near the Grip Side in QI-HBB Joints With Different $e/d$ ratio at 12.5 kN	68
64	Effect of Bolt Rotation on QI-HBB Joint with Different $e/d$ Ratio at 12.5 kN (Deformation Scale 30x)	69
65	Tensile $\sigma_x$ and Shear Stress $S_{xy}$ Distribution Around the Critical Hole in QI-HBB Joints at 12.5 kN	70
66	Effect of Bolt Clamping at the End of the Preload Application	70
67	QI12-HBB ( $e/d=2$ ) Large Washer Configuration	71
68	Peel $\sigma_z$ and Shear $S_{xz}$ Stresses at the Overlap End in QI-HBB Joints with Different Washer Sizes at 12.5 kN	71
69	FEA Specimens Geometry Used for the Comparison with the CLT	79
70	Stress-Strain Curve For Different Layups Under Tensile Loading	80
71	Mesh Convergence Study for OHT Models	81



72	Energy Monitoring in OHT Models	83
73	Energy Monitoring in 3OB Joints Models	84
74	Energy Monitoring in HBB Joints Models	84

# List of Tables

1	FEA Unidirectional Laminae Properties	21
2	Equivalent Woven Fabric Properties	22
3	Comparable Prepreg Woven Fabric Mechanical Properties	22
4	Cohesive Surface Properties	29
5	Computational Time of Various Models	32
6	Temperature Gradients Used in the Simulation Process of the Clamping Load	34
7	Stacking Sequence of Studied Specimens	35
8	OHT Ultimate Failure Strength	37
9	Load Distribution Between the Bolts in 3OB Joints	45
10	Failure Load of Different Joint Configurations	47
11	Comparison of OPD Between 3OB and HBB Joints	48
12	Failure Load for Different HBB Joint With and Without Middle Bolts	59
13	Failure Load of HBB Joint Using Araldite® LY 8601/Aradur® 8602 Epoxy for Different Overlap Length	63
14	HBB Joint Failure Load for Various $e/d$ Ratio	66
15	Ply properties of AS4/8552 unidirectional prepreg	79
16	Predicted Material Properties Using CLT	79
17	Mesh Convergence Study at The Overlap Ends in HBB Joints	82

# Nomenclature

Symbol	Signification	Units
$A$	Area	$\text{mm}^2$
$c_d$	Dilatational Wave Speed	m/s
$D$	Damage Variable	-
$d$	Bolt Hole Diameter	mm
$E$	Tensile Modulus	MPa
$e$	Edge Distance	mm
$F$	Material Damage Initiation Parameter	-
$G$	Shear Modulus	MPa
$G_n$	Normal Fracture Energy	$\frac{\text{mJ}}{\text{mm}^2}$
$G_t$	First Shear Direction Fracture Energy	$\frac{\text{mJ}}{\text{mm}^2}$
$G_s$	Second Shear Direction Fracture Energy	$\frac{\text{mJ}}{\text{mm}^2}$
$G_X$	Longitudinal Fracture Energy	$\frac{\text{mJ}}{\text{mm}^2}$
$G_Y$	Transverse Fracture Energy	$\frac{\text{mJ}}{\text{mm}^2}$
$h$	Warp Fibre Area To Total Fibre Area in a Woven Ply Ratio	-
$K_{nn}$	Normal Cohesive Stiffness Coefficient	GPa
$K_{ply}$	Stress Concentration Factor in the Ply	-
$K_{ss}$	First Shear Direction Cohesive Stiffness Coefficient	GPa
$K_{tt}$	Second Shear Direction Cohesive Stiffness Coefficient	GPa
$k$	Torque Coefficient	-
$r$	Hole Radius	mm
$S$	Shear Strength	MPa
$T$	Bolt Preload Torque	Nmm
$T_o$	Original Cohesive Thickness	mm
$t$	Laminate Thickness	mm
$t_k$	Ply Thickness	mm
$t_n$	Normal Traction Stress	MPa
$t_s$	First Shear Direction Traction Stress	MPa
$t_t$	Second Shear Direction Traction Stress	MPa
$V_f$	Fiber Volume Fraction	-
$w$	Specimen Width	mm
$X$	Longitudinal Strength	MPa
$Y$	Transverse Strength	MPa
$z$	Coordinate Along the Z-Axis	mm
$\delta$	Separation	mm
$\delta_t$	Second Shear Direction Separation	mm
$\epsilon$	Strain	-
$\eta$	Benzeggagh-Kenane Coefficient	-
$\kappa$	Curvature	$\frac{1}{\text{mm}}$
$\nu$	Poisson's Ratio	-
$\rho$	Density	$\frac{\text{kg}}{\text{m}^3}$
$\sigma$	Stress	MPa
$\tau$	Shear Stress	MPa

# Index

Symbol	Signification
1	1 Axis
12	1-2 Plane
13	1-3 Plane
2	2 Axis
23	2-3 Plane
3	3 Axis
$C$	Compression
$c$	Critical
$F$	Fill Direction
$f$	Fiber
$L$	Longitudinal
$m$	Matrix
$n$	Normal
$s$	First Shear Direction
$T$	Transverse
$t$	Tension
$w$	Warp Direction
$x$	X Axis
$xy$	X-Y Plane
$xz$	X-Z Plane
$y$	Y Axis
$yz$	Y-Z Plane
$z$	Z Axis

# Acronyms

Abbreviation	Signification
CFRE	Carbon Fiber Reinforced Epoxy
CFRP	Carbon Fiber Reinforced Polymer
CLT	Classical Laminate Theory
CP	Cross-ply
DIC	Digital Image Correlation
FEA	Finite Element Analysis
HBB	Hybrid Bolted/Bonded
OB	Only Bolted
OHT	Open Hole Test
OPD	Out-of-Plane Displacement
QI	Quasi-isotropic
RVE	Representative Volume Element
SB	Secondary Bending
SLJ	Single-lap Joint
UD	Unidirectional
VARTM	Vacuum Assisted Resin Transfer Molding

# 1. Introduction

## 1.1 Overview

Composite materials are increasingly used in aerospace, wind energy harvesting, and civil engineering structures. They have many advantages over their metallic counterparts, such as being light weight, corrosion resistant, fatigue resistant, and more interestingly, they offer the possibility of manufacturing large components as single parts [1]. This last advantage influences the number of elements in a structure. It thus reduces the number of joints, which saves manufacturing time and weight, and reduces the number of discontinuities in the structure. Composite laminates can be manufactured using different types of reinforcement, such as unidirectional (UD), 2D woven fabric, and 3D woven fabric. Woven fabrics are produced by interlacing warp (0-degree) yarns, and weft/fill (90-degree) yarns in a regular pattern called weave style. The mechanical interlocking of the fibres maintains the fabric's integrity. Drape (the ability of a fabric to conform to a complex surface), surface smoothness, and stability of a fabric are controlled primarily by the weave style. Woven fabrics, in general, are easier to handle compared to UD reinforcements which mainly helps during manufacturing [2]. Woven fabrics are also more stable due to the presence of yarns in the warp and fill directions which permits load distribution in the fabric while retaining its original shape [2]. Another advantage of woven fabric is that they are more resistant to impact compared to UD reinforcements [2]. Although they have many benefits, they have the following drawbacks: the yarns must be perpendicular which may reinforce an orientation not subject to high loads, and a reduction of mechanical properties due to the crimps produced by the weave [2, 3]. In many cases, the advantages of impact resistance and ease of manufacturing may offset the slight reduction in mechanical properties that characterize woven fabric compared to UD reinforcements. As such, reinforcement in the form of woven fabric is used in this thesis. Additionally, different types of weave can be used to optimize the laminate performance considering the design requirements. Plain weave is the most commonly used by researchers due to its simple architecture, excellent stability, and good overall performance for simple geometries [2].

Two main joining methods exist: bolted and adhesively bonded joints. Composite bolted joints have the advantage of the ease of assembly, and they facilitate part replacement. Their main disadvantages are the high stress concentrations at the holes and the generation of bearing stresses at the interface between the composite material and the bolt. There is also the increased risk of manufacturing-induced damage by drilling holes in the laminates [4, 5]. On the other hand, adhesive joints generate a more uniform stress distribution; thinner laminates can be used; no drilling of the laminate is required, have a relatively low weight; and they have excellent fatigue resistance [5, 6]. However, adhesively bonded joints suffer significant drawbacks such as sensitivity to manufacturing parameters, environmental conditions, and peel stresses [5]. Also, the assessment of the bond quality remains a problem as non-destructive methods fail to reliably detect all the defects in a bonded joint [5]. This limits a more widespread use of adhesively bonded structural joints. Also, while there are no holes to induce stress concentrations in the laminate, stress concentrations occur at the edge of the overlap in the adhesive layer, which presents a risk for crack formation affecting the performance of the joint.

The alternative presented in this thesis to joining composite laminates through the combination of mechanical and adhesive joining. Hybrid bolted/bonded (HBB) joints combine the advantages of

bolted and bonded joints while mitigating their drawbacks. The adhesive in HBB joints enhances joint efficiency by reducing the stress concentration around the bolt holes [7]. On the other hand, it is believed that the bolts contribute to lowering the peel stresses in the adhesive layer yielding behaviour which increases the joint reliability [7]. If HBB joints are designed as bolted joints with an adhesive layer, the chances that the weight penalty will outmatch the gain in performance are high [5]. Thus, it becomes crucial to fully understand the interaction between the bolts and the adhesive to achieve proper joint designs, which may lead to reliable, high-performance joints.

## 1.2 Research Objectives and Sub-Objectives

The main objective of this thesis was to develop a finite element analysis (FEA) model that simulates the interaction between the adhesive and the bolts in 3-bolt HBB single-lap composite joints under tensile shear loading. The FEA model will facilitate an understanding of the mechanisms of load transfer in different joining methods and a study of the effect of various parameters that may optimize HBB joint design. This research is conducted to provide further insights into the behaviour of bolted/bonded joints made of woven fabric carbon fibre reinforced polymer (CFRP) laminates, which include the critical design factors influencing the composite joint strength, failure conditions as well as load-sharing mechanisms, which would optimize the joining performance of the combined assembly elements. Using an enhanced simulation process, it will be easier, compared to experiments, to conduct a comprehensive study of the failure conditions of such joints. Along with the main research objective, sub-objectives need to be considered in this thesis:

- Assess the simplification of the finite element modelling by using UD laminae to simulate the behaviour of woven fabric tested experimentally.
- Exploit the experimental results in tensile load as well as DIC to confirm the stiffness and strength properties of the material.
- Identify the effect of hybridization on the only-bonded and only-bolted joints.
- Assess the relevance of the middle bolts in joints having relatively long overlap lengths.
- Study the effect of the laminate layup, type of adhesive, overlap length, laminate thickness and edge distance to hole diameter ratio  $e/d$  on the load-sharing potential of the HBB joint.
- Study the effect of  $e/d$  ratio on the adhesive stress state at the overlap ends.
- Study the effect of washer size on the adhesive stress state at the overlap ends.

## 1.3 Thesis Organization

This thesis is divided into 8 Chapters; where the content of each chapter is described below:

- CHAPTER 2: Literature Review
  - A summary of the research done experimentally and through FEA of the tensile behaviour and design optimization of HBB joints.
- CHAPTER 3: Theory
  - A review of the fundamental concepts pertinent to the analysis of HBB composite joints, which includes:
    - \* Classical laminate theory; and
    - \* Load transfer mechanisms and failure modes in bolted, adhesive and HBB composite joints.
- CHAPTER 4: Experimental Procedure
  - A description of the experimental procedure used to produce the experimental results used to validate the FEA models.
- CHAPTER 5: FEA Modelling Approach and Procedure
  - A description of the model parameters that were used for the finite element model. This chapter includes the following:
    - \* Overall approach of the model, including the solving method and assumptions;
    - \* The method of application of bolt preload;
    - \* The material model used, including the material properties;
    - \* The element type and mesh;
    - \* The loading and the boundary conditions;
    - \* The contact interactions; and
    - \* The solution parameters used to complete the analysis.
- CHAPTER 6: Material Model Calibration
  - A review of the material properties calibration process used to validate the accuracy of the FEA model simplification described in Chapter 5. This includes a comparison of OHT specimens for every layup investigated. The validation steps include comparing the ultimate strength, the longitudinal strain field, and the stress concentration at the hole for OHT specimens. The ultimate strength and longitudinal strain field comparison are also made for 3OB and HBB joints.
- CHAPTER 7: Design Considerations for HBB Joints
  - A characterization of 3OB, bonded and HBB joints, highlighting their differences;
  - Study on the influence of the role of the middle bolt in HBB joints;
  - Study on the influence of adhesive properties, overlap length, laminate thickness and layup type on load-sharing in HBB joints;
  - Study on the influence of the  $e/d$  ratio on the adhesive stress state in HBB joints; and
  - Study on the influence of the washer size on the adhesive stress state in HBB joints.
- CHAPTER 8: Conclusion
  - Summary of the work completed and the outcome of the research objective and sub-objectives;
  - Analysis of the model limitations; and
  - Potential future work.



## 2. Literature Review

Hybrid bolted/bonded composite joints (HBB) are an interesting alternative to bolted or bonded composite joints for the reduction of peel stress in the adhesive, the crack-stopping role of the bolts and the stress concentration reduction [8, 7]. Efforts have been made to study HBB joints using simulation techniques and experiments to understand further the behaviours that explain these advantages.

Gamdani et al. [7] investigated experimentally the tensile behaviour of single-lap multi-bolted HBB joints made of cross-ply and quasi-isotropic woven CFRE laminates. They concluded that in 3 in-line bolts joint configurations, it is the outer bolts that limit peel stresses in the adhesive and that the adhesive limits the stress concentration effect around the holes. Their study suggested the middle bolt's possible redundancy and a negligible transfer of load through the fastener. However, they observed that for one and two bolts configurations, the bolts might carry some load after the failure of the adhesive.

Mehrabian and Boukhili [8] have also experimentally investigated hybrid multi-bolted/bonded joints made of cross-ply and quasi-isotropic woven carbon-epoxy composites. They concluded that hybridization produces three positive effects: the reduction of secondary bending and twisting, the relief of stress concentration around the holes, and the delay of damage initiation and thereby the final fracture. They noted that the bolts prevent the debonding of the free end from progressing to the middle section. They observed that the load transfer between the laminates is mainly provided by the adhesive, as the bolts do not contribute significantly in this regard. Even though it was identified that the 3-bolt HBB joint strength is influenced mainly by the adhesive, the advantages of the action of the bolts are also highlighted in comparison to a purely bonded joint.

Bodjona et al. experimentally studied the effect of adhesive layer compliance ( $c$ ) (Eq. 1) on the strength of single-lap hybrid bonded-bolted joints made of prepreg UD quasi-isotropic CFRP tape [9]. They found no benefit in adding a fastener for a bonded joint with a low compliance adhesive. For high compliance adhesive, it is found that the addition of a fastener significantly delays the initial failure. Thus, the fastener's impact depends on the adhesive mechanical and geometric properties.

$$c = \frac{t}{GA} \quad (1)$$

Where  $G$  is the adhesive shear modulus,  $t$  is the adhesive layer thickness, and  $A$  is the bond area.

While [7] and [8] studied the behaviour of HBB joints using only one type of adhesive, in [9] the effect of the adhesive was analyzed experimentally suggested that HBB joints performance are dependent on the adhesive properties.

However, the literature has not achieved a consensus on the performance of hybrid bolted/bonded joints as some report that the joint behaves as a bonded joint since the bolts do not significantly influence the strength of the joint [7, 8, 9]. This shows why researchers became interested in understanding the parameters that can influence the level of interaction between the adhesive and the

bolts. For most researchers, this interaction was seen as load-sharing, which would increase joint performance. Research started mainly with single-bolt hybrid joints and then focused increasingly on multi-bolted hybrid joints. Some noted simultaneous load-sharing between the adhesive and the bolts, while others noted load-sharing but where bolts would bear the load only when the adhesive failed.

Kelly [10] studied the influence of the adherend thickness, the adhesive thickness, the overlap length, the bolt pitch distance and the adhesive modulus on the load-sharing in single-lap single-bolt/bonded hybrid joints made of QI UD CFRP. The study was done through an FEA investigation using Abaqus/Standard, verified by experimental results, using 3D brick elements and included material non-linearity. This research concluded that the load transferred by a bolt is increased for increasing adherend and/or adhesive thickness, and it is also increased for decreasing overlap lengths, bolt pitch distance and/or adhesive modulus.

In another study, Kelly [11] did an experimental investigation complemented by an FEA investigation of a CFRP single-lap HBB joint. He noted that the bolted joint offers inferior performance compared to bonded and HBB joints in terms of strength. He highlighted that bonded and hybrid joints behaved similarly regarding failure initiation at the overlap ends in the adhesive layer. It is mentioned that HBB joints using a stiff adhesive significantly limits the improvements of HBB joint strength compared to bonded joints. However, strength improvements over bonded joints are made for lower modulus adhesives due to load-sharing between the bolt and the adhesive. Thicker laminates also helped increase the maximum strength of HBB joints due to the higher bearing load capacity of thicker laminates.

Bodjona and Lessard [12] also developed an FEA model verified by experimental results to assess the influence of various parameters on load-sharing in single-lap single-bolted/bonded hybrid joints made of UD QI CFRP tape. The analysis was performed using Abaqus. This model used S8R shell elements for the laminates and linear beam elements for the bolts to reduce computational time. The laminates were not considered to suffer damage and followed the CLT. The adhesive non-linear behaviour was modelled using the Drucker-Prager plasticity model. An extensive amount of parameters were considered in this study, targeting mainly geometric and adhesive parameters. This study quantified the relative importance of the various parameters on load-sharing between the adhesive and the bolt. It concluded that the most critical factors affecting load-sharing are the adhesive yield strength, the  $e/d$  ratio, the hardening slope and the adhesive thickness. The edge distance  $e$  is defined as the smallest distance between the center of a bolt hole and the closest edge perpendicular to the load direction. It was also observed that achieving load-sharing at low load levels is challenging as the adhesive will carry most of the load. The previously mentioned research [10, 12] indicated plasticity's importance in load-sharing. When the adhesive was not fully plasticized, no significant proportion of the applied load was transferred by the bolt.

Armentani et al. investigated the structural behaviour of a hybrid (bonded/bolted) single-lap composite joint made of UD prepreg QI CFRE [13]. The study was conducted using Ansys APDL. The adhesive elastoplastic behaviour was modelled using Drucker-Prager yield criterion. 3D solid elements were used for all parts of the model, and the effect of various parameters on the adhesive behaviour and load transfer was monitored. It was concluded that the load transferred by the bolt increases when the strength of the structural adhesive reduces; preload acting on the bolt reduces, and the gap between the bolt's shank and the hole reduces.

While the various research considered adhesive elastoplastic behaviour [12, 13, 10], the effect of plasticity and bolt-hole clearance is seen differently. Armentani et al. [13] concluded that the bolt-hole clearance affects load-sharing without commenting on the effect of adhesive plastic behaviour, while Bodjona and Lessard [12] mentioned that bolt-hole clearance did not significantly impact load-sharing as at the moment where plastic deformation in the adhesive is across the entire overlap length, it cannot support any additional load, thus overcoming the bolt-hole clearance.

Romanov et al. [14] performed a parametric study on the static behaviour and load-sharing of single-lap two-bolt hybrid bonded/bolted composite joints made of QI UD prepreg CFRE through experimental testing complemented by McGill’s in-house design tool Hybrid Joint Engineering Tool (HJET). They studied five geometric configurations with varying overlap lengths, the distance between the bolts, and the edge distance. It was concluded that the major contributors to load-sharing in hybrid bolted/bonded joints are the overlap length and the bolt hole clearance for two-bolt HBB joints (along with a flexible adhesive).

Lopez-Cruz and al. [15] evaluated the effect of several factors quantitatively on the hybrid joint strength by applying the design of experiments (DOE) methodology. They tested experimental single-lap joints with laminates made of CFRP to study the factors of adherend thickness, adhesive modulus, adhesive thickness, clamping area and bolt-hole clearance. Among those factors, it was determined that the adherend thickness, the adhesive mechanical properties and the bolt-hole clearance were the most influential ones for increasing the HBB joint strength. They noted that hybridization offered superior performance to the bonded joint because of its crack arrest capability and it significantly improved its performance compared to bolted joints. It was found that a combination of increasing the adherend thickness, decreasing the adhesive modulus and installing the bolt without clearance should give the higher strength. In the experiments, increasing the clamping area did not significantly influence the maximum strength of the HBB joint.

This literature review permitted to identify some parameters and conclusions as key to this project. Notably, to the author’s knowledge, an FEA study of geometric parameters on 3-bolt HBB joints strength is missing as research focused on the load-sharing phenomenon. The optimization of HBB joints is believed to be achieved mainly by load-sharing. However, it seems to be very difficult to achieve this condition. While this load-sharing phenomenon will be monitored, alternative phenomena will be studied to improve HBB joint performance. Concerning the load-sharing in HBB joints, literature showed that the adhesive plays a significant role. Plasticity is often regarded as key to achieving good load-sharing; thus, it will be included in this project. It was also highlighted that load-sharing in 3-bolt HBB joints is challenging compared to other configurations with fewer bolts. However, this may not be due to the number of bolts but to the longer overlap length of the joint as discussed in [14]. The parameters that will be studied in this thesis to characterize potential design improvements of HBB composite joints are the effect of the  $e/d$  ratio, the overlap length, the laminate thickness, the adhesive properties, the washer size and the layup. This study should characterize whether any simultaneous load-sharing is possible in 3-bolt HBB composite joints and if an alternative configuration is preferred to optimize the design of HBB joints in another way rather than through load-sharing.

# 3. Theory

## 3.1 Classical Laminate Theory

The classical laminate theory (CLT) can be used to perform quick calculations to assess a laminate's behaviour and/or to calculate the stress and strain state in a ply within the laminate. It can also be used to evaluate some in-plane mechanical properties, such as the longitudinal and transverse tensile moduli, the in-plane shear modulus, and Poisson's ratio, knowing each laminae's properties and fibre orientation. The theory development as presented in this section is based on [16]. In this thesis, the CLT is used to calculate the woven fabric properties based on the sub-laminate formed using UD plies as part of the modelling simplification.

### 3.1.1 Basic Assumptions

The CLT is only valid for thin laminates consisting of homogeneous layers. Each lamina is also assumed to be in a state of plane stress and transversely isotropic in directions 2 and 3, as shown in Figure 1. Also, Kirchhoff Hypothesis applies to the theory, and perfect bonding is assumed between the plies [17].

### 3.1.2 Theory Development

The coordinate system, thicknesses and fibre orientation are defined in Figure 1 where 1 is the fibre direction, 2 is the direction perpendicular to the fibres and 3 is the out-of-plane direction.

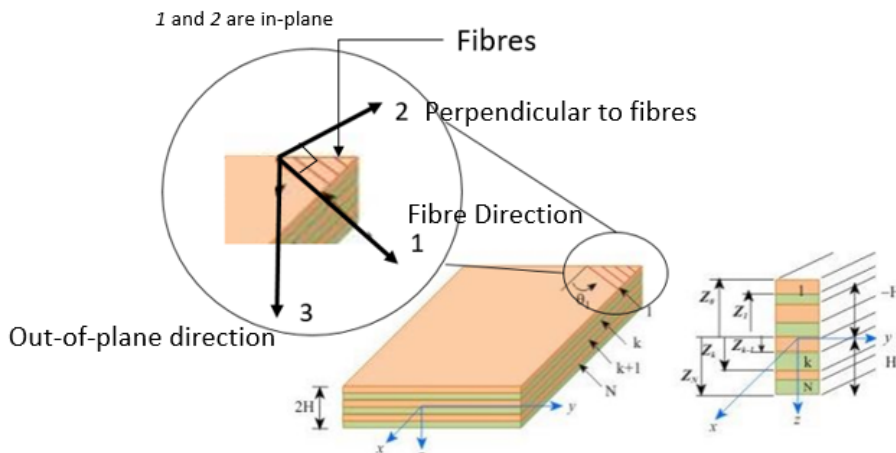


Figure 1: Laminate and Laminae Coordinate System [17]

The main steps outlined by the CLT are summarized hereafter. In order to calculate the laminate properties, the reduced stiffness matrix must be calculated for every ply orientation. The use of the reduced stiffness matrix is only possible when coupled with the plane stress assumption, meaning the stresses  $\sigma_z$ ,  $\tau_{xz}$  and  $\tau_{yz}$  are very small compared to  $\sigma_x$ ,  $\sigma_y$  and  $\tau_{xy}$ . In a joint application, this assumption would not be valid as peel stresses are high, but this CLT is only used in this work to compare the material properties with a woven fabric. First, the reduced stiffness matrix  $[Q]$  is calculated, not considering the ply orientation as shown below.

$$[Q] = \begin{bmatrix} \frac{E_1}{1-\nu_{12}\nu_{21}} & \frac{\nu_{21}E_1}{1-\nu_{12}\nu_{21}} & 0 \\ \frac{\nu_{21}E_1}{1-\nu_{12}\nu_{21}} & \frac{E_2}{1-\nu_{12}\nu_{21}} & 0 \\ 0 & 0 & G_{12} \end{bmatrix} \quad (2)$$

Where,

$$\nu_{21} = \nu_{12} \frac{E_2}{E_1} \quad (3)$$

Where  $E$  is Young's Modulus,  $G$  is the shear Modulus and  $\nu$  is Poisson's ratio.

Then, transformation matrices are required to take into account the ply orientation. The first one is the stress transformation matrix  $[T_\sigma]$ .

$$[T_\sigma] = \begin{bmatrix} m^2 & n^2 & 2mn \\ n^2 & m^2 & -2mn \\ -mn & mn & m^2 - n^2 \end{bmatrix} \quad (4)$$

Where,

$$m = \cos(\theta_1) \text{ and } n = \sin(\theta_1)$$

With  $\theta_1$  being the angle between the identified laminate x-direction and the fibre direction as shown in Figure [1](#)

And the second one is the transformation matrix for engineering strain  $[T_\varepsilon]$  which is shown in Equation [5](#) .

$$[T_\varepsilon] = \begin{bmatrix} m^2 & n^2 & mn \\ n^2 & m^2 & -mn \\ -2mn & 2mn & m^2 - n^2 \end{bmatrix} \quad (5)$$

Where,

$$m = \cos(\theta_1) \text{ and } n = \sin(\theta_1)$$

The on-axis reduced stiffness matrix  $[\bar{Q}]$  can now be obtained using Equation [6](#) .

$$[\bar{Q}] = [T_\sigma^{-1}] [Q] [T_s] \quad (6)$$

Now, the laminate matrix describing its behaviour can be derived. The laminate stiffness matrix can now be calculated using the results from the [A], [B] and [D] matrix which can be calculated using Equations [7](#), [8](#) and [9](#) respectively. The superscript  $k$  denotes the ply number.

$$A_{ij} = \sum_{k=1}^n (\bar{Q}_{ij})_k (z_k - z_{k-1}) = \sum_{k=1}^n (\bar{Q}_{ij}) t_k \quad (7)$$

$$B_{ij} = \frac{1}{2} \sum_{k=1}^n \{ \bar{Q}_{ij} \}_n (z_k^2 - z_{k-1}^2) \quad (8)$$

$$D_{ij} = \frac{1}{3} \sum_{k=1}^n \{ \bar{Q}_{ij} \}_n (z_k^3 - z_{k-1}^3) \quad (9)$$

Using these results, the laminate stiffness matrix  $[ABD]$  can be calculated. Then, using Equation (11), the laminate compliance matrix can be calculated and used in Equation (12) to calculate the mid-plane strains knowing the applied loads. Equation (12) does not consider any moisture or thermal effects. The coordinate system and positive loads used in Equation (12) are shown in Figure 2.

$$[ABD] = \begin{bmatrix} A_{ij} & B_{ij} \\ B_{ij} & D_{ij} \end{bmatrix} = \begin{bmatrix} A_{11} & A_{12} & A_{16} & B_{11} & B_{12} & B_{16} \\ A_{12} & A_{22} & A_{26} & B_{12} & B_{22} & B_{26} \\ A_{16} & A_{26} & A_{66} & B_{16} & B_{26} & B_{66} \\ B_{11} & B_{12} & B_{16} & D_{11} & D_{12} & D_{16} \\ B_{12} & B_{22} & B_{26} & D_{12} & D_{22} & D_{26} \\ B_{16} & B_{26} & B_{66} & D_{16} & D_{26} & D_{66} \end{bmatrix} \quad (10)$$

$$[abd] = [ABD]^{-1} = \begin{bmatrix} a_{11} & a_{12} & a_{16} & b_{11} & b_{12} & b_{16} \\ a_{12} & a_{22} & a_{26} & b_{21} & b_{22} & b_{26} \\ a_{16} & a_{26} & a_{66} & b_{61} & b_{62} & b_{66} \\ b_{11} & b_{21} & b_{61} & d_{11} & d_{12} & d_{16} \\ b_{12} & b_{22} & b_{62} & d_{12} & d_{22} & d_{26} \\ b_{16} & b_{26} & b_{66} & d_{16} & d_{26} & d_{66} \end{bmatrix} \quad (11)$$

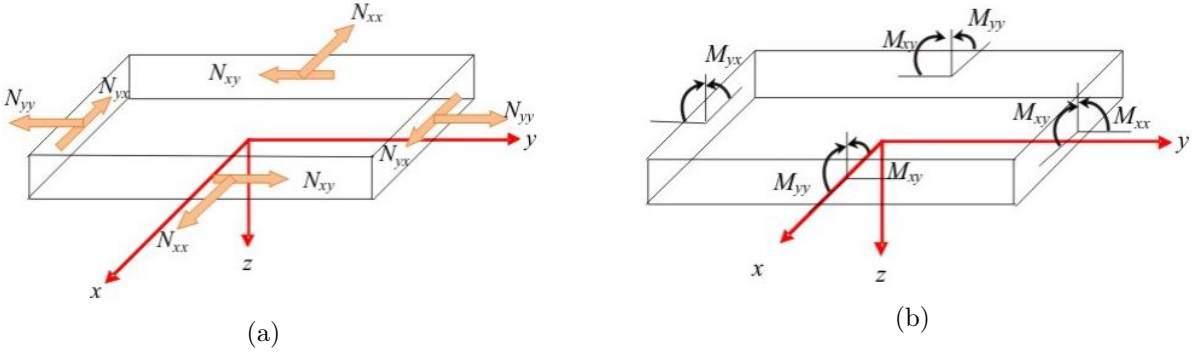


Figure 2: (a) Forces Per Unit Length Acting On the Laminate (17) (b) Moments Per Unit Length Acting On the Laminate (17)

$$\begin{bmatrix} \epsilon_x^o \\ \epsilon_y^o \\ \gamma_{xy}^o \\ \kappa_x \\ \kappa_y \\ \kappa_{xy} \end{bmatrix} = \begin{bmatrix} a_{11} & a_{12} & a_{16} & b_{11} & b_{12} & b_{16} \\ a_{12} & a_{22} & a_{26} & b_{21} & b_{22} & b_{26} \\ a_{16} & a_{26} & a_{66} & b_{61} & b_{62} & b_{66} \\ b_{11} & b_{21} & b_{61} & d_{11} & d_{12} & d_{16} \\ b_{12} & b_{22} & b_{62} & d_{12} & d_{22} & d_{26} \\ b_{16} & b_{26} & b_{66} & d_{16} & d_{26} & d_{66} \end{bmatrix} \begin{bmatrix} N_x \\ N_y \\ N_{xy} \\ M_x \\ M_y \\ M_{xy} \end{bmatrix} \quad (12)$$

Where  $\epsilon_x^o$ ,  $\epsilon_y^o$  and  $\gamma_{xy}^o$  are the laminate mid-surface strains,  $\kappa_x$  and  $\kappa_y$  are the curvatures of the plate due to bending and  $\kappa_{xy}$  is the curvature of the plate due to twisting. Equation (13) can be used to determine the in-plane state of strains for any specific ply in the laminate as a function of its position  $z$ .

$$\begin{bmatrix} \epsilon_x \\ \epsilon_y \\ \gamma_{xy} \end{bmatrix}^k = \begin{bmatrix} \epsilon_x^0 \\ \epsilon_y^0 \\ \gamma_{xy}^0 \end{bmatrix}^k + z_k \begin{bmatrix} \kappa_x \\ \kappa_y \\ \kappa_{xy} \end{bmatrix}^k \quad (13)$$

Generalized Hooke's law is used to find the state of stress according to Equation (14) and (15).

$$\begin{bmatrix} \sigma_x \\ \sigma_y \\ \tau_{xy} \end{bmatrix}^k = \begin{bmatrix} \bar{Q}_{11} & \bar{Q}_{12} & \bar{Q}_{16} \\ \bar{Q}_{12} & \bar{Q}_{22} & \bar{Q}_{26} \\ \bar{Q}_{16} & \bar{Q}_{26} & \bar{Q}_{66} \end{bmatrix}^k \begin{bmatrix} \epsilon_x \\ \epsilon_y \\ \gamma_{xy} \end{bmatrix}^k \quad (14)$$

$$\begin{bmatrix} \sigma_1 \\ \sigma_2 \\ \tau_{12} \end{bmatrix}^k = [T_\sigma] \begin{bmatrix} \sigma_x \\ \sigma_y \\ \tau_{xy} \end{bmatrix}^k \quad (15)$$

## 3.2 Load Transfer Mechanism and Failure Modes in Single-Lap Joints

### 3.2.1 Bolted Joints

In bolted joints, the fasteners are loaded in shear when each composite laminate applies pressure on the bolt shank, which generates bearing loads. When multiple bolts are used, the applied load will distribute among the bolts depending on parameters such as the bolt-hole clearance and the bolt preload [18] [19]. Although part of the load is transferred through bearing contact at each bolt location, the remainder is transmitted through the by-pass region to the other bolts. Another part of the load is transferred through friction at the interface between the laminates, but it is not significant. These load transfer mechanisms (bearing and friction) are depicted in Figure 3.

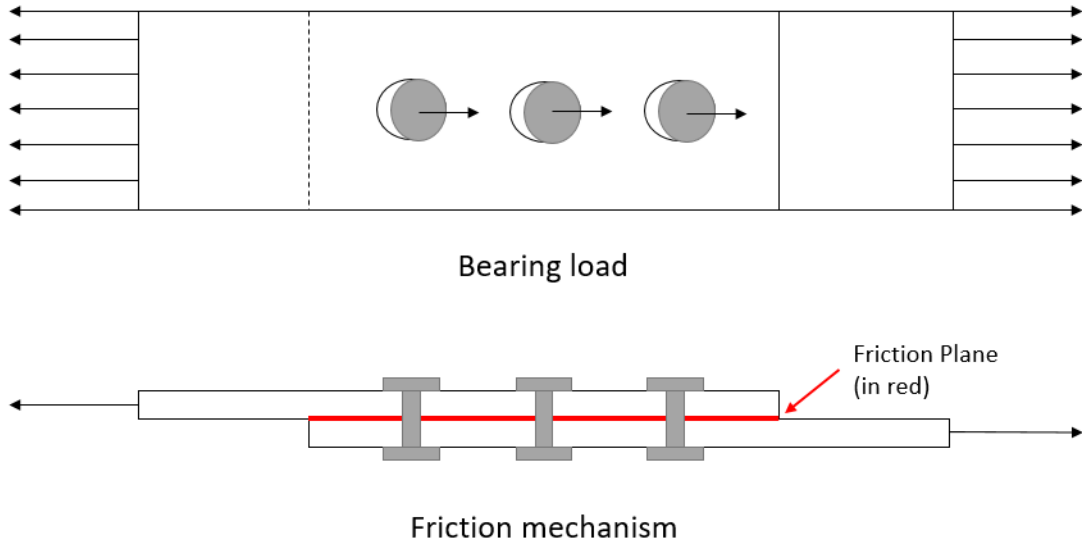


Figure 3: Load Transfer Mechanisms in Bolted Joints

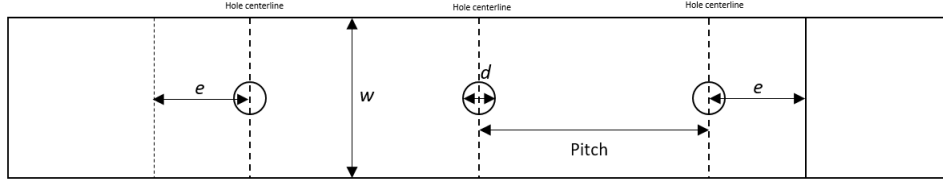


Figure 4: Geometric Parameters of Bolted Joints

Composite bolted joints can fail in multiple ways depending on geometries or parameters such as the edge margin, the bolt pitch, the plate width to bolt hole diameter ratio and the laminate's strength which are depicted in Figure 4. The various failure modes that can be expected in the case of a composite bolted joint are shown in Figure 5.

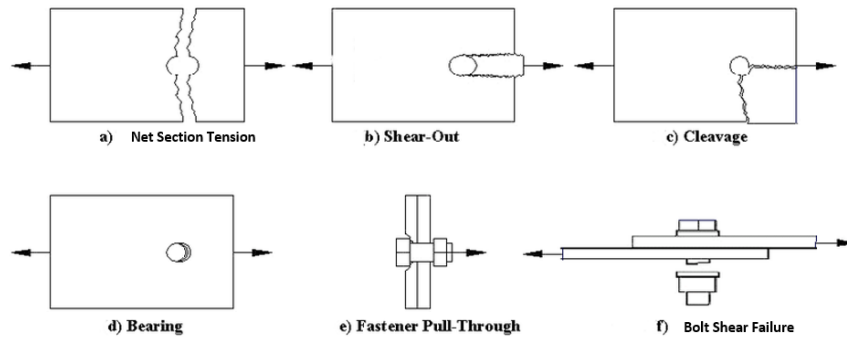


Figure 5: Bolted Joint Failure Modes [20]

The most common failure modes are net section tension and bearing failure. Bearing failure is often preferred as the first anticipated damage since it can be detected during regular inspections, thus preventing catastrophic failure.

Net section tension (Fig. 5a) is defined as a fracture of the laminate initiating at the hole and developing perpendicular to the loading direction due to the tensile stress exceeding the tensile strength of the material. This is a catastrophic failure mode causing a loss of integrity of the joint. The most influential parameters causing this type of failure are the hole diameter to plate width ( $d/w$ ) ratio, the number of bolts in a row and the layup stacking type, as these three parameters directly influence the load carrying capability of the joint. The layup type was found to influence the notch sensitivity which also applies to holes, negatively impacting the joint resistance against net-section tension failure [8].

The shear-out failure (Fig. 5b) occurs as there is not enough material, relative to its shear strength, behind the fastener to sustain the load being applied by the fastener's shank on the laminate. This failure mode depends on the edge distance and the layup type. A quasi-isotropic layup with reinforcement in the  $\pm 45^\circ$  directions is more resistant to shear-out than a cross-ply laminate.

Cleavage (Fig. 5c) is a mixed-mode failure mode that consists of a mix between net tension and shear-out failure. For some parameters, such as the  $w/d$  ratio, there is a transition point where failure mode switched between net tension and shear-out failure. Cleavage is susceptible to occur



around this point of transition.

Bearing failure (Fig. 5d) is defined as the compressive failure of the laminate as pressure is applied by the bolt shank on the laminate. The type of layup, the bolt diameter, the laminate thickness and the laminate width.

The bolt pull-through (Fig. 5e) may occur during in-plane loading of single-lap joint (SLJ) as the eccentricity induces a bending moment generating a pull-out effect of the assembly.

Bolt shear failure (Fig. 5f) happens when the load transferred by the fastener exceeds its shear strength; the load redistribution can then trigger the failure of the other fasteners.

### 3.2.2 Bonded Joints

In bonded joints, the adhesive layer transfers the load as it develops internal shear forces to resist the shear displacement between the adherends. However, for SLJ, shear is not the only type of stress developing in the adhesive. As the load is transferred through the joints, severe peel stresses take place in the adhesive due to secondary bending caused by the offset in the load path in the bonded plates [1].

The types of failure modes for composites adhesively bonded joints are shown in Figure 6. Similar to bolted joints, fracture can occur in the laminate due to tensile stresses exceeding tensile strength of the material (Fig. 6a). Additionally, due to nature of CFRP being formed of the stacking of laminae, high shear stresses develop between the different plies, which can induce delamination (Fig. 6b). It is important to note that cohesive failure refers to a rupture of the adhesive layer. This can occur due to shear (Fig. 6c) but also peel (Fig. 6d) stresses developing in the adhesive. Shear stresses are induced by the relative displacement between the laminates and peel stresses originate from the secondary bending induced by eccentricity in the load path. The last failure mode characterizing bonded joints is adhesive bondline fracture. This failure mode defines fracture at the laminate-adhesive interface and similarly to cohesive failure, it can be triggered by shear (Fig. 6e) or peel stresses (Fig. 6f). The failure of the bondline largely depends on the surface preparation during the joint manufacturing process [21]. It was found that higher surface energy of the adherend would improve adhesion at the bondline [22]. Various processes are recommended for that effect, such as the use of peel plies, abrasion, media blasting, and plasma technics. Although peel plies offer great consistency, they usually do not produce the highest surface free energy value, leading to poor performance of the joint [23]. The abrasion process has the risk of generating exposure of the fibres and, as such, would weaken the structure of the laminate while simultaneously reducing the adhesion potential [23]. Media blasting can produce a high energy surface but generates a lot of debris compared to the other methods [23]. However, the induced damage to the outer ply of the laminate would potentially trigger the premature failure of the adherend. The plasma method is another commonly used method for surface treatment. Atmospheric air plasma produces the best surface free energy value and shows a desirable consistency while being costly [23]. Thus, surface preparation requires numerous considerations when manufacturing a composite bonded joint, as this will significantly affect the strength of the bonded joint.

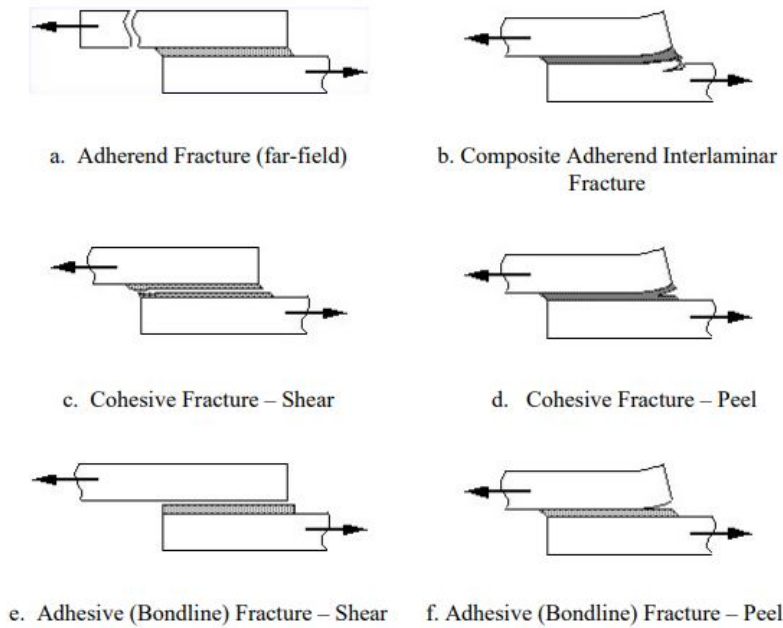


Figure 6: Adhesively Bonded Joint Failure Modes [21]

The overlap ends are critical regions of the adhesive where stress concentrations occur, generating failure by either shear stress, peel stress or a combination of the two, specifically in the case of an eccentric load path. This is demonstrated by Figure 7, which shows the shear stress distribution at the mid-thickness plane of the adhesive layer for two adhesives used in bonded joints. In addition, stress peaks are apparent at the stress-concentrated regions at the overlap ends for single-lap joints (SLJ). This phenomenon is reduced for low-stiffness adhesives such as Sikaflex 256, but it is not used in high-performance structural joints.

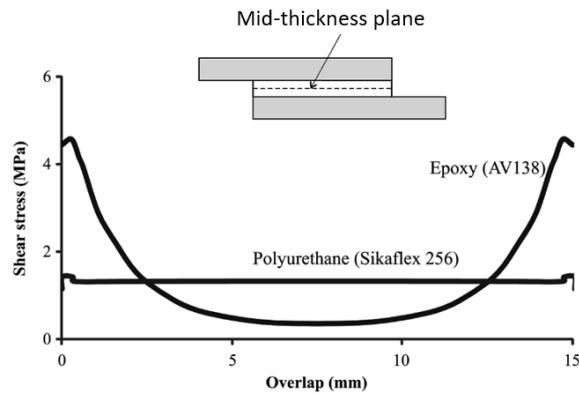


Figure 7: Shear Stress Distribution in the Adhesive Along the Overlap Length in SLJ [24]

### 3.2.3 Hybrid bolted/bonded joints

Although the benefits of combining the two basic methods of joining have been proven, research is still progressing to better understand the load-sharing process between the fasteners and the adhesive. Some researchers have noted negligible sharing among them [8, 7], while others have indicated that proper load-sharing can be achieved at medium to high loads [10, 12, 13, 14]. In

the absence of load-sharing, failure of the joint is triggered by the adhesive failure, while the bolts do not play any significant role in the load-sharing process. The present research tries to elucidate the interaction between the bolts and the adhesive in these joints while investigating the failure mechanisms.

## 4. FEA Modelling Approach and Procedure

The specimen geometries used to create the 3D simulation models of OHT, OB and HBB configurations are shown in Figure 8. Sandpaper is used to reduce the slippage of the specimens upon loading. Additionally, doublers made of the same composite material, is used for the joint such as the joint can be aligned properly on the traction machine. These doublers were glued to the specimens. These areas were discarded from the simulation to reduce computational time. An average laminate thickness of 2.6 mm was measured on the experimental specimens. The specimen type: open hole test (OHT), only-bolted (OB) and hybrid bolted/bonded (HBB) is added to the laminate code, e.g. CP12-HBB or QI12-OHT, to specify the class of configurations. For example, a 12-ply cross-ply layout will be referred to as CP12. The geometries are purely based on the available experimental results which used specimen geometries following ASTM standards. To maintain the focus of this study on the characterization of HBB joints and on the HBB joint strength enhancement parametric study, it has been determined that the use of a simple geometry was preferable to avoid modelling and behaviour complexities.

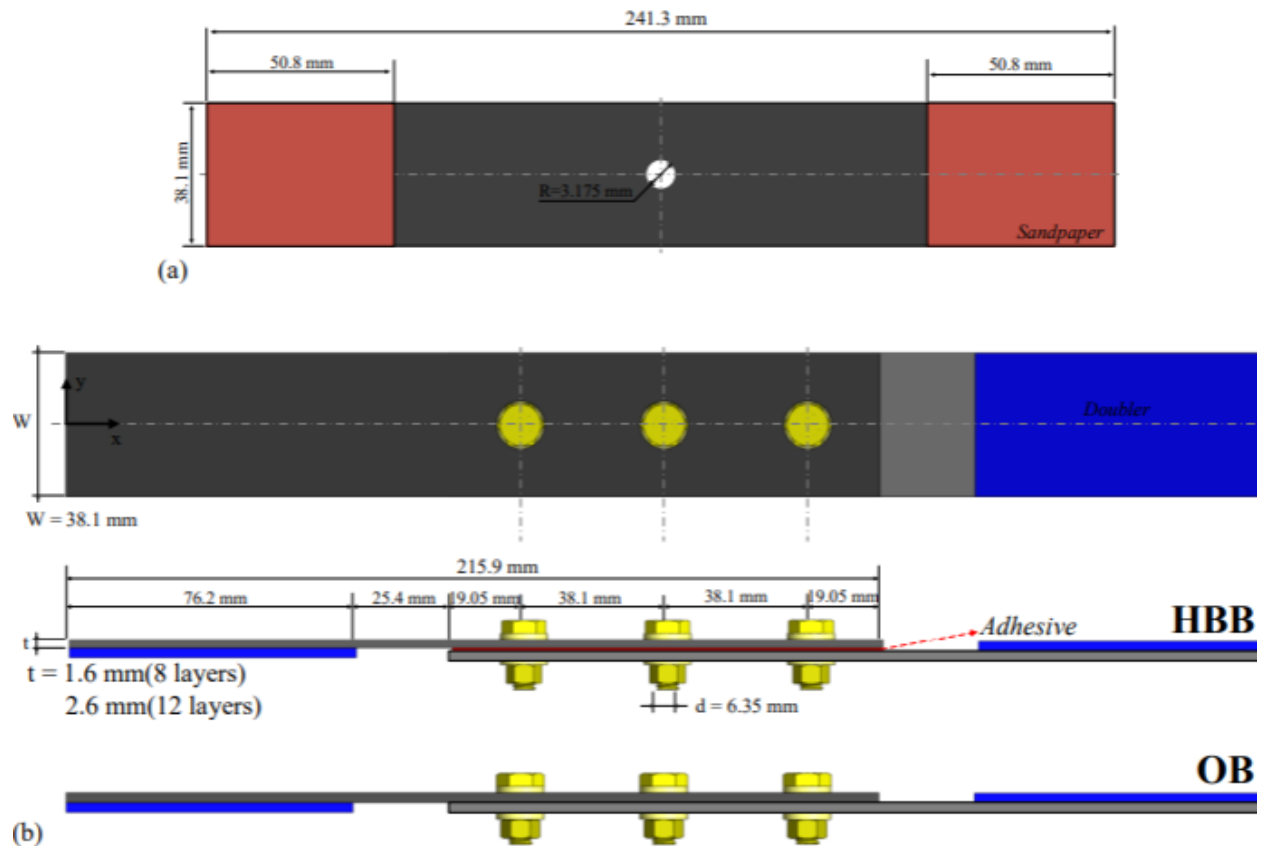


Figure 8: Specimen Geometry and Dimensions for (a) OHT and (b) 3OB and HBB SLJ

### 4.1 Joint Geometry

QI layup geometries are modelled as complete geometries because of ply angles. Cp makes use of symmetry because all plies in a CP layup are either at 0° or 90°. As such, planes of symmetry can be defined with respect to the X-Z plane and Y-Z plane. The difference can be observed in Figure 9 for OHT models and Figure 10 for OB and HBB models. The geometries were partitioned around the holes to help produce a high mesh quality. Also, in OB and HBB joints, the bolts were modelled as one component where the head and the nut are assumed to have identical geometries. The washers were also modelled as they are used to apply a compressive preload of the joints. More details are provided in Section 4.7.1.



Figure 9: Geometry of Open Hole Tensile Test Specimen

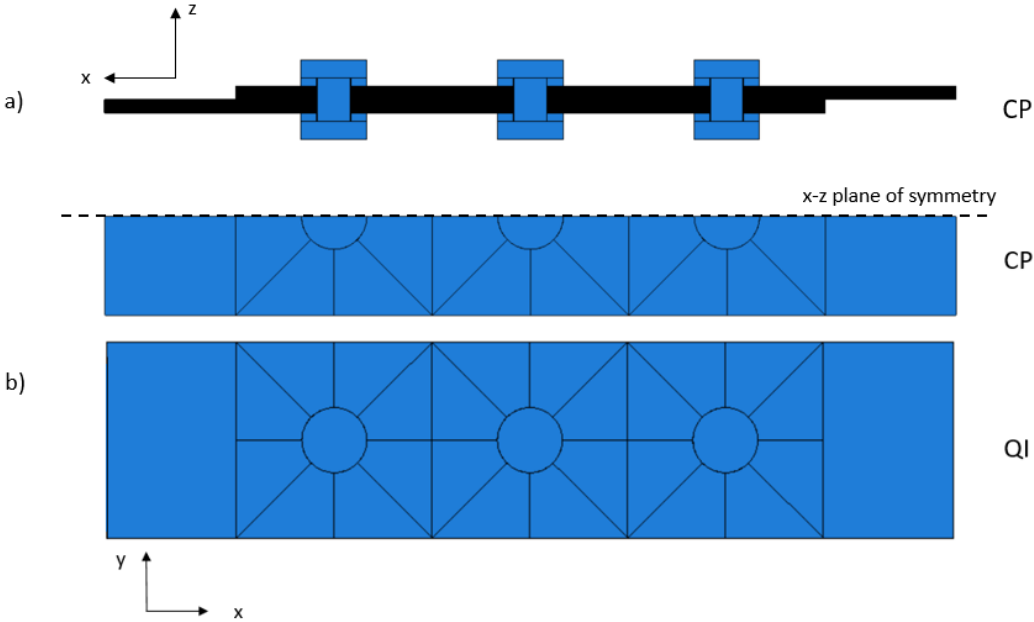


Figure 10: Geometry of OB and HBB Joints Specimen a) Side View b) Top View

### 4.2 FEA Solution Method and Solution Parameters

An explicit non-linear model was used for this analysis as large deformations occur at failure, multiple contacts are defined and damage evolution is included in the analysis. The FEA simulations

were run using Abaqus/CAE 2019. An implicit solver is usually the preferred way of simulating static and quasi-static loading as it is usually more computationally efficient than the explicit solver. However, when damage occurs in the material, the use of the implicit solver becomes much more complex, and convergence problems may arise. Researchers using the implicit solver have defined the failure condition as the instant when the simulation crashes, preventing the solver from converging in many cases [25] [26]. This means that the complete failure might not have been observed due to ill-conditioned solutions of that damage propagation state. Also, a higher number of iterations becomes necessary as damage progresses, making the implicit solver less computationally effective compared to the explicit solver [27]. These problems are not encountered with the explicit solver as it advances the previous increment's kinematic state, without any convergence requirement, which is preferred for quasi-static analysis [26] [28].

The explicit solver requires that energies be monitored to ensure that the simulation remains in a quasi-static state and, more specifically, that kinetic energy does not influence the results uncontrollably. Also, overshoots in terms of material behaviour response are expected due to the nature of the explicit solver, which has to be taken into account when considering minor discrepancies in the results. Overshoots occur as the material behaviour is derived for the next increment in terms of an extrapolation of the current time increment rather than solving the equation systems for equilibrium in the next time increment. The overshoots are usually more predominant at lower load levels when the mass of the component is accelerated from a static state to motion. Nevertheless, due to the energy monitoring and the choice of small time increments, those overshoots remained relatively small at higher load levels, where meaningful results are obtained. The stable time increment must be reduced if premature damage occurs due to a significant overshoot.

For the OHT models, the simulation was run as one step consisting of the tensile test. For the joints, a bolt preload had to be applied. As such, the simulation were run using two steps; the first one being the bolt preload application, and the second one corresponding to the tensile test.

The simulation ran over the real-time period of the actual experimental tests. Due to the long time period required for the explicit step to emulate the displacement rate of the experimental set-up, the mass scaling technique was used to increase the time increments, thus reducing the calculation time. Mass scaling can be performed by scaling the masses of all specified elements by a user-supplied constant factor or scaling the masses of all specified elements by the same value so that the minimum stable time increment for any element in the element set is equal to a user-supplied time increment [29].

In this case, mass scaling was applied so that the scaling value is adapted throughout the step to match the user-supplied time increment. This adaptation throughout the step was required as elements deform and some fail, changing the value of the critical element length during the simulation. The OHT models were set to scale to a target time increment of 1E-04 seconds, updated every 10 increments, while the 3OB joints were set to a time increment of 6E-05 seconds, and HBB joints were set a time increment of 1.2E-04 seconds.

To determine if these mass scaling parameters altered the quasi-static nature of the simulation, the total strain energy (ALLIE) and kinetic energy (ALLKE) were monitored throughout the simulation. For a given system, ALLIE is expected to increase as the model absorbs energy when loaded. On the other hand, ALLKE should be very low as a quasi-static test is represented by the simulation. Any significant presence of ALLKE would mean the model is in a dynamic state, which would not accurately represent the quasi-static nature of the experimental test. It was determined

that ALLKE must remain under 5% of ALLIE to consider the quasi-static results unaffected by dynamic phenomenon [30]. The mass scaling parameters shown above proved reasonable as kinetic energy (ALLKE) remained negligible until failure, meaning the model remained in a quasi-static state. A detailed definition of the various types of energies monitored is given in Appendix A.2. The energy plots for each model are shown in Appendix A.4.

### 4.3 Mass Scaling

Conducting a simulation with the explicit algorithm is an excellent alternative to the implicit solver mainly because of its ability to mitigate convergence problems. However, to obtain this stable state, a very small time increment must be used in comparison with an implicit solver [27]. The stability limit is influenced by the minimum element characteristic length  $L_{\min}$  and the dilatational wave speed in the element  $c_d$ . Equation (16) is used by Abaqus to calculate the stable time increment, which corresponds to the stable time increment of the most limiting element in the model [29].

$$\Delta t = \min \left( \frac{L_{\min}}{c_d} \right) \quad (16)$$

The dilatational wave speed in the element is proportional to the square root of the ratio between the element's Young's Modulus and the material density assigned to a specific element, as shown in Equation (17) [29].

$$c_d \propto \sqrt{\frac{E}{\rho}} \quad (17)$$

Since the simulation accuracy must not be decreased to accelerate the solution time, the Young's Modulus must remain the same as the actual test specimen. Thus, the density is the only parameter that can be changed to speed up the simulation considering the material behaviour is rate dependent and that the coarsest mesh for which results have converged is used. Instead of adjusting the density manually, Abaqus can scale the density of the critical elements such as the stable time increment is increased [29]. When a mass scaling definition is created in the software, it will automatically artificially increase the density of the elements that do not initially satisfy the target time increment. This will lead to a larger stable time increment, meaning the solver will require fewer steps to complete the simulation, reducing the computational time. However, this method must be used with caution not to induce significant dynamic effects in the quasi-static analysis. Additionally, by increasing artificially the mass of the elements, the dilatational wave speed is reduced. Yet, the ratio of deformation speed to the dilatational wave speed must remain under 0.3 as above this threshold, purely mechanical material constitutive relationship is no longer valid and a thermo-mechanical equation of state material is required [29].

### 4.4 Contact Definitions

In the bolted joint assembly and the hybrid bolted/bonded joint models, contact definitions had to be implemented to simulate the interface regions between the joint components. Abaqus/Explicit has two contact algorithms to define contact in the simulation: general contact and contact pairs [29]. Usually, the general contact algorithm is more powerful and imposes fewer restrictions to contact definition than the contact pair algorithm [31]. General contact is also faster in terms of calculations and, thus, in an attempt to reduce computational time, useful when defining multiple contacts in a simulation. Also, when considering damage and, more specifically, element deletion,

general contact is superior because contact will be established between any elements in the simulation, while the contact pair algorithm can only define contact between the specified initial surfaces. If an element is deleted, contact will not be established with the next closest active element when using contact pairs [31].

For the bolted joints, the general contact algorithm was used for bolt to washer, bolt to hole of the laminate, washer to laminate and laminate to laminate contact interactions. Every interaction was defined using a penalty friction model and hard contact definition for the pressure-overclosure relationship to minimize the penetration of the surfaces in contact. The friction coefficients used are 0.7, 0.1 and 0.5 for laminate to laminate, bolt/washer to laminate and bolt to washer interactions respectively [32].

For the hybrid bolted/bonded models, general contact is used for all contact interactions, namely bolt to washer, bolt to laminate and adhesive to adhesive contact. The same interaction parameters selected for the bolted joint are used for these models. The only difference is the contact between the adhesive layer where a cohesive interaction was defined. No adhesive bondline failure was defined due to the variability in results, the high dependency on surface preparation and the lack of experimental data. As such, the bondline was assumed to be perfect, and the adhesive layer was modelled as part of the laminate. The properties of the cohesive interaction and the assigned behaviour are detailed in Section 4.5.3.

## 4.5 Materials Properties and Damage Modelling

### 4.5.1 CFRP Laminates

The technique usually used to properly model the woven architecture is based on a representative volume element (RVE) which is repeated to form the structure, a technique also called the multi-scale approach where the fibres or yarns are modelled as well as the matrix at the micro-scale [33, 34, 35, 36]. A schematic representation of this strategy is shown in Figure 11 for the case of UD plies with fibres oriented at a  $10^\circ$  angle in an off-axial tensile test. The fibres and the matrix are modelled with a voxel mesh which is similar to a pixel but for the 3D space. This allows an accurate discretization of a component at a very small scale (particles). Then, this repetitive cell is used to represent a single lamina of a laminate. Thus, macro-scale strains (laminate scale) are converted to the micro-scale (RVE scale) at which the material response at every integration point is computed before converting this information to the macro-scale level for computing the state of stress in the structure [37, 38]. This method can be used to model woven fabric, but at a high computational cost [37]. The same process is used for woven fabric, with the micro-scale representing the particular architecture of this type of reinforcement. Instead of having all the fibres parallel, they are stacked together as yarns intertwined with other yarns to form the warp.



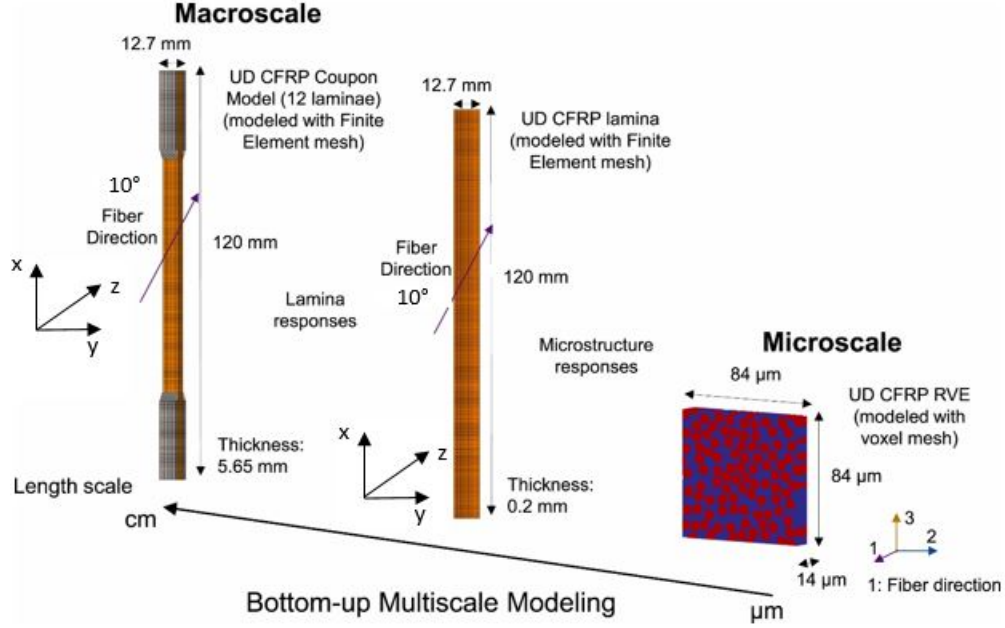


Figure 11: Multi-scale Modelling Strategy [37]

Due to the high computational cost of this modelling strategy, another approach will be used for this research. One potential option is to treat the plies as having anisotropic properties similar to those of a prepreg fabric (similar longitudinal and transverse in-plane stiffness and strength), with the drawback of a poor representation of the interaction between the fibres and the matrix. In addition, the characterization of the damage evolution in the layer would be challenging, as it would be difficult to express the stiffness degradation due to damage since there is no dominant mechanical properties contributor like in the case of unidirectional plies for which the fibres dominate the longitudinal direction and the matrix dominates the transverse direction.

Since stress concentrations arise in joints around the bolt holes, damage evolution is essential to the simulation because the material can sustain a certain amount of damage before complete failure. The other option is to model the fabric using a technique discussed by Gordon [39] which consists of substituting one fabric ply with 4 UD plies to form a symmetric sub-laminate, then stacked together to form the woven fabric laminate. This technique of replacing fabric layers with UD plies has been used by other researcher [40] [41]. Also, the sub-laminate formed by the 4 UD plies will have the same thickness as the fabric, but the thickness ratio of the ply will comply with Equation (18) as suggested by [39].

$$h = \frac{A_w}{A_F + A_w} \quad (18)$$

Where,  $A_w$  is the warp fibre area, and  $A_F$  is the fill fibre area.

Since the fabric is a plain weave, it has the same amount of fibres in the fill and warp directions. Thus,  $h$  is equal to 0.5, and as such, each UD ply has the same thickness equivalent to 1/4 of the thickness of a woven fabric ply, as shown in Figure 12. Thus, in the simulation, every woven ply was modelled by 4 UD plies.

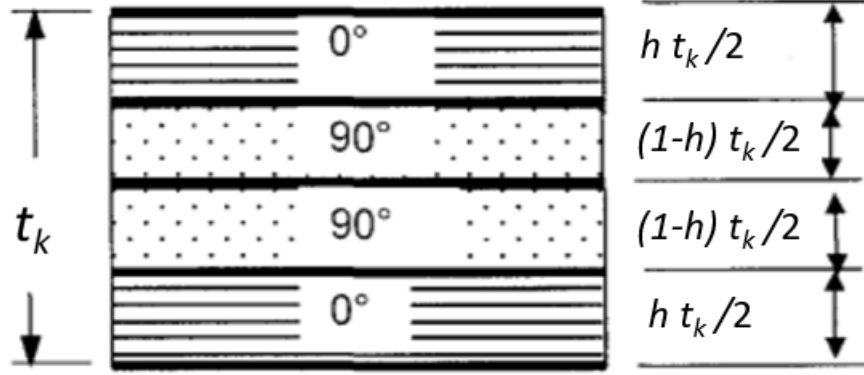


Figure 12: Woven Ply Simplification [39]

The material properties used in the FEA model for the unidirectional plies are shown in Table 1. They were obtained according to a developed procedure called material properties calibration, discussed in Chapter 5. Out-of-plane properties were assumed to be the same as those in the transverse direction as they are driven by the matrix. Using the classical laminate theory, it was possible to calculate the equivalent in-plane mechanical properties for a woven fabric, which are reported in Table 2.

Table 1: FEA Unidirectional Laminae Properties

Property	Units	Value
$t_{ply}$	mm	0.05417
Density	kg/m <sup>3</sup>	1800
$E_1$	GPa	100
$E_2 = E_3$	GPa	7
$G_{12} = G_{13} = G_{23}$	GPa	4
$\nu_{12} = \nu_{13}$	-	0.3
$\nu_{23}$	-	0.35
$X_t$	MPa	1150
$X_c$	MPa	1000
$Y_t$	MPa	54
$Y_c$	MPa	250
$S_L = S_T$	MPa	110
$G_{Xt}$ [42]	$\frac{mJ}{mm^2}$	91.6
$G_{Xc}$ [42]	$\frac{mJ}{mm^2}$	79.9
$G_{Yt}$ [42]	$\frac{mJ}{mm^2}$	0.22
$G_{Yc}$ [42]	$\frac{mJ}{mm^2}$	1.1

Where  $X_t$  is the fibre tensile strength,  $X_c$  is the fibre compression strength,  $Y_t$  is the matrix tensile strength,  $Y_c$  is the matrix compression strength,  $S_L$  is the shear strength,  $G_{Xt}$  is the fibre fracture energy in tension,  $G_{Xc}$  is the fibre fracture energy in compression,  $G_{Yt}$  is the matrix fracture energy in tension,  $G_{Yc}$  is the matrix fracture energy in compression.

Table 2: Equivalent Woven Fabric Properties

Property	Units	Value
$E_x$	GPa	53.8
$E_y = E_z$	GPa	53.8
$G_{xy}$	GPa	4
$\nu_{xy}$	-	0.0393

For comparison, Table 3 shows some mechanical properties of commercial prepreg woven fabrics similar to those used to manufacture the test coupons for which the data were unavailable.

Table 3: Comparable Prepreg Woven Fabric Mechanical Properties [43]

Product Name		SOLVAY COM® 50%-1KT300-P-120	CY- 977-6- 120	HEXCEL Ply® F593	Hex- W3T282-42
Fibers		T300		T300	
Resin		CYCOM® 977-6		F593 Epoxy	
$V_f$	%	42.7		49	
$E_x$	GPa	53		56.5	
$G_{xy}$	GPa	3.9		N/A	

An improved Hashin damage initiation criterion is used to model the damage initiation condition of the individual laminae. These damage initiation criteria and the damage evolution laws were programmed using a user-defined subroutine (VUMAT) for predicting four damage initiation modes, which are: tensile fibre damage initiation, compressive fibre damage initiation, tensile matrix damage initiation, and compressive matrix damage initiation. A flowchart of the VUMAT subroutine is shown in Figure 13.

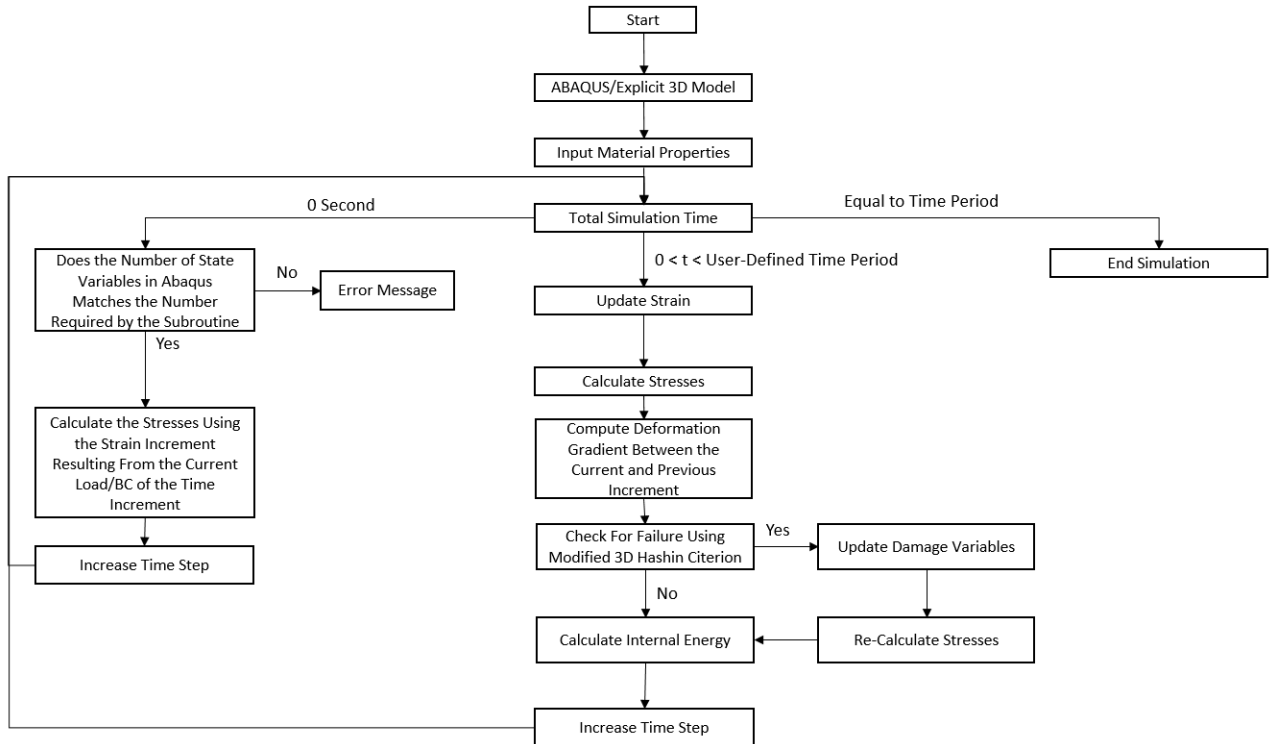


Figure 13: VUMAT Flow Chart

As the epoxy used for the matrix is qualified as brittle the plastic behaviour of the matrix itself is neglected. The damage initiation criteria were implemented according to the following governing equations [26].

Tensile fibre damage initiation criterion for  $\varepsilon_1 \geq 0$ :

$$F_{ft}^2 \geq 1.0 \quad (19)$$

$$F_{ft}^2 = \left( \frac{\varepsilon_1}{\varepsilon_{1t}^f} \right)^2 + \left( \frac{\gamma_{12}}{\gamma_{12}^f} \right)^2 + \left( \frac{\gamma_{13}}{\gamma_{13}^f} \right)^2 \quad (20)$$

Compressive fibre damage initiation criterion for  $\varepsilon_1 < 0$ :

$$F_{fc}^2 \geq 1.0 \quad (21)$$

$$F_{fc} = -\frac{\varepsilon_1}{\varepsilon_{1c}^f} \quad (22)$$

Tensile matrix damage initiation criterion for  $\varepsilon_2 + \varepsilon_3 \geq 0$ :

$$F_{mt}^2 \geq 1.0 \quad (23)$$

$$F_{mt}^2 = \left[ 1 - \left( \frac{\varepsilon_{2t}^f}{2\gamma_{23}^f} \right)^2 \right] \frac{(\varepsilon_2 + \varepsilon_3)^2}{\varepsilon_{2t}^f} + \left( \frac{\varepsilon_2 + \varepsilon_3}{2\gamma_{23}^f} \right)^2 - \frac{\varepsilon_2\varepsilon_3}{(\gamma_{23}^f)^2} + \left( \frac{\gamma_{12}}{\gamma_{12}^f} \right)^2 + \left( \frac{\gamma_{13}}{\gamma_{13}^f} \right)^2 + \left( \frac{\gamma_{23}}{\gamma_{23}^f} \right)^2 \quad (24)$$

Compressive matrix damage initiation criterion for  $\varepsilon_2 + \varepsilon_3 < 0$ :

$$F_{mc}^2 \geq 1.0 \quad (25)$$

$$F_{mc}^2 = \left[ \left( \frac{\varepsilon_{2c}^f}{2\gamma_{23}^f} \right)^2 - 1 \right] \frac{(\varepsilon_2 + \varepsilon_3)^2}{\varepsilon_{2c}^f} + \left( \frac{\varepsilon_2 + \varepsilon_3}{2\gamma_{23}^f} \right)^2 - \frac{\varepsilon_2\varepsilon_3}{(\gamma_{23}^f)^2} + \left( \frac{\gamma_{12}}{\gamma_{12}^f} \right)^2 + \left( \frac{\gamma_{13}}{\gamma_{13}^f} \right)^2 + \left( \frac{\gamma_{23}}{\gamma_{23}^f} \right)^2 \quad (26)$$

Where,

$$\begin{aligned}\varepsilon_{1t}^f &= \frac{\sigma_{1t}}{E_1} & \varepsilon_{2t}^f &= \frac{\sigma_{2t}}{E_2} & \gamma_{12}^f &= \frac{\tau_{12}}{G_{12}} & \gamma_{23}^f &= \frac{\tau_{23}}{G_{23}} \\ \varepsilon_{1c}^f &= \frac{\sigma_{1c}}{E_1} & \varepsilon_{2c}^f &= \frac{\sigma_{2c}}{E_2} & \gamma_{13}^f &= \frac{\tau_{13}}{G_{13}}\end{aligned}$$

When damage initiation is detected, damage evolves at the integration point following an exponential evolution scheme corresponding to the damage mode (i.e. fibre tensile damage, fibre compression damage, etc.) as shown in Equation (27) to (30). This prevents sudden instability in the model and represents more realistically a gradual stiffness loss of the laminate due to damage. From these, the global fibre  $D_f$  and matrix  $D_m$  damage variables are calculated [26, 44]. Prior to damage initiation, those variables are set to zero. Also, the coding also applied a specific condition prohibiting material regeneration, which would take the form of decreasing the level of damage as the simulation progresses.

$$D_{ft} = 1 - (1/F_{ft}) \exp\left(-X_t \varepsilon_{1t}^f L^c (F_{ft} - 1) / G_{ft}\right) \quad (27)$$

$$D_{fc} = 1 - (1/F_{fc}) \exp\left(-X_c \varepsilon_{1c}^f L^c (F_{fc} - 1) / G_{fc}\right) \quad (28)$$

$$D_{mt} = 1 - (1/F_{mt}) \exp\left(-Y_t \varepsilon_{2t}^f L^c (F_{mt} - 1) / G_{mt}\right) \quad (29)$$

$$D_{mc} = 1 - (1/F_{mc}) \exp\left(-Y_c \varepsilon_{2c}^f L^c (F_{mc} - 1) / G_{mc}\right) \quad (30)$$

$$D_f = 1 - (1 - D_{ft})(1 - D_{fc}) \quad (31)$$

$$D_m = 1 - (1 - D_{mt})(1 - D_{mc}) \quad (32)$$

As damage increases in the material, parameters from the stiffness matrix are reduced as shown below [45].

$$\begin{aligned}C_{11} &= (1 - D_f) E_1 [1 - (1 - D_m) \nu_{32} \nu_{23}] / \Delta \\ C_{22} &= (1 - D_f) (1 - D_m) E_2 [1 - \nu_{13} \nu_{31}] / \Delta \\ C_{33} &= (1 - D_f) (1 - D_m) E_3 [1 - \nu_{12} \nu_{21}] / \Delta \\ C_{12} &= (1 - D_f) (1 - D_m) E_1 [\nu_{31} \nu_{23} + \nu_{21}] / \Delta \\ C_{13} &= (1 - D_f) (1 - D_m) E_1 [\nu_{21} \nu_{32} + \nu_{31}] / \Delta \\ C_{23} &= (1 - D_f) (1 - D_m) E_2 [\nu_{12} \nu_{31} + \nu_{32}] / \Delta \\ C_{44} &= (1 - D_f) G_{12} \\ C_{55} &= (1 - D_f) G_{23} \\ C_{66} &= (1 - D_f) G_{13} \\ \Delta &= 1 - \nu_{32} \nu_{23} - \nu_{31} \nu_{13} - \nu_{21} \nu_{12} - 2 \nu_{13} \nu_{21} \nu_{32}\end{aligned}$$

This also influences the stress levels as the material behaviour is assumed to be linear-elastic and as such follows Hooke's law as shown in Equation [33].

$$\sigma = \begin{pmatrix} C_{11} & C_{12} & C_{13} & & & 0 \\ & C_{22} & C_{23} & & & \\ & & & C_{33} & & \\ & & & C_{44} & & \\ & sym & & & C_{55} & \\ & & & & & C_{66} \end{pmatrix} \epsilon \quad (33)$$

Regarding failure of the material, since the elements used in this simulation have only one integration point, this point's failure represented the element's failure. Material failure is defined as when fibre damage reaches 99% or when the element volume exceeds 3 times or becomes 2.5 times smaller compared to the previous increment. Once one of these conditions are met, the element is considered to have failed and it is removed from the simulation. Element removal was selected to avoid excessive element distortion.

It is assumed that the laminae are transversely isotropic. Also, the interface between the plies is assumed to be perfect; thus, relative inter-ply movement is not permitted, preventing any degradation of this interface. This perfect interface condition is created by partitioning the laminate to form the individual UD plies within the original laminate, modelled as one part. This assumption's effect on the laminate behaviour was deemed negligible from a study on the inter-ply modelling techniques [46].

#### 4.5.2 Modelling of the Bolts and Washers

The bolts and the washers made of steel are modelled as purely elastic isotropic material. A Young's Modulus of 200 GPa, a Poisson's ratio of 0.3 and a density of  $8000 \frac{\text{kg}}{\text{m}^3}$  were used for this material.

#### 4.5.3 Adhesive

The Araldite® LY 8601/Aradur® 8602 Epoxy System adhesive is relatively brittle, however, it is modelled as an elastoplastic isotropic material to capture the slight possible plastic deformation. The adhesive has a Young's modulus of 1.61 GPa, a Poisson's ratio of 0.35 and a density of  $1090 \frac{\text{kg}}{\text{m}^3}$ . The uniaxial tensile stress-strain curve of the adhesive obtained according to ASTM D638-14 is shown in Figure 14.

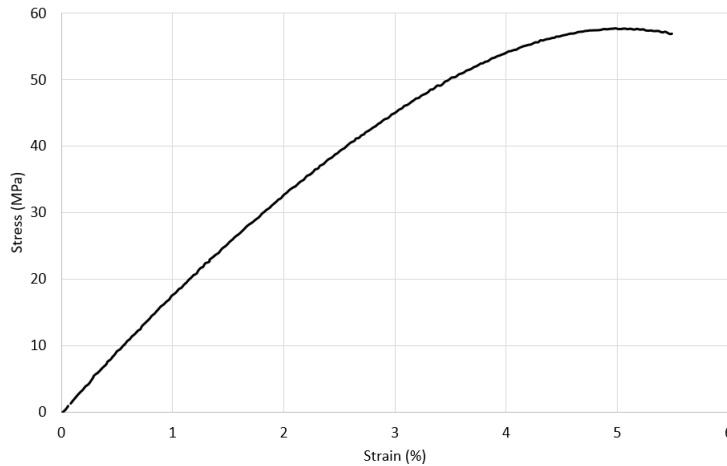


Figure 14: Araldite® LY 8601/Aradur® 8602 Epoxy System Uniaxial Tensile Stress-Strain Curve

Although the plastic deformation of the adhesive is defined by Figure 14, this indicates only the plastic behaviour under a uniaxial loading condition. Therefore, the adhesive's plastic behaviour was simplified by a linear Drucker-Prager plasticity model to define the yield criteria under different loading conditions as represented in Figure 15.

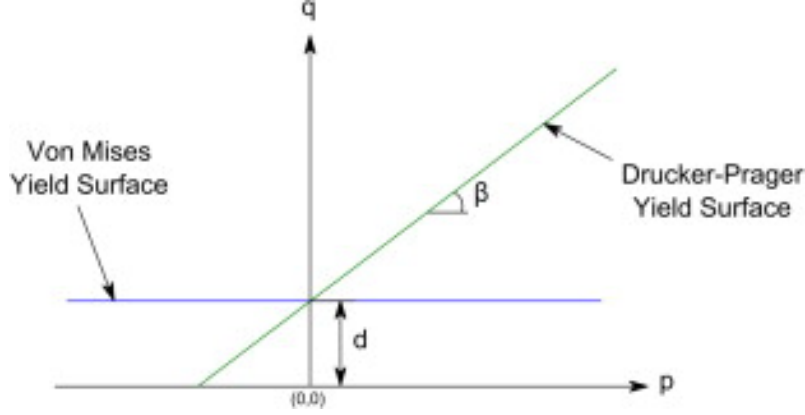


Figure 15: Linear Drucker-Prager Yield Surface 47

Where  $q$  is the equivalent Von Mises stress,  $\beta$  is the friction angle,  $p$  is the hydrostatic pressure,  $d$  is the adhesion strength of the adhesive and  $\sigma_{ya}$  is the adhesive uniaxial tensile yield strength. They can be calculated with the following equations (bold variable representing a tensor):

$$p = -\frac{1}{3} \text{trace}(\boldsymbol{\sigma}) \quad (34)$$

$$q = \sqrt{\frac{3}{2}(\mathbf{S} : \mathbf{S})} \quad (35)$$

$$\mathbf{S} = \boldsymbol{\sigma} + p\mathbf{I} \quad (36)$$

$$d = \left(1 + \frac{1}{3} \cdot \tan(\beta)\right) \cdot \sigma_{ya} \quad (37)$$

In this model, the linear Drucker-Prager yield surface is simplified to the Von mises yield surface as suggested by 47. That is implemented by assigning a value of 0 for  $\beta$ , making the adhesive yield surface independent of the hydrostatic pressure, like the Von Mises yield surface. Even though this simplification, emulates the Von Mises yield surface, Drucker-Prager was still used as it allowed to specify the material volume change due to plastic deformation, which is referred to as the dilation angle and assigned a value of  $10^\circ$  for this adhesive.

Non-destructive testing (NDT) techniques currently available do not offer repeatable and reliable monitoring of all defects potentially present in adhesively bonded joints. Therefore real-time monitoring of these types of joints is critical to record the structural behaviour and ensure a safe load transfer. The use of non-destructive structural health monitoring methods may permit the detection of damage in the adhesive at an early stage in prevention of catastrophic failure. However, the location of damage initiation in the adhesive needs to be predicted depending on a broad range of design parameters. This important aspect has drawn sustained attention of researchers interested in developing experimental studies of the damage as well as simulation modelling of the adhesive

medium behaviour when the joint is loaded.

The back-face strain measurement method, based on the concept of placing a proper sensor or defining a virtual strain gage using DIC on the back-face of the panel, has been developed to measure the strain as shown in Figure 16.

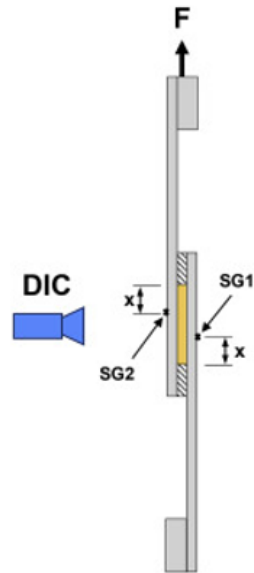


Figure 16: Test Assembly Sketch to Measure Back-Strain [48]

Until now, many investigations have been carried out to detect damage in the adhesive layer efficiently. As stated earlier, the exact location of the strain gauge is very significant. For a simple single lap joint, different sensor positions are feasible. The bending effect increases at a critical point located at the edge of the overlap where a crack may form as shown in Figure 17.

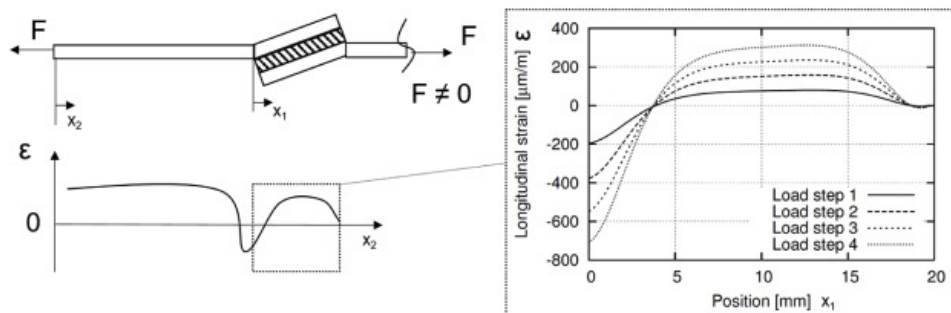


Figure 17: Characteristic Back-Face Strain Curve of SLJ Adherent, Schematic Strain Curve Overall (Left) and in the Overlap Length Range for Different Load Cases (Right) [49]

In addition, locations where strain gradients of the longitudinal strain variation are the largest are critical due to the relationship with the stress intensity factor, which defines the onset condition of crack formation that reduces the effective overlap length of the joint. This brief introduction was intended to present the most important background practical concepts taken into account by the modelling.



As presented earlier, bondline and cohesive failures are predominant in the adhesive. In our case, a purely cohesive failure is assumed for the structural-mechanical analysis of adhesive, as recommended in many studies. In addition, it is known that the internal strength of the adhesive is strongly related to the stress intensity factor and critical energy release rate depending on the fracture mode, which is a combination of traction, sliding and possibly tearing, increasing the complexity of the fracture mechanism in this case.

A surface-based cohesive model approach was used in the FE modelling to simulate the fracture behaviour of the adhesive. Many researchers have widely used the so-called cohesive zone model (CZM) to simulate the progressive damage (initiation and propagation stages) in adhesively bonded joints. In this approach, cohesive connections are modelled by a fictitious, zero-thickness interface that behaves according to a constitutive damage law based on the traction-separation law.

Beside treating the entire adhesive layer thickness as a cohesive zone or considering its interface with the laminate, there are several possibilities for positioning it within the thickness, as depicted in Figure 18. A study of the effect of this positioning conducted by [50] has concluded minimal deviations in the strain-load curve compared with the experiments. Therefore, the midplane of the adhesive layer (option 2 in Figure 18) was selected to accelerate the simulation process.

The constitutive damage law used in the modelling, based on the traction-separation law, is capable of simulating the gradual damage of the adhesive based on the correlation between the traction and the relative displacement (separation in this case).

Abaqus contains a routine capable of implementing the cohesive zone model as a bilinear law that consists of three main parameters; elastic stiffness, critical traction and fracture energy; schematically represented in the generic Figure 19 representing axial loading. A mixed mode cohesive zone model was used for 3D modelling to predict a damage initiation, represented by the critical level in Figure 19, using the quadratic nominal stress criterion, Equation (38) [29] [26].

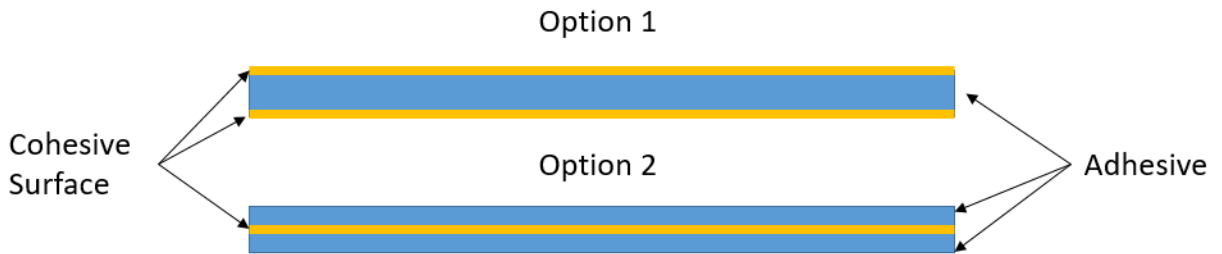


Figure 18: Cohesive Surface Positioning

$$\left\{ \frac{\langle t_n \rangle}{t_n^o} \right\}^2 + \left\{ \frac{t_s}{t_s^o} \right\}^2 + \left\{ \frac{t_t}{t_t^o} \right\}^2 = 1 \quad (38)$$

Where  $t_n$  is the normal traction stress,  $t_s$  and  $t_t$  are the shear traction stress, the superscript  $^o$  signifies the ultimate stress and the Macaulay bracket  $\langle \rangle$  signifies that compression does not initiate damage.

The monitoring of damage evolution is permitted to gradually decrease the cohesive stress beyond the prediction point of the failure criterion. This is done by degrading the stiffness of the contact interaction surface according to Equation (39).

$$\mathbf{t} = \begin{Bmatrix} t_n \\ t_s \\ t_t \end{Bmatrix} = (1 - D) \begin{bmatrix} K_{nn} & & \\ & K_{ss} & \\ & & K_{tt} \end{bmatrix} \begin{Bmatrix} \varepsilon_n \\ \varepsilon_s \\ \varepsilon_t \end{Bmatrix} \quad (39)$$

Where  $D$  is the damage variable of the cohesive interaction in the form of a scalar,  $K_{nn}$ ,  $K_{ss}$  and  $K_{tt}$  are the cohesive layer stiffness coefficient and  $\varepsilon_n$ ,  $\varepsilon_s$  and  $\varepsilon_t$  are the cohesive layer strains. The damage variable varies monotonically from 0 at damage initiation to 1 when complete failure is observed.

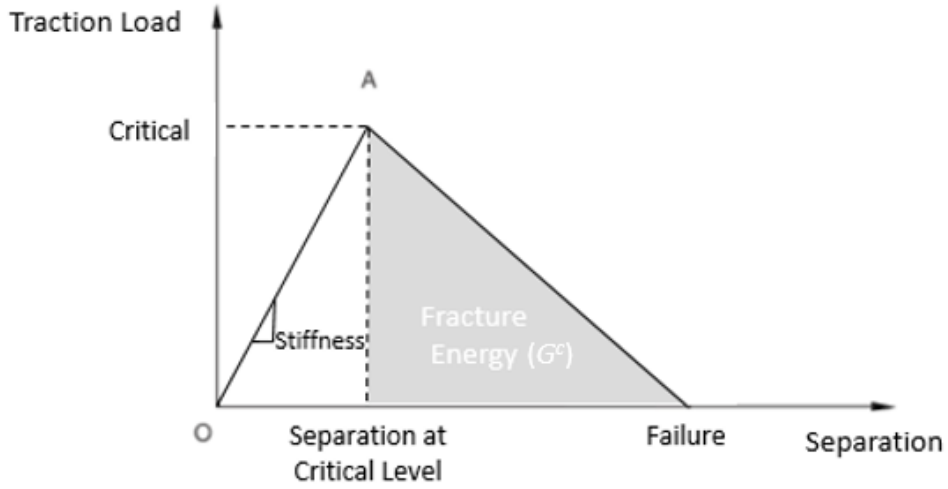


Figure 19: Linear Traction Separation Cohesive Zone Model [29]

The energy-based mixed-mode damage evolution law based on the fracture energy, developed by Benzeggagh and Keane [29] was used in this work to determine the critical fracture energy ( $G^c$ ) as shown in Equation (40). This considers the effect of each mode, normal ( $G_n^C$ ) or shear ( $G_s^C$  and  $G_t^C$ ), in controlling the evolution damage until failure.

$$G^C = G_n^C + (G_s^C - G_n^C) \left( \frac{G_s^C + G_t^C}{G_n^C + G_s^C + G_t^C} \right)^\eta \quad (40)$$

The material parameter  $\eta$  was assigned a value of 2 as suggested in [50] for a similar adhesive.

The cohesive properties of the adhesive were taken from [50, 51] as shown in Table 4, which also contains the shear strength of a similar adhesive (EA 9628 Film Adhesive).

Table 4: Cohesive Surface Properties

$t_n^o$ MPa	$t_s^o$ MPa	$t_t^o$ MPa	$K_{nn}$ [50] N/mm <sup>3</sup>	$K_{ss}$ [50] N/mm <sup>3</sup>	$K_{tt}$ [50] N/mm <sup>3</sup>	$G_n^C$ [50] mJ/mm <sup>2</sup>	$G_s^C$ [50] mJ/mm <sup>2</sup>	$G_t^C$ [50] mJ/mm <sup>2</sup>
55	39.3	39.3	10 <sup>5</sup>	3.575x10 <sup>4</sup>	3.575x10 <sup>4</sup>	2.5	5	5

## 4.6 Element Type and Mesh

In order to capture the high stress gradients around the holes, the specimens have been partitioned into regions permitting smart meshing. First-order solid hexahedral reduced integration (C3D8R) elements were used for the entire model. These elements have 1 integration point and 8 nodes as shown in Figure 20. Each node is capable of only translation degree of freedom (Dof), giving a total of 24 degree of freedom to these elements.

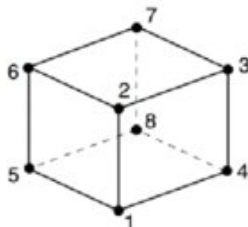


Figure 20: First-Order Solid Hexahedral Reduced Integration (C3D8R) Elements 52

The reduced integration scheme was used to reduce the computational cost and avoid shear locking, a common problem with fully integrated solid elements causing an overly stiff model leading to inaccurate results 53. However, the reduced integration elements can suffer from hourglassing due to the lower number of integration points. Thus, an enhanced hourglass control algorithm was selected to artificially add stiffness to avoid the element's hourglassing 29. The added stiffness appeared insignificant and did not influence the models accuracy. Additionally, the use of reduced integration elements required a slightly finer mesh in the high stress gradient regions. Still, even with this increase in the number of elements, the computational cost remained lower than when using fewer fully integrated elements. The mesh convergence study can be found in Appendix A.3.

### 4.6.1 OHT Case

The strain results, monitored as the time step when fibre damage initiation was observed, converged for the same mesh for every configuration for both studied layups. The mesh for the OHT models shown in Figure 21 served as a starting point for the other configurations. It was determined that the mesh refinement at the hole was sufficient for the other configurations (3OB and HBB), which are shown in Figure 22 and 23. This is attributed to the fact that, even though the hole is unloaded for OHT specimens, the stress concentration is located at the same location and the geometry in this critical region, remains unchanged between OHT and the joints.

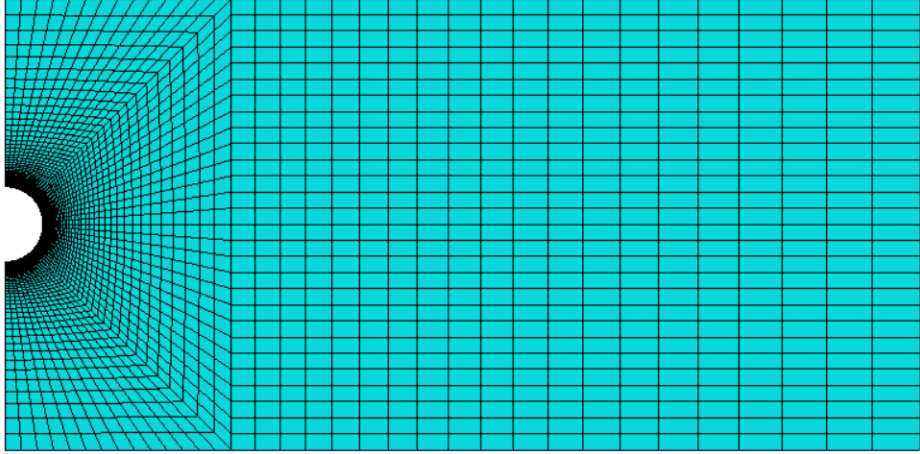


Figure 21: Mesh Plot for the OHT Models

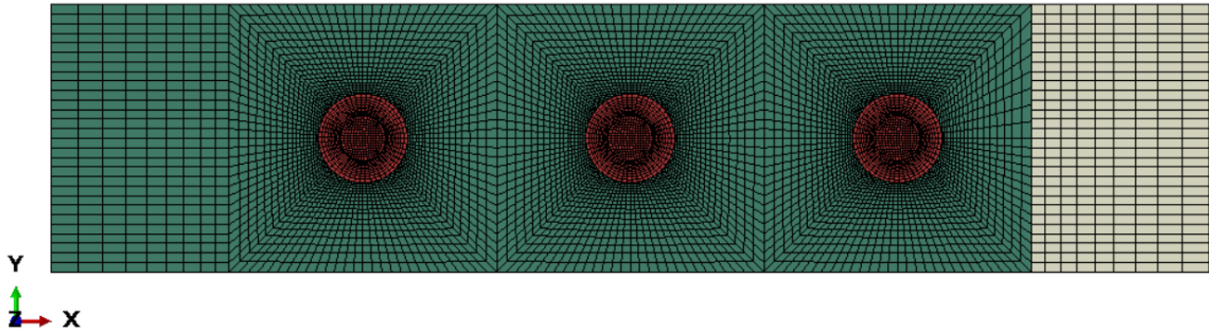


Figure 22: Mesh Plot for the 3OB Joints

The mesh had to be changed significantly for the HBB joints because the addition of an adhesive layer resulted in high stress concentration at the overlapping ends. As mentioned earlier, around the bolt-hole, the mesh density remained the same as in OB joints. A different partitioning method was used to help capture the stress gradient at the overlap ends. This led to a significant increase in the number of elements, but that was necessary due to the joint's different nature, which is now influenced by the behaviour of an adhesive layer.

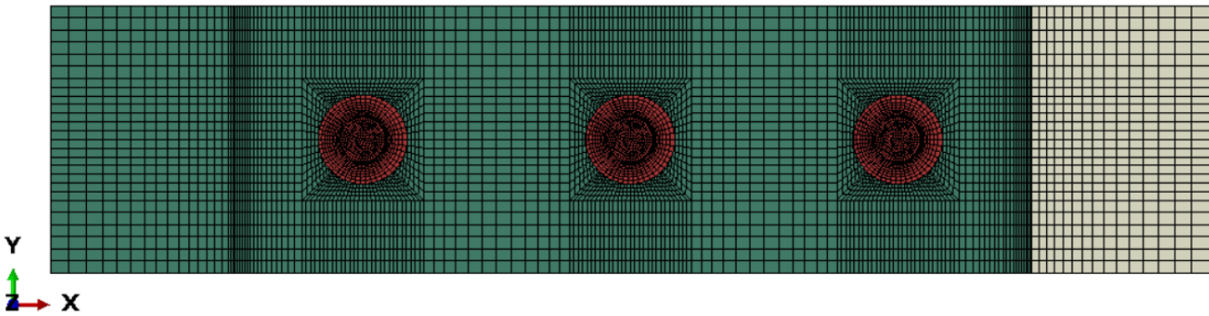


Figure 23: Mesh Plot for the HBB Joints

Table 5 shows the solution times for the various models along with their number of nodes. The

simulation were run using an Intel Xeon CPU E5-2637 v3 @ 3.50 GHz running on 8 cores.

Table 5: Computational Time of Various Models

Geometry		OHT	3OB Joint	HBB Joint
Target Time Increment (s)		1.00E-04	6.00E-05	1.20E-04
CP12	# of Nodes	100800	1138092	692732
	Simulation Time (h)	1.6	18.2	17.9
QI12	# of Nodes	419244	2168584	1395699
	Simulation Time (s)	9.7	40.1	42.4

## 4.7 Loading and Boundary Conditions

Depending on the model geometry and the joint/specimen configuration, the boundary conditions (BC) varied slightly. For the OHT models, as shown previously in the geometry section, the model contained none or two planes of symmetry depending on the layup. All the faces at the end opposed to the hole are fixed in the  $z$  and  $y$  directions with a prescribed displacement of 1mm/min in the  $x$  direction only. A symmetry boundary condition is applied about the  $Y$ - $Z$  plane at the model midplane (at the hole location), and about the  $X$ - $Z$  plane for the CP layup as shown in Figure 24.

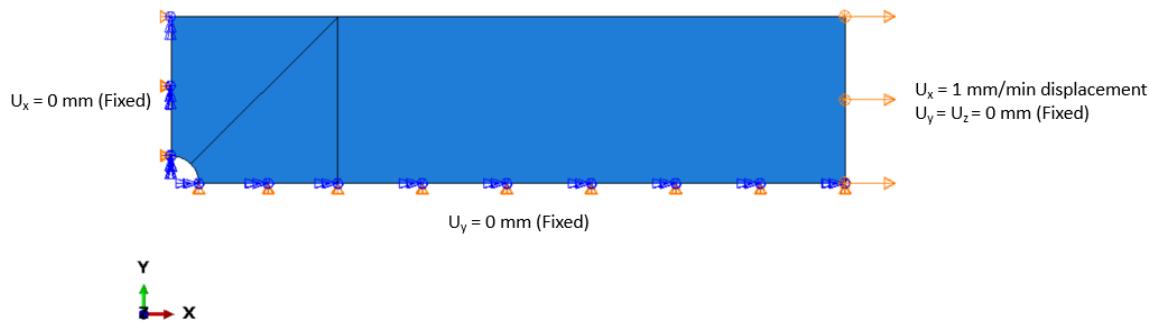


Figure 24: OHT Models Boundary Conditions (Shown for CP Layup)

For the joint configurations (OB or HBB), the end faces of the upper laminate on the grip side have a prescribed displacement of 0 in all directions, while the end faces of the lower laminate on the grip side have a prescribed displacement of 0 in the  $y$  and  $z$  directions with a prescribed displacement in the  $x$  direction at a rate of 2 mm/min as shown in Figure 25. Additionally, the CP layups have a symmetry BC as only half of the joint is modelled, as shown in Section 4.1. Also, a temperature field is applied to the washers to simulate the bolt preload.

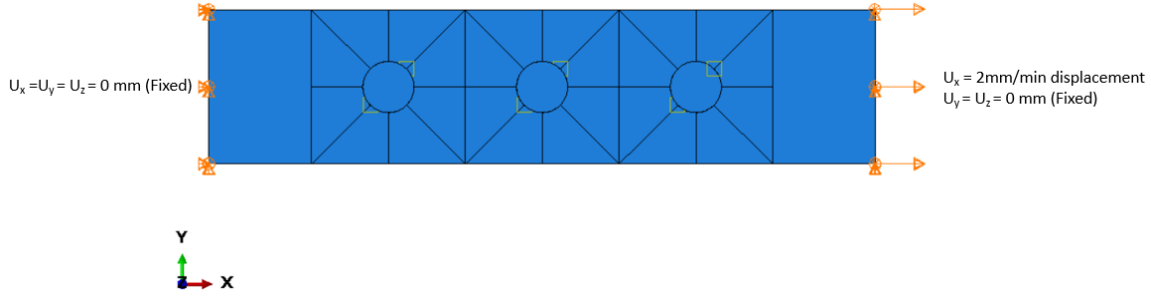


Figure 25: OB and HBB Joints Models Boundary Conditions (Shown for QI Layup)

The reaction force used to evaluate the applied load is computed by summing the axial reaction forces taken at the nodes on the constrained grip side, as shown in Figure 26. In the case of CP layups, this sum is multiplied by a factor of 2 as only half the joint is modelled.

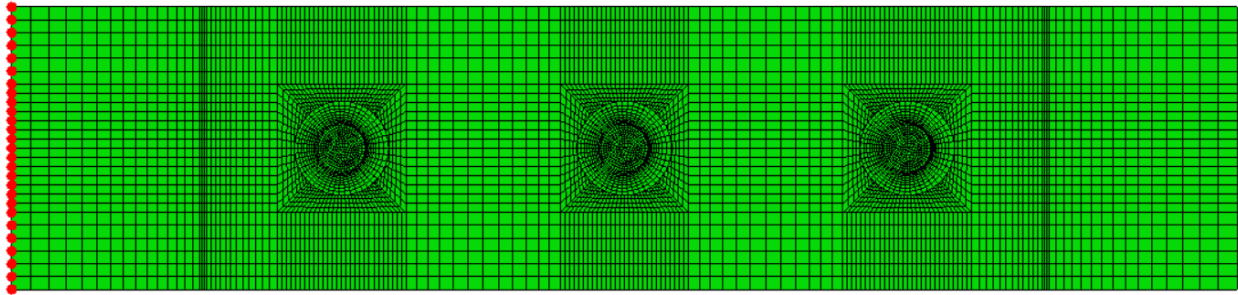


Figure 26: Nodes (in Red) at Which Reaction Forces Are Extracted

#### 4.7.1 Bolt Clamping Load

In the experiments, a bolt preload of 5 Nm was applied to the bolts [54]. The preload can be calculated using Equation 41, where  $k=0.16$  for a cadmium-plated bolt [55]. This equation allows a calculation of the internal axial force in the bolt shank  $FN$  to be implemented in Abaqus/Standard.

$$FN = \frac{T}{d k} \quad (41)$$

Where  $T$  is the applied bolt torque,  $d$  is the hole diameter and  $k$  is the torque coefficient.

Bolt preload is not an available loading condition in Abaqus/Explicit, while it is in Abaqus/Implicit. The technique used here is to apply the preload in Abaqus/Implicit and compare the resulting out-of-plane stress distribution on the laminate to the out-of-plane stress distribution on the laminate in Abaqus/Explicit. In Abaqus/Explicit, a technique commonly used to apply bolt preload is to use a thermal load applied to the bolt shank or the washers to either create a compression of the bolt shank or put tension on the bolts by expanding the washers [56, 57]. Applying a temperature field to the washer, resulting in tension in the bolt, is used as it seems to be the best physical representation of a standard preload and it produced very good results in other studies [56]. The temperature gradients reported in Table 6, based on a thermal expansion coefficient of  $8.4E-05 \text{ K}^{-1}$  were found to simulate the clamping load accurately by resulting in a 4930 N axial bolt load. The

values were selected so that they produce the required preload and have no physical meanings. A higher washer temperature had to be applied for HBB joint configuration to achieve the desired preload due to the lower total out-of-plane stiffness of the assembly due to the presence of the adhesive layer. The expansion coefficient was applied only along the thickness direction as shown in Figure 27 with the other orientations being insensitive to the applied temperature.

Table 6: Temperature Gradients Used in the Simulation Process of the Clamping Load

Joint Type	T [K]
OB	147
HBB	188

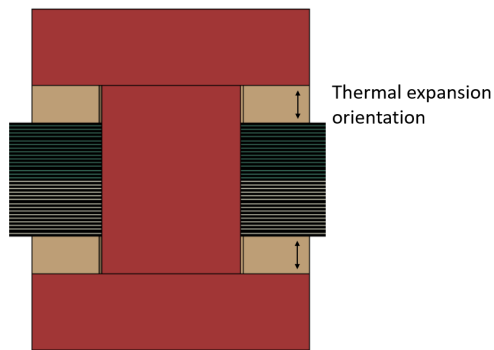


Figure 27: Washer Thermal Expansion Direction

# 5. Material Model Calibration and Model Validation

## 5.1 Experimental Procedure

### 5.1.1 Static Tensile Tests

As stated earlier, experimental tests were used to obtain the necessary input data for the FEA modelling and to validate the simulation results. These experimental tests were performed at the Center for Applied Research on Polymers and Composites (CREPEC) and are the work of Dr. Masoud Mehrabian and Mr. Aouni JR. Lakis [58, 8, 59]. Although HBB joints may be used in aircraft structures to join upper and lower fuselage sections, for example, the geometry of the experimental specimens were chosen to be following ASTM standards. Open hole test (OHT), only-bolted (OB) and hybrid bolted/bonded (HBB) types of specimen were considered; with OHT specimen manufactured per the ASTM D5766 standard [58]. The single-lap (SL) shear bolted joints (OB and HBB) with three bolts were fabricated according to the ASTM-D5961 standard [59]. Hexagonal head steel fasteners (NAS6204-4) having a shank diameter of 6.35mm and nuts (MS21042-4) were used. These bolts were fitted with cadmium-plated steel washers (NAS1149F0463P), having an internal diameter of 6.73mm and external diameter of 12.70 mm, on both sides (head and nut sides), and an adhesive layer of 0.15 mm (Araldite® LY 8601 / Aradur® 8602) was applied between the overlapping surfaces of the HBB joint.

The composite plates were made of carbon-fibre reinforced epoxy (CFRE) 3K plain weave T300 carbon fabric and Araldite® LY 8601 / Aradur® 8602 epoxy system using vacuum-assisted resin transfer moulding process (VARTM) [59]. All tensile tests of the OHT, OB and HBB coupons serving as a baseline were conducted on a servo-hydraulic MTS machine model 810 at an extension rate equivalent to 2 mm/min. At least five coupons were used for each configuration to obtain a meaningful average experimental result. The 3D DIC system and software used is a Vic-3D v 7.2.4 model from Correlated Solutions Inc., USA. Table 7 contains the stacking sequence and fibre orientations of the cross-ply and quasi-isotropic composites considered in this study.

Table 7: Stacking Sequence of Studied Specimens

Cross-ply symmetric sequence-12 plies	$[(0/90)/(0/90)/(0/90)/(0/90)/(0/90)/(0/90)]_S$
Quasi-isotropic symmetric sequence-12 plies	$[(0/90)/(\pm 45)/(0/90)/(\pm 45)/(0/90)/(\pm 45)]_S$

### 5.1.2 Digital Image Correlation Measurements

Digital Image Correlation (DIC) is an optical, non-contact measurement technique that can determine displacement fields in a loaded test specimen [60]. It measures the full field strain over the side surface of the specimen. Two charge-coupled (light-sensitive integrated circuit that captures images by converting photons to electrons) device cameras measurement can identify three-dimensional surface contours and the strain distribution of the surface by taking into account the displacement in the depth direction. DIC measurement can recognize the surface characteristics of an object in digital camera images and allocates coordinates to the image pixels. Then, DIC measurement records additional images during the loading of the object, compares the digital images and calcu-



lates the deformation of the object characteristics based on the first image (i.e. undeformed state of the object). This technique, coupled with an appropriate software, was used to determine the longitudinal strain field on the laminates [58, 8]. This data has served to calibrate and validate some of the simulated results.

The approach used for determining the characteristics of the UD plies used in this study was presented earlier in sub-section 4.5.1. However, a validation of the material properties listed in Table 1 is necessary. A comparison between FEA models and experimental results was done to confirm the accuracy of the simulation. For the validation process, the failure of the specimen/joint is defined as the peak load after which the specimen/joint cannot carry more load. Experimental results pertaining to plain weave woven fabric in the OHT configuration were used to verify the ultimate strength as well as the strain field around the holes and the stress concentration factor. Damage and failure models were only used for the overall validation of the experimental results. Specific failure modes were not validated. This did not hinder the design study as damage models were not used in the design study since failure was assumed to occur when damage was initiated.

## 5.2 OHT

### 5.2.1 Longitudinal Strain Field

The strain field at the discontinuity was measured using the DIC technique described earlier. The longitudinal strain field results are shown for FEA and DIC in Figure 28 where variations of the strain field with respect to the x-axis are evaluated as:  $\epsilon_{xx} = du/dx + ((du/dx)^2 + (dv/dx)^2)/2$ . The DIC presents a weakness in this case as it does not allow proper measurement of the strain at the very edge of the hole. An adjustment was made to the FEA results in order to reflect the state of this uncaptured region.

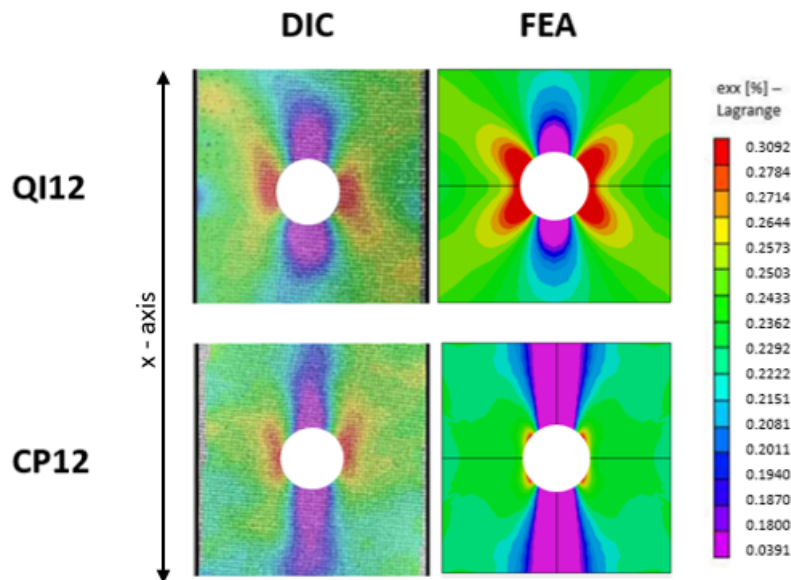


Figure 28: Strain Field in the Loading Direction  $\epsilon_{xx}$  at 25% of Ultimate Load for OHT CP12 and QI12 Laminates [58]

The case of QI12 and CP12, loaded at (9.1 kN and 10.1 kN, respectively) which represents 25% of the maximum load at failure detected during the experiments, was chosen to illustrate not only

the state of strain in the vicinity of the hole for OHT coupons but also to assess the validity of the simulation results to calibrate the model.

It is to note that the loading level equivalent to 25% of the ultimate strength is, in fact, higher for CP than QI; the first containing more 0 degree orientation plies for an equivalent thickness. A reasonable agreement is revealed between the simulation and the experiment. Quantitatively, maximum discrepancies of 5% and 8% were detected for QI and CP layups, respectively. These deviations are explained by the difficulties of manufacturing high quality laminates that contain perfectly oriented fibres and precise layer thicknesses. Additionally, unpredictable damage may occur during the drilling process of the holes, although it is unlikely that this caused significant discrepancies at low load levels. The high strain regions, originating from the hole edge, tend to stretch along the loading direction (0 degree layers) for CP and in the 45 degrees direction for the QI. The same trend observed for QI has been reported for the case of isotropic materials such as aluminum [61]. The increased notch sensitivity of CP layups compared to QI layups reported in [8] is depicted as strains reduce quickly when moving away from the hole in CP layups. Additionally, it is noted that, due to its lower stiffness, the QI layup displays greater strains in all regions compared to the CP layup, even though it is evaluated at a lower load level than the CP layup. The condition of convergence of the strain field results for CP layups has yielded the longitudinal and transverse stiffness of the UD laminates. On the other hand, the QI results served to estimate their shear modulus.

### 5.2.2 Ultimate Failure Strength

The simulated tensile strength at failure was also compared to the experimental results for validation purposes. These results are contained in Table 8. This similarity confirms the validity of the material properties estimated above. Due to the higher ply count in the loading direction, the CP layup has higher strength, although this advantage is slightly attenuated by the fact that CP layups are more notch sensitive, as discussed in the next section. Yet, independently of the layup, all models failed by tensile fibre failure.

Table 8: OHT Ultimate Failure Strength

Parameter	CP12	QI12
OHT FEA Failure Stress (MPa)	423	364
OHT Experimental Failure Stress (MPa)	409	366
Discrepancy (%)	3.2	-0.5

### 5.2.3 Stress concentration Factor at the Hole

Another important parameter that specifies the level of stress peak generated by the hole is the stress concentration factor. This parameter depends on the elastic and shear properties of the laminate as well as the geometry of the discontinuity as expressed by the analytical model developed by Lekhnitskii [62] and reported here (Eq. 42). The case of CP was chosen to illustrate the comparison of the results predicted by the simulation and the analytical model, depicted in Figure 29. A negligible discrepancy of less than 8% was found, consolidating the previous conclusions of agreement of the results.

$$\sigma_x(y, 0) = \frac{\sigma^\infty}{2} \left\{ 2 + \left(\frac{r}{y}\right)^2 + 3 \left(\frac{r}{y}\right)^4 - (1 + n - 3) \left[ 5 \left(\frac{r}{y}\right)^6 - 7 \left(\frac{r}{y}\right)^8 \right] \right\} \quad (42)$$

Where  $\sigma^\infty$  is the longitudinal stress in the far-field.

$$n = \sqrt{2 \left( \frac{E_1}{E_2} - 2\nu_{12} \right) + \frac{E_1}{G_{12}}} \quad (43)$$

Where at the hole edge  $y = r$  and at the center of hole  $y = 0$ .

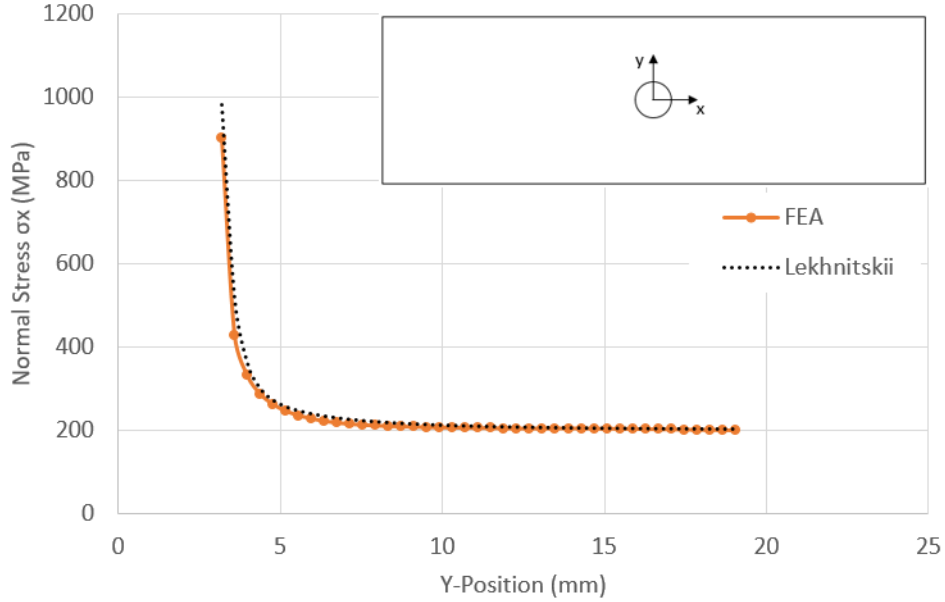


Figure 29: FEA and Analytical Normal Stress ( $\sigma_x$ ) vs Y Position in the  $0^\circ$  External Layer For CP Layup OHT Specimen

The simulated results of the variation of this factor across the section at the opening are shown in Figure 30 for both layups. A higher stress concentration factor at the hole's edge was obtained for CP compared with QI due to its higher degree of anisotropy. The trend is reversed away from this discontinuity when the effect of the higher average stress level for CP becomes dominant until it decays. This result confirms the observation made in [8] indicating that CP laminates are more notch sensitive.

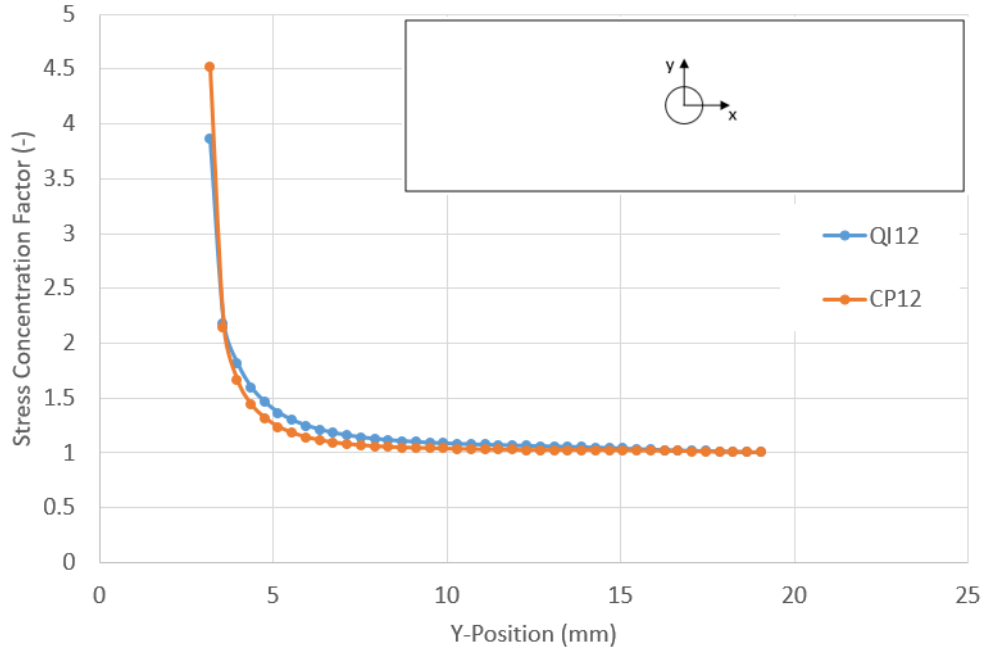


Figure 30: Normal Stress Concentration Factor in  $0^\circ$  plies ( $\sigma_x/\sigma_x^\infty$ ) vs Y Position in OHT Models for QI12 and CP12

### 5.3 3OB and HBB Joints

Further evaluation of the simulation model was performed considering actual bolted as well as hybrid joints to analyze the effects of reinforcement of the holes and load transfer by the bolts for the 3OB configuration and the effects of integration of the adhesive at the interface in the case of HBB joints. Finite element analysis were performed on these joints resulting in the variation of the nominal stress, determined from the imposed loading, with respect to the elongation simulated by the displacement at the grip end of the joint. The comparison between the experimental results and the simulation for the CP and QI is shown in Figure 31 and 32. Only the portions pertaining to the loading phase until the onset of the bearing failure were simulated.

Although it will be analyzed in detail in the next chapter, the improvement in performance of the HBB joint is noticeable. A good agreement between the predictions and the actual results was found for the CP case. A weaker correlation was noted for QI in the case of the HBB joint. It was noted during the experiment that the QI laminates had a slightly higher fibre volume fraction content. Thus, it would mean that the mechanical properties of each ply would be higher than for the CP layup. However, in the simulation, the same mechanical properties were used independently of the layup, which creates this discrepancy. Additionally, more conservative results were obtained for the 3OB caused by the sensitivity of Hashin failure criteria to the high shear stresses developing at the loaded holes. Nevertheless, it was decided to continue the simulation work of analysis of the HBB joint using the material properties already obtained, thus limiting the iterative process.

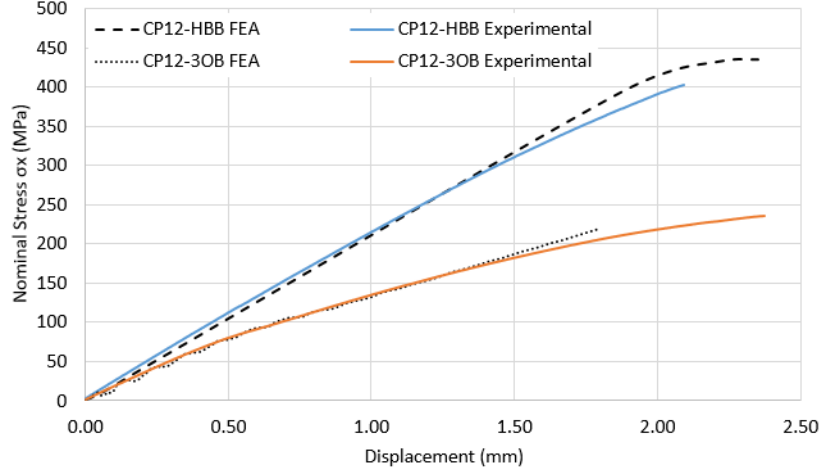


Figure 31: Nominal Stress-Displacement Curves for 3OB and HBB Joints, Case of CP Layout

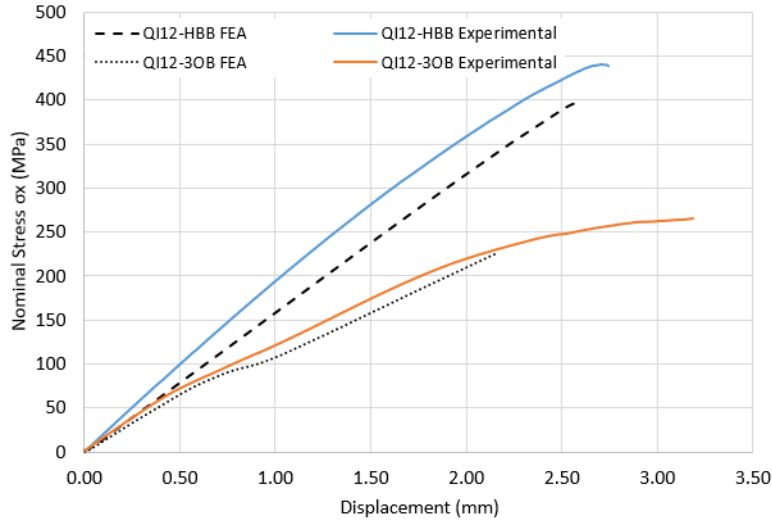


Figure 32: Nominal Stress-Displacement Curves for 3OB and HBB Joints, Case of QI Layout

For the HBB joints, experimental tests showed that for the CP and QI configurations, adhesive failure initiation is expected between 30 and 45% of the ultimate failure stress of the HBB joint. This cannot be seen on the stress-displacement curves, but it was captured by DIC. The simulation predicted an adhesive failure initiation at a stress level corresponding to 40% for CP and 33% for QI of the experimental failure stress of their respective HBB joints, which also reinforces the validation of the models.

### 5.3.1 Longitudinal Strain Field in 3OB and HBB Joints

Additional testing of the performance of the simulation model was conducted by carrying out a comparative assessment of strain acting along the loading axis and taking place at the external surface of the 0 degree layer, for the case of several load levels. For joint configurations, DIC presents a significant limitation as the washers prevent strain measurements on the laminate near the holes. As such only the region away from the washer can be used for validation of the FEA model. These results are depicted in Figure 33 and 34 taking note that the failure load (FL) of the 3OB joint is

about 50% lower than the equivalent HBB.

The effect of the bolts for 3OB and the stress concentration reduction at holes caused by the addition of the adhesive in HBB joints is noticeable and adequately captured by the simulation. The bolt load distribution phenomenon, which will be detailed in the next chapter, commonly occurring in multiple fasteners joints, has developed a strain gradient originating at the beginning of the overlap and propagating toward its end. This trend was observed independently of the type of layup. The analysis of the strain field pattern reveals a reduction of the effects generated by the 45 degree layers of QI layups for the case of HBB; resulting in a similar behaviour to CP. Undoubtedly higher longitudinal strains are observed in QI layups due to their lower stiffness. However, no matter the layup, the high strain region propagates roughly at a 45° angle at the hole in 3OB due to the bearing pressure applied by the bolt shank. Thus, it is observed that while the type of layup influences strain levels, the joining method has the most significant influence on the strain field pattern. A discrepancy is observed for CP12-HBB joints, where a high tensile strain region is observed behind B1. This represents an error of the DIC apparatus as this is a region of compression and no high tensile strains are expected. These data confirm once more a good agreement between the experimental and simulated results.

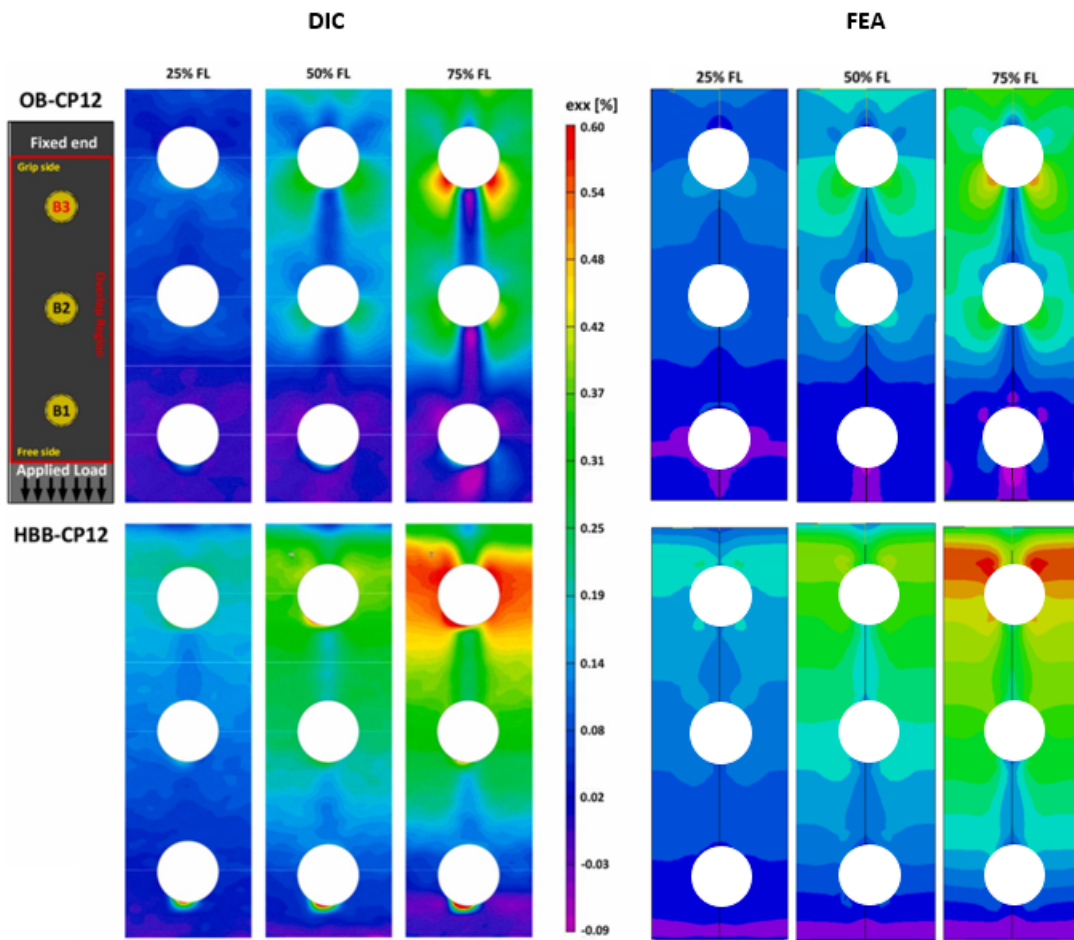


Figure 33: Longitudinal Strain Field for the CP Layup Away From the Washer, Comparison Between DIC Results [8] and Simulation

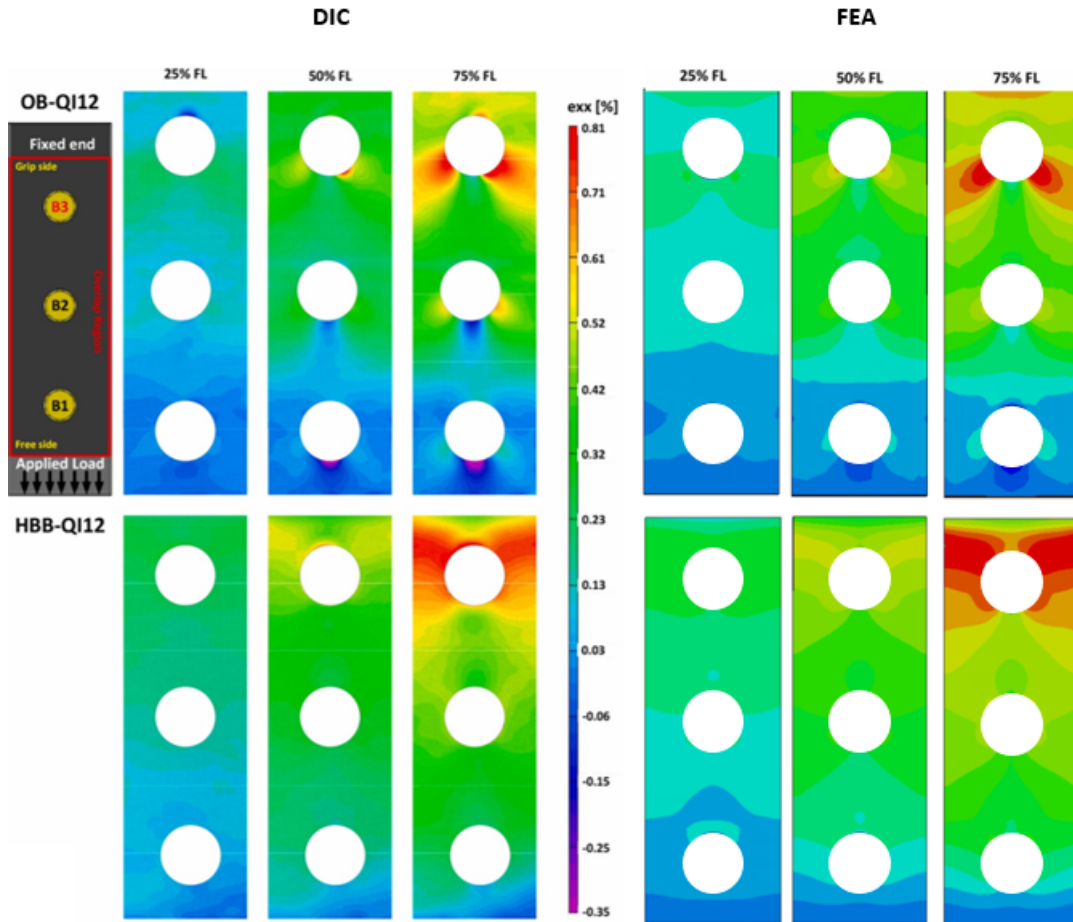


Figure 34: Longitudinal Strain Field for the QI Layup Away From the Washer, Comparison Between DIC Results [8] and Simulation

The results of this chapter showed good agreement with experimental data for different tensile test configurations (OHT, 3OB joints and HBB joints). A comparison of load-displacement behaviour, ultimate strength, stress concentration distribution and the longitudinal strain field proved that the modelling strategy can yield accurate results. This is highly pertinent as high-fidelity results can be obtained at a relatively low computational cost when using woven fabric.

## 6. Design Optimization Study of HBB Joints

This study aims to provide guidelines for improving the performance of HBB joints. Improvement of HBB joints can be made by reducing the weight of the joint for the same strength or by increasing its strength for the same weight. The mechanism of damage initiation and bolt-adhesive interaction are important features characterizing the performance of these joints. The bolt-adhesive interaction can take the form of load sharing or reduction of peel stresses at the overlap ends. Researchers have already established that load-sharing, a characteristic of the load distribution between the adhesive and fasteners, is a crucial factor influencing the performance of HBB joints. Unfortunately, this ideal situation may be challenging to achieve in reality. Thus, geometric parameters and adhesive properties will be investigated to see if they can allow proper load sharing before joint failure. Additionally, the influence of geometric parameters on the bolts' contribution to the reduction of peel stresses in the adhesive will be analyzed. According to the preliminary results above, HBB joints offer superior performance compared to bolted joints but also, as reported by different authors, to bonded joints in experimental tests due to crack stopping featured by the bolts [63, 7, 8]. This indicates that the bolts must have a definite impact on the failure of the adhesive layer. For this Chapter, failure of the joint is defined as the onset of fibre or adhesive damage initiation. This was chosen as it reduced the length of the simulation while still being a good indicator of the relative strength of the different joint configurations. Additionally, no experimental results are available to compare the following FEA results. As the model was validated in the previous chapter, it is assumed that the simulation can now be used to carry the optimization study.

Before presenting the results of this study concerning HBB joints, joining mechanisms taking place in 3OB and adhesively bonded joints will be analyzed to understand how they transfer load and how failure develops in them. Additionally, the difference between the classic joining methods and HBB joints will be highlighted to understand the gains made by hybridization and areas of improvement that can be achieved through careful design. Finally, the characterization of the different joining methods will allow a deeper understanding of the bolts' contribution to the load-carrying capability of HBB joints.

### 6.1 Joining Methods Characterization

#### 6.1.1 Joining Mechanisms

Mechanically fastened joints are used to transfer load from one component of the structure to another. This transfer occurs through the contact zone that develops between the fastener and the internal surface of the hole when a load is applied. Multiple fasteners arranged in a specific pattern are usually needed to generate a larger contact surface between the joined plates and moderate secondary adverse effects of this assembly method, such as out-of-plane bending moment. On the other hand, adhesive bonding has become a more efficient load transfer mean than the former, providing a uniform stress distribution due to the elimination of stress concentration peaks at the discontinuities. However, there are still challenges related to quality-control constraints that are presently much more severe. The combination of both assembly methods has started to draw researchers' attention; interested in optimizing the design of joints used by the aerospace industry to enhance the load transfer performance at a lower weight. Unfortunately, early analysis has shown that, in the case of hybrid joints, the fasteners share only a small portion of the applied load and may be needed to satisfy redundancy requirements only. However, the fasteners' potential prevention of peel stress



at the critical locations of the joint presents advantages in terms of the impediment to delamination propagation along the bond line. The joint model considered in this study is shown in Figure 35.

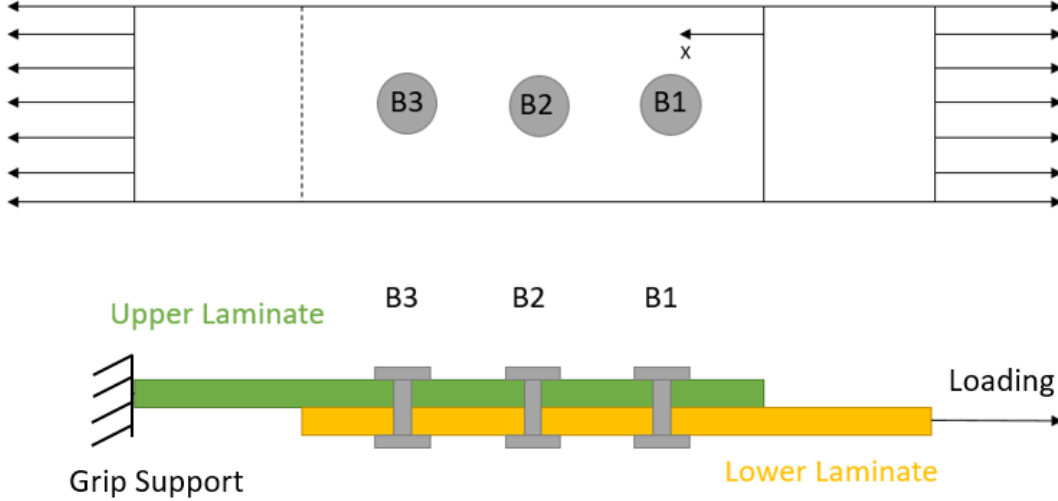


Figure 35: Joint Model

#### 6.1.1.1 Bolted Joints

Upon loading a single lap shear joint, the bolt makes contact with the plate's hole and transmits a percentage of the load to the second plate, while the remainder by-passes this location. As a result, a Hertzian contact stress distribution, called bearing stress, arises in the radial direction. Simultaneously, the by-pass load results in the development of tangential stress amplified by stress concentration effects at the hole edge. Figure 36 shows a generic relationship between the two stresses for a certain ratio that depends on the characteristics of the joint, remaining constant until failure. The linear reduction in laminate resistance towards a specific failure mode with the increase of bearing load is truncated by a bearing-stress cut-off equivalent to the bearing strength of the material. Due to the bearing load applied by the bolts on the laminate, stress concentration at holes are greater compared to unloaded holes. The constant  $C$  in the equation, limiting the safe domain of application without failure, expresses the stress-concentration relief phenomenon due to the non-homogeneous nature of the composite materials.  $C$  permits to correct the standard theoretical stress concentration factor to determine its effective value, based on the net section, according to the following equations [64]:

$$k_{th} = 2 + \left(\frac{w}{d} - 1\right) - 1.5 \frac{(w/d - 1)}{(w/d + 1)} \theta \quad (44)$$

Where,

$$\theta = 1 \text{ for } \frac{e}{w} \geq 1$$

$$\theta = 1.5 - \frac{0.5}{(e/w)} \text{ for } \frac{e}{w} \leq 1$$

$$k_{eff} = 1 + C (k_{th} - 1) \frac{w}{w - d} \quad (45)$$

The literature reports a value of  $C$  close to 0.25 for 6.5 mm diameter hole in quasi-isotropic carbon/epoxy laminates, increasing for orthotropic laminates. Overall, it was shown that the value of  $C$  is close the percentage of  $0^\circ$  plies in the laminate. A single value for  $C$  is applicable only when the failure mode does not change. For instance, for small diameter holes in relation to the width, laminates may fail in bearing rather than in tension through the hole.

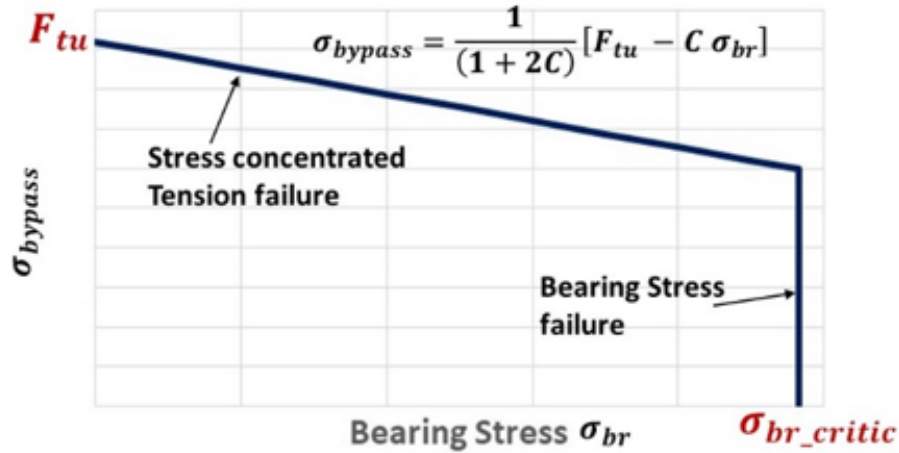


Figure 36: Classical Bypass-Bearing Relationship

Additionally, it is known that the bearing strength of composite laminates is strongly dependent on the magnitude of the transmitted clamping force generated by bolt tightening. However, although improvement in bearing strength of composites is realized through higher torquing of the fastener, the tension strength of the section across the hole may control the failure. Finally, the strength and the type of failure of bolted joints loaded in shear depend on different factors such as the boundary conditions, the geometric characteristics of the joint, materials and properties of the laminate as well as the geometric characteristics of the bolt.

Another important feature of bolted joints concerning load transfer is the load-sharing between the bolts. For example, in a 3-bolt configuration, it was reported that an uneven fraction of the total load is transferred by each bolt while the middle bolt shares less load [18]. The results of the simulation are shown in Table 9. The contact pressure between the bolt and the laminate was used to estimate this distribution. This result was taken as the maximum contact pressure at each single bolt divided by the sum of the maximum contact pressure of the three bolts. The maximum contact pressure is taken on the bolt shank in the contact region defined in red in Figure 37. The load distribution between the bolts appeared unaffected by the type of layup used in the joint.

Table 9: Load Distribution Between the Bolts in 3OB Joints

	B1	B2	B3
CP12	0.35	0.25	0.40
QI12	0.34	0.26	0.41

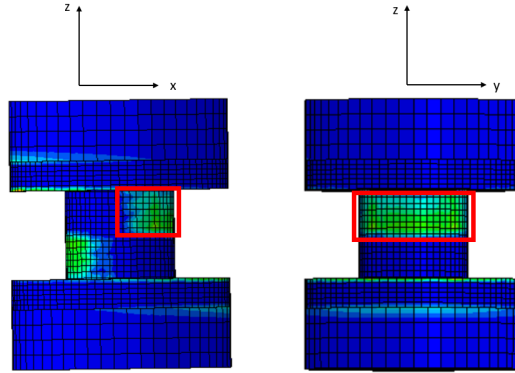


Figure 37: Region Monitored for Bolt Load Measurement

### 6.1.1.2 Adhesively Bonded Joint

The load transfer efficiency of these joints depends on the joint design (single lap in the case of this study), the adhesive characteristics and the properties of the adhesive/substrate interface. The load path in single lap joints is highly eccentric, which generates secondary bending moments yielding substantial peel stress. This drawback limits the joint strength and may require an underlying support structure in actual situations. The standard requires the use of a lap joint configuration to assess the adhesive bond shear strength. However, two limiting factors influence the result: the non-uniform stress distribution in the adhesive due to stress concentration peaks and the induced peel load. An analysis based on elastic behaviour using the actual adhesive shear modulus is appropriate when the adhesive does not experience plastic deformation at limit load.

However, in most situations, an elastic-plastic analysis is required to predict the actual joint strength that accounts for the increased shear and decreased elastic strain energy. It is to note that the influence of the operating environment (including temperature, moisture, and any solvents or fluids) on the adhesive shear stress-strain relationship, which could be important, is not considered in this study. Only cohesive failure of the adhesive is simulated as delamination at the adhesive-adherend interface does not occur. Additionally, the critical area in the adhesive is at the overlap ends where high stresses occur in shear and peel. High shear stresses develop at this location as the difference in tensile load carried by the upper and lower adherend is significant.

### 6.1.1.3 Hybrid Bolted/Bonded Joints

Knowing the strength and weaknesses of the above types of joints, the challenge is to design a hybrid form that permits adequate interaction between the adhesive and the fasteners, which can take the form of load-sharing, but also peel stress reduction in the adhesive. Although this configuration provides evident benefits of bonded strength improvement and reinforcement of the hole edges by the adhesive, it is still being determined how the bolts improve the strength of the bonded joint. Therefore, as indicated earlier, the focus of this study is to model the behaviour of this type of joint to assess the impact of adhesive properties and design considerations on its performance in carrying a tensile shear load. Furthermore, to understand how hybridization affects the classic joining methods, the stresses are monitored in their respective critical region to see if the additional component (adhesive layer for a 3OB joint and the bolts for a bonded joint) effectively reduces the stress state in these regions.

### 6.1.2 Assessment of The Behaviour of Different Joining Methods

The load-displacement relationship as predicted by the simulation is shown in Figure 38 to provide a comparison tool of the behaviour of 3OB, bonded as well as HBB joints subjected to the same loading condition until failure, for the case of each layup. It is to note that failure is defined as the onset of fibre and/or adhesive damage. Table 10 summarizes the observed failure mode and corresponding load. These results confirm the benefits of the adhesive in comparison to the fasteners, intensified by the favourable alignment of most layers in the case of the CP configuration. As for 3OB joints, the QI configuration presents a slight advantage of strength due to the presence of 45° plies increasing the joint capability of sustaining bearing loads. Also, it appears that the HBB joint behaviour and strength are similar to that of a bonded joint, suggesting that the adhesive is the main contributor to load transfer between the laminates. Additionally, bonded and HBB QI joints have a lower strength due to higher peel and shear stresses compared to CP layups, as discussed in subsection 6.1.2.4

Table 10: Failure Load of Different Joint Configurations

Model	Failure Mode	Load at Failure (kN)
CP12		
3-Bolts HBB Joint	Fiber Failure	15.41
3 OB Joint	Fiber Failure	8.72
Bonded Joint	Adhesive Failure	16.50
QI12		
3-Bolts HBB Joint	Adhesive Failure	13.78
3 OB Joint	Fiber Failure	9.01
Bonded Joint	Adhesive Failure	13.58

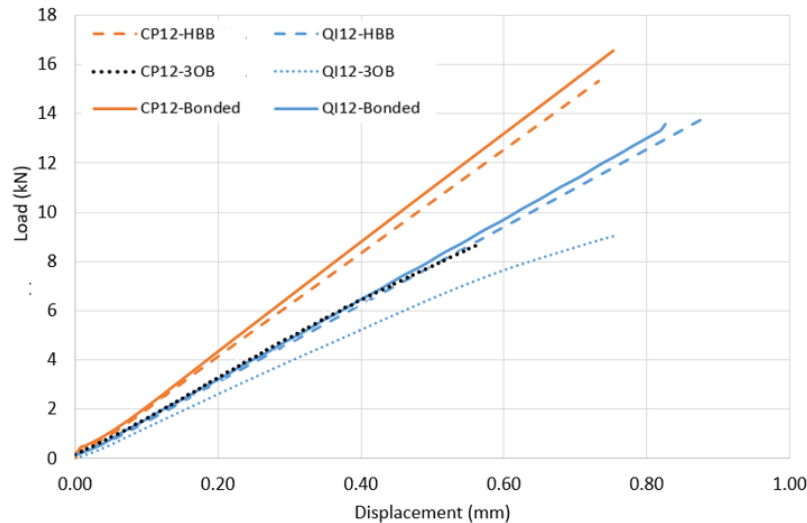


Figure 38: Load-Displacement Curves for QI and CP Joints

Concerning the failure mechanisms in HBB joints, it appears to be a combination of only bonded and only bolted joint failure. Depending on the geometric parameters of the joint such as the  $e/d$  ratio and the overlap length explored later in the thesis, as well as the adhesive and material strength,

the failure of the joint will be characterized by tensile fibre failure or adhesive failure. Thus, a more in-depth investigation is required to understand how hybridization affects the stress state at the holes and in the adhesive layer.

### 6.1.2.1 Out-Of-Plane Displacement for Different Joining Methods

Out-of-plane displacement (OPD) was monitored for the different joint configurations to see if the adhesive affected this behaviour. The OPD curves are shown for the different joining methods at different load levels in Figure 39. The results suggest that the adhesive mainly drives the hybrid joint behaviour as the HBB and the bonded joint have the same OPD curves for every load level. Additionally, compared to 3OB, it is noted that HBB joints suffer from much less OPD and that the behaviour of the joint over the overlap length is very different. In HBB joint, the adhesive layer maintains the two laminates together, even at the overlap ends, which reduces the maximum/minimum OPD by up to 84 % as shown in Table 11 but also gives a sinusoidal trend to the out-of-plane behaviour of the joint. Thus, the HBB joint will retain its original geometry better in a structure even at higher load levels compared to 3OB joints, which will exhibit higher OPD displacements.

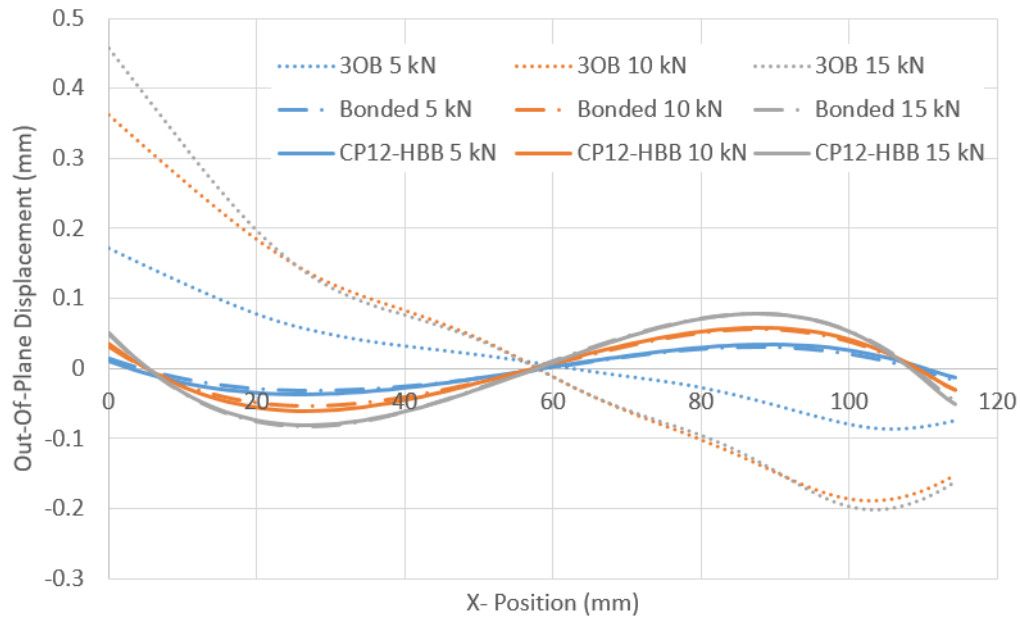


Figure 39: Out-Of-Plane Displacement for Different Joining Method at Various Load Levels

Table 11: Comparison of OPD Between 3OB and HBB Joints

	5 kN	10 kN	15kN
Maximum OPD Value For 3OB Joint (mm)	0.171	0.362	0.458
Maximum OPD Value For HBB Joint (mm)	0.035	0.057	0.079
Difference in Maximum OPD (%)	79.8	84.1	82.7

The difference in OPD behaviour between 3OB and HBB joints is mainly due to the presence of the adhesive layer. Figure 40 depicts the joint deformation under tensile shear loading. These deformations were scaled to show their pattern more clearly. Scaling was increased for the HBB joint configuration as it displayed significantly less OPD than the 3OB joint. Due to the eccentricity

in the load path, secondary bending will occur in both joints, trying to separate the laminates at the overlap ends. However, how this secondary bending affects the deformation of the joint varies significantly. In 3OB joints, this rotation at the overlap ends is unrestrained, and the joint opens up. The absence of resistance to joint opening results in large OPD at the overlap end, but also makes the variation of OPD gradual along the overlap length. In HBB joints, the adhesive layer resists the rotation at the overlap ends and keep the laminates together. The joint opening restriction imposed by the adhesive layer results in a larger OPD at a quarter of the overlap length as the laminate is subjected to the induced moment applied at the overlap ends. This phenomenon greatly affects the variation of OPD along the overlap length as the restriction of the joint opening gives a sinusoidal form to the OPD. As both ends resist secondary bending, OPD at the middle of the overlap is zero. Interestingly, the inflection points are located at the same position along the overlap length for a bonded joint, meaning this behaviour for the current HBB joint configuration is not influenced by the bolts. However, different bolts' positioning may affect the HBB joints' OPD. This will be explored in a section [6.2.3](#)

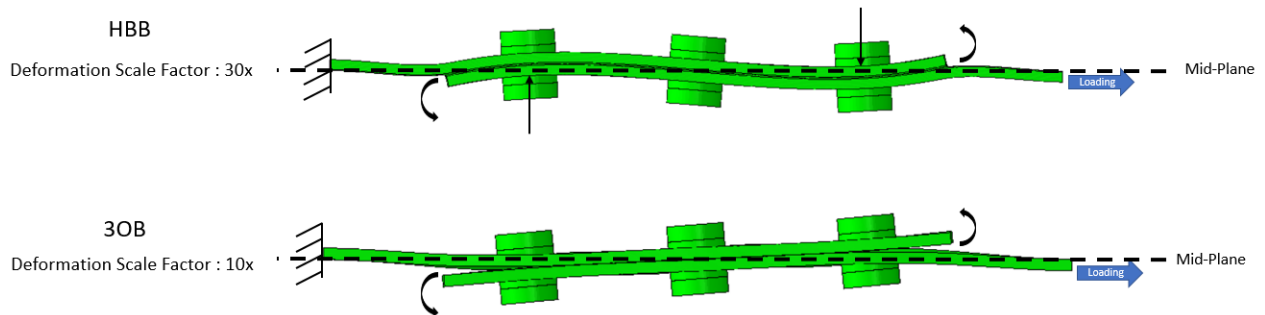


Figure 40: Scaled Out-Of-Plane Deformation of 3OB and HBB Joints at 8 kN, Case of CP

### 6.1.2.2 Longitudinal Strain Field

A meaningful comparison of 3OB versus HBB joint behaviour was conducted using the simulation model to predict the strain field generated by the same loading. The strain field analysis presented so far had the main objective of validating the simulation model against the available experimental results. Only a few conclusions on the behaviour of the joints when comparing 3OB with HBB were possible to draw from the fact that the experimental data obtained using the DIC were collected at loading levels function of the ultimate resistance of the joint, which is dependent on the type of joint and layup. In addition, the DIC technique does not allow measurements under the washer; therefore, strain fields closer to the holes, in the critical zones of concentrated stress, cannot be captured.

Examples of simulation predictions are shown in Figure [41](#) depicting strain fields for 3OB and HBB joint configurations involving CP layups loaded at the loading levels indicated at the top of each set. The analysis of the strain field around the most loaded region of the laminate reveals a net advantage of the increased strength of HBB yielded by the addition of the adhesive augmented by the favourable orientation of a higher number of plies with respect to the loading direction, for the case of CP as shown in Figure [42](#). These results suggest a significant strain concentration relief at all holes due to hybridization, but especially at the critical hole. Nevertheless, significant strain reduction at the hole due to the adhesive layer occurs only after the load in 3OB joint begins to be transferred mainly by the bolts (after 5kN), before which the 3OB joint behaves more as a filled-hole specimen where bearing induced high strains are not present. Finally, independently of

the joint configuration and layup, it is noted that the critical region where high deformations occur is at the hole corresponding to B3. This result was expected as this hole is situated closer to the grip side, meaning that only a small fraction of the load has been transferred when reaching its position. As such, much higher by-pass loads are observed at this position compared to the other holes contributing to the development of higher strains. Thus, subsequent investigations will focus mainly on this region.

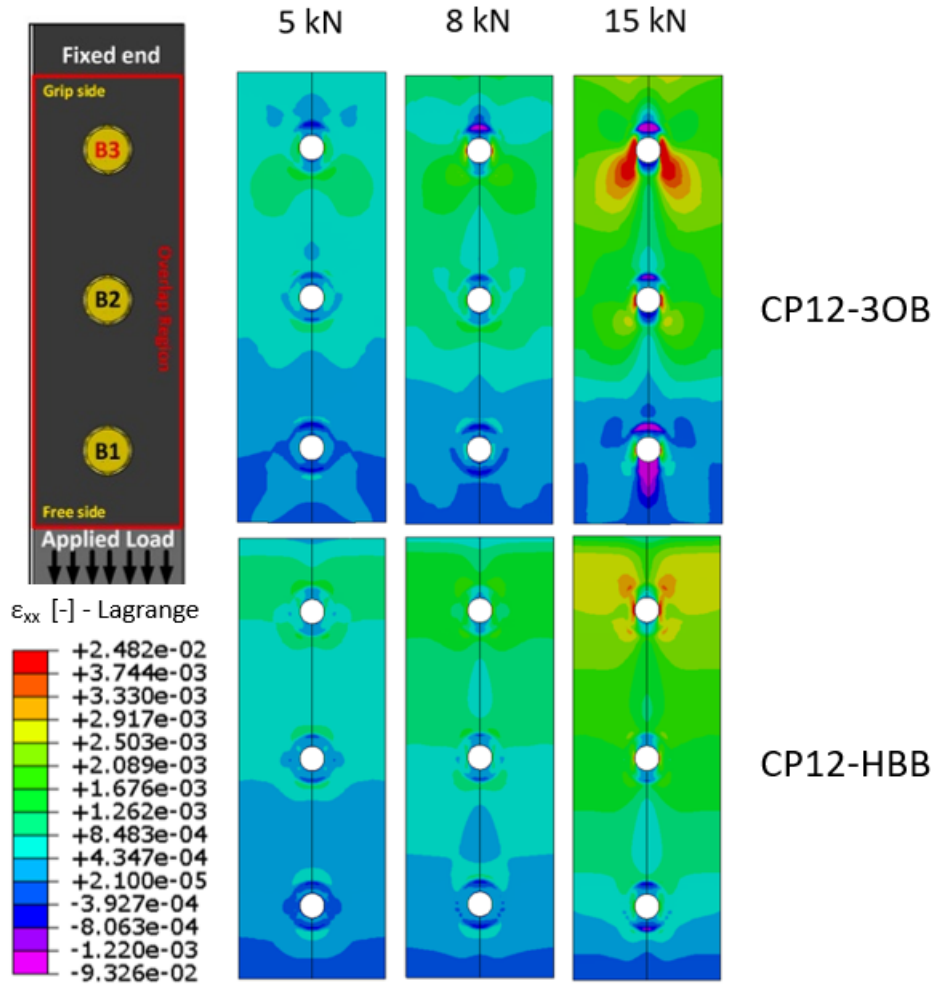


Figure 41: Simulation Top Ply Strain Field Comparison Depending on the Joint Configuration, Case of CP Layup

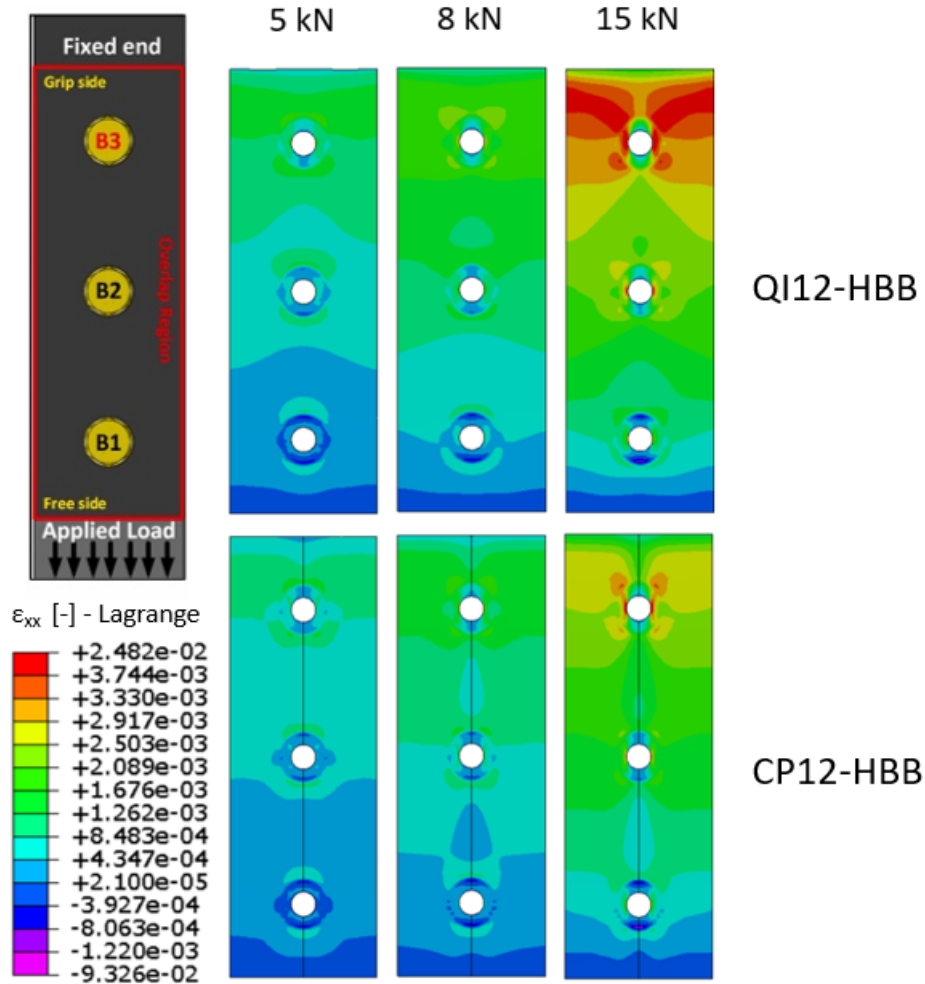


Figure 42: Simulation Top Ply Strain Field Comparison Depending on the Layup, Case of HBB Joint

### 6.1.2.3 Stress Concentration in the Laminate in HBB and 3OB Joints

The critical state of stress at the hole that generates failure consists of the combination of  $\sigma_x$  and a shear component  $S_{xy}$ . The study of the longitudinal strain field indicated that the critical hole in 3OB and HBB joints is the one corresponding to B3. Yet, a variation of the peak stress at all hole locations is of great interest to see how the joining method influences the development of those high stresses. The predicted variation of the normal stress with the imposed loading at the critical point of each hole of the top ply is depicted in Figure 43 and 44 for 3OB and HBB joints consisting of CP and QI layups, respectively. Due to the bolt preload, negligible compressive stress (around 10 MPa) is observed at very low load levels as the laminate is compressed creating a compression zone in bending. As discussed previously, the loading by-pass at each fastener location has developed a variation of stress, B3 being critical. Once the load is applied to one end of the joint, it tends to transfer through the fasteners and/or the adhesive to the other end, where a reaction load develops. For the 3OB configuration, there is a decrease in load to carry by each laminate moving from the grip side to the free side as part of it has been transferred to the second laminate. The concept of load transfer becomes more complex in the case of HBB types of joints as it involves the adhesive as well. It was found that the mechanical properties of the adhesive, as well as its resistance to stress



concentrations taking place at each end of the overlap dictates the performance of such joints. For a stiff adhesive such as the one used in this case, the holes remained unloaded and thus, significant stress reduction is observed at higher load levels, improving the performance of HBB joints. Not only is a fraction of the load already transferred by the adhesive when reaching the first hole, but there is also less matrix damage in the laminate due to another important feature of the HBB joint: the reduction of shear stresses.

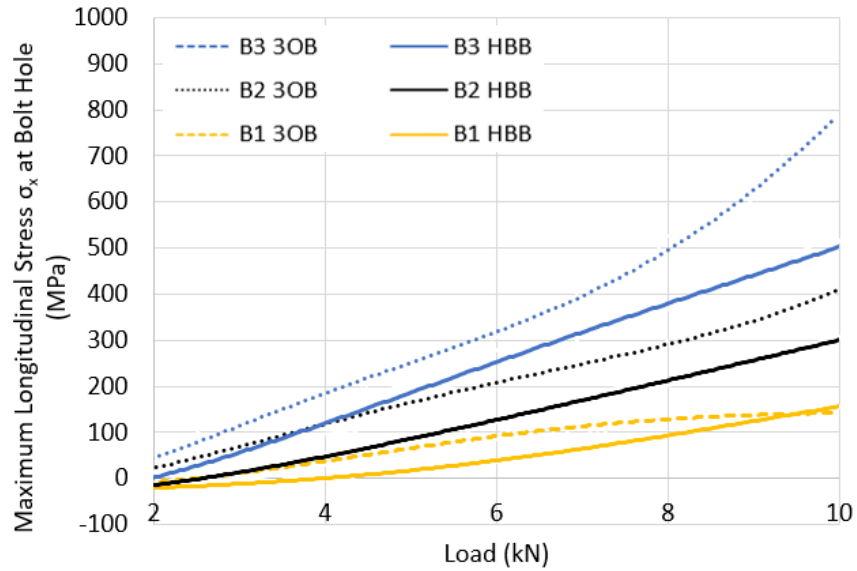


Figure 43: Maximum Longitudinal Stress  $\sigma_x$  at the Different Holes in CP Joints

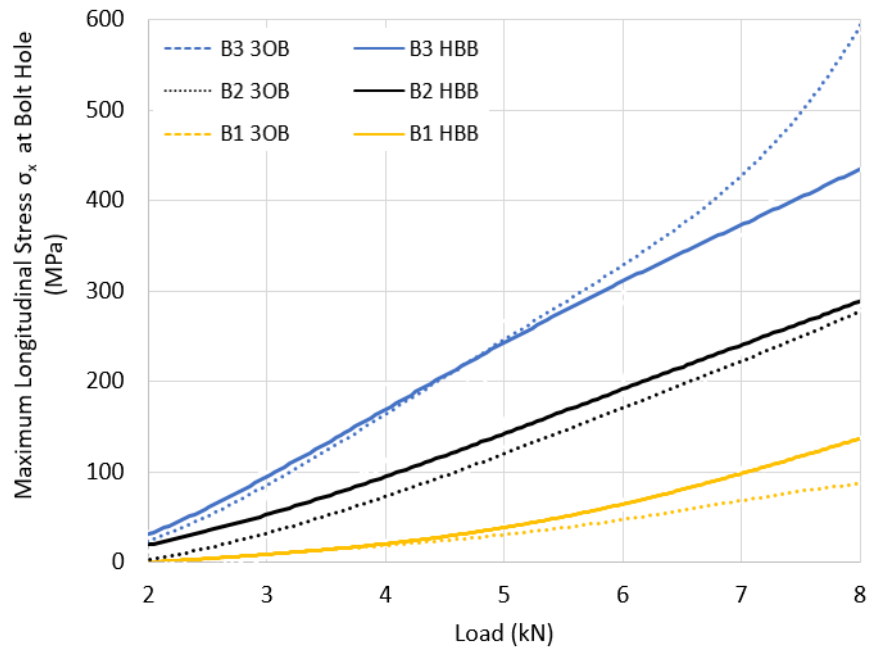


Figure 44: Maximum Longitudinal Stress  $\sigma_x$  at the Different Holes in QI Joints

For the QI layup, a slight reduction of the maximum longitudinal stress is observed for the HBB joints. However, this difference is much less apparent than in the case of the CP layup. Initially, for the QI configuration, the stresses are similar independently of the joint type, but at around 7 kN, significant contact is initiated between the bolt shank and the laminate, which creates a significant stress concentration. The difference in behaviour between the CP and QI layups can be explained by the fact that CP layups are more notch sensitive, a phenomenon reduced by the adhesive layer. This notch sensitivity relates not only to longitudinal stresses  $\sigma_x$ , but also to shear stresses  $S_{xy}$ . Thus, CP layups suffer matrix damage at a lower load level compared to QI layups due to the development of higher shear stresses, reducing the local stiffness.

As indicated above, shear stress is also present at these same points. Similar results focusing on the critical point (maximum normal stress) are summarized in Figure 45. This data indicates a net gain in the reduction of the shear stress generated by the adhesive independently of the layup. This gain becomes even more substantial with increased loading, independently of the layup type. For the CP layups, the reduction of the maximum shear stress around the holes due to hybridization is almost double compared to a QI layup, showing the significant gains that can be achieved, especially for HBB CP joints. One can conclude that the adhesive in HBB joints contributes to an important reduction of the shear stress at the critical point of the joint, thus delaying failure at the critical hole. While the holes were unloaded in this HBB joint due to the stiff adhesive, with the reduction of longitudinal and shear stresses at all load levels, hybridization is expected to lead to lower stress levels when the holes are loaded. This is expected as the adhesive would still transfer a portion of the load; thus, the holes will be less loaded than in OB joints.

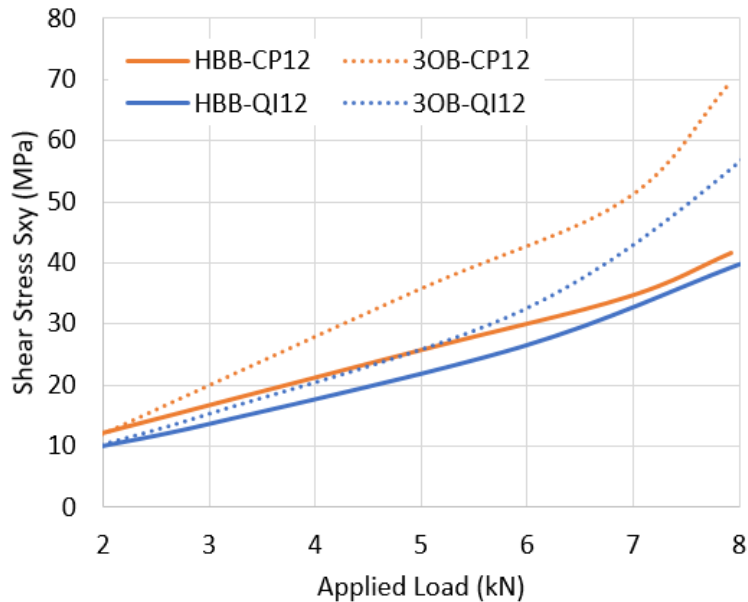


Figure 45: Shear Stress  $S_{xy}$  in  $0^\circ$  Plies for CP12 and QI12 Joints

#### 6.1.2.4 State of Stress Comparison in the Adhesive in HBB and Bonded Joints

It was determined that peel  $\sigma_z$  and shear  $S_{xz}$  stresses are critical for the adhesive in HBB and bonded joints. Specifically, the overlap ends are the regions of interest as high peel, and shear

stresses develop at these locations, as shown in Figure 46. The compressive stress around the holes is generated by the clamping load.

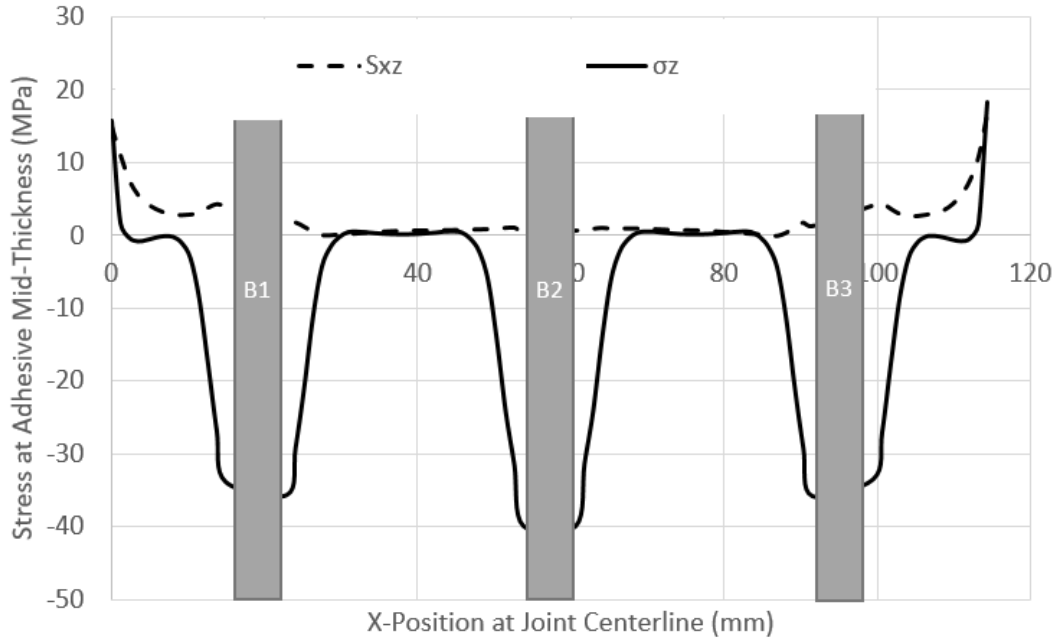


Figure 46: Stress Distribution Along the Centerline of the Adhesive Layer for HBB Joint at 8.5 kN

The high stresses result from three main factors: the relative displacement of the two laminates in the  $x$  direction, the difference in the load carried at the bottom of the top and at the top of the bottom laminates and the secondary bending. This difference in longitudinal stress in the laminate at the adhesive interface at the overlap end is especially significant, as depicted in Figure 47. This large difference will result in shearing of the adhesive. It can be seen that the increase in the difference of longitudinal stress in the laminates matches the increase in shear stress in the adhesive layer. This difference in longitudinal stress between the top and bottom laminates is attributed to the fact that at the beginning of the overlap, no load has been transferred in one laminate, while all the load has been transferred by the other. This difference in longitudinal tensile stress is also increased by secondary bending.

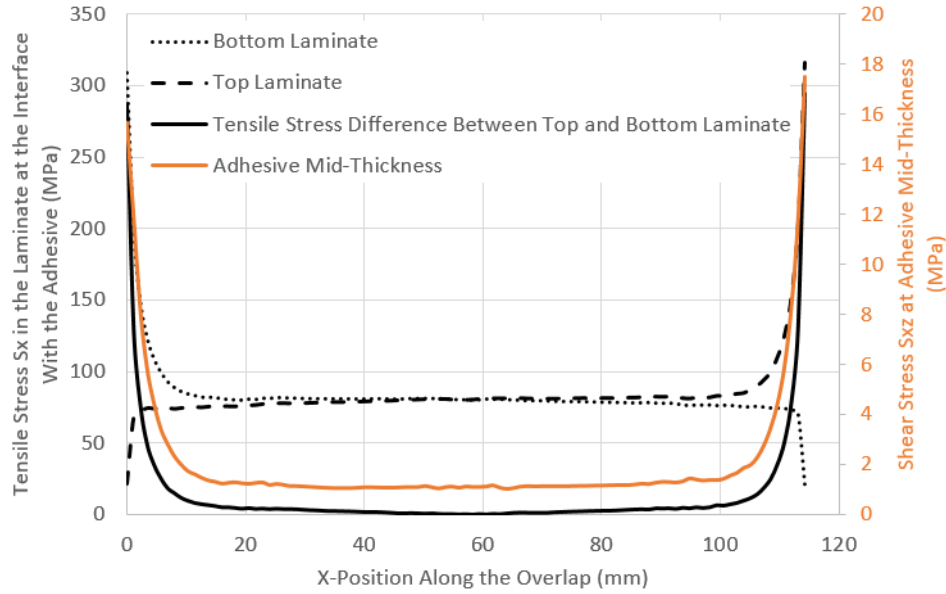


Figure 47: Stress Distribution in the Laminate and the Adhesive in HBB Joints, Case of CP at 8kN

As shown in Figure 48, secondary bending increases the difference of tensile stress between the two laminates by creating an additional tensile stress component due to the moment induced by the eccentricity in the load path. Additionally, the secondary bending phenomenon, explained previously, causes high peel stresses as the laminates are forced away from each other but maintained together by the adhesive. This pulling-apart action by the laminate generates tensile stress in the adhesive layer. Secondary bending also affects the shear stresses  $S_{xz}$  at the overlap end due to the joint's rotation. The increase in tensile stresses due to secondary generates a larger difference between the longitudinal stresses between the top and bottom laminates resulting in higher shear stresses.

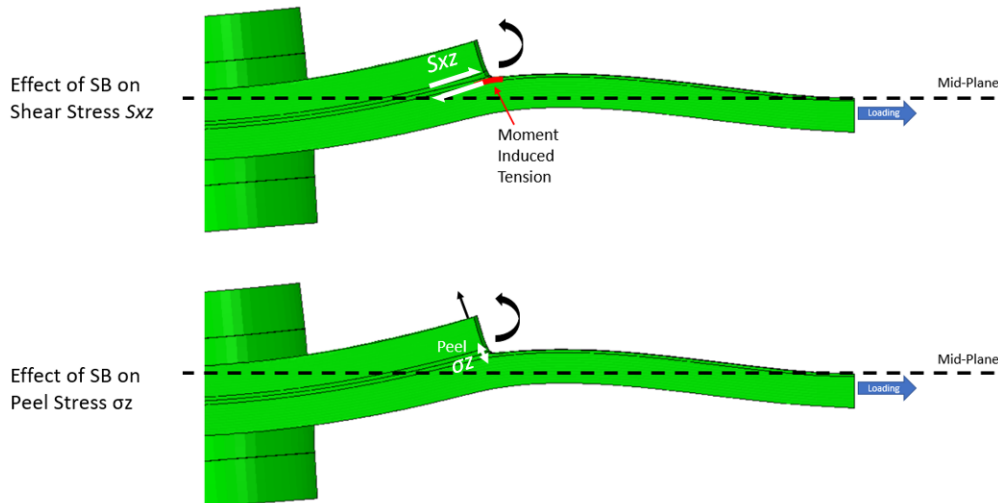


Figure 48: Effect of Secondary Bending on HBB Joint, Case of CP-HBB Joint at 8kN (Deformation Scale 50x)

The case of a QI-HBB joint at 12.5 kN (before QI-HBB joint failure) was chosen to illustrate

the variation of the critical stresses along the edge of the adhesive (y-axis) as shown in Figure 49. Similar results obtained for a QI only bonded joint were added for comparison. It is interesting to note that the highest peel stresses are located along the joint centreline. This may be due to the load resultant being aligned with the joint centreline. However, this phenomenon was not seen in CP layups; thus, this may be due to the lower transverse stiffness of the QI layups or the presence of  $\pm 45^\circ$  plies. These preliminary results indicate that the bolts are redundant in the sense that failure is dictated by the stress levels at the edge of the adhesive layer and these are unimpacted by the presence of the bolt in the current HBB joint configuration. CP layups deviated slightly from this observation as bolts not only did not contribute to reducing the stress state in the adhesive layer, but the bolt holes induced stress concentrations which drives the failure of the HBB joint at a lower load level compared to the bonded joint. This highlights the importance of considering HBB joints as unique for their design and cannot be designed as bolted joints to which an adhesive layer is added.

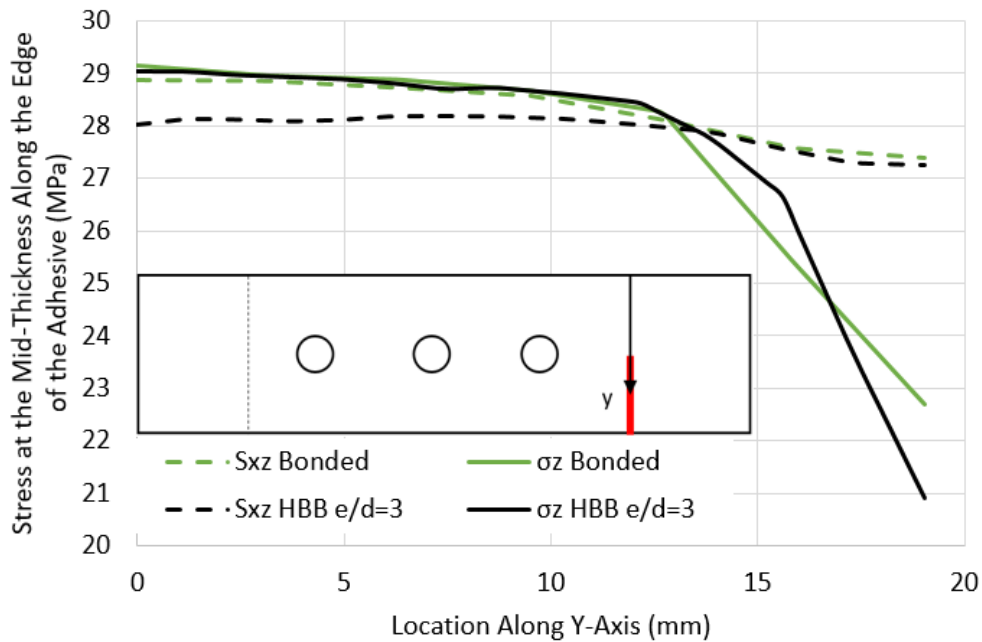


Figure 49: Peel  $\sigma_z$  and Shear Stress  $S_{xz}$  Distribution along the Adhesive Edge in QI HBB and Bonded Joints at 12.5 kN

Additionally, the layup was found to influence the stress levels in the adhesive, as shown in Figure 50. For the same load level, the adhesive in the QI-HBB joint will be more stressed in peel and shear than in the CP-HBB joint. This is why CP bonded joints performed better than QI bonded joints. The difference in peel stresses can be attributed to the fact that CP layups are much stiffer than QI layups due to the higher  $0^\circ$  ply count. Since a correlation exists between longitudinal stiffness and bending stiffness, the same comparison can be made regarding the superior bending stiffness of CP layups meaning less out-of-plane displacement is observed for a joint using a CP layup, as shown in Figure 51. Thus, the adhesive does not have to hold the CP laminates together as much as it does when QI laminates are used. It is also further emphasized that the main contributors to adhesive damage are  $S_{xz}$  and  $\sigma_z$ . The in-plane shear stresses  $S_{xy}$  are so low that it is an insignificant contributor to adhesive failure.

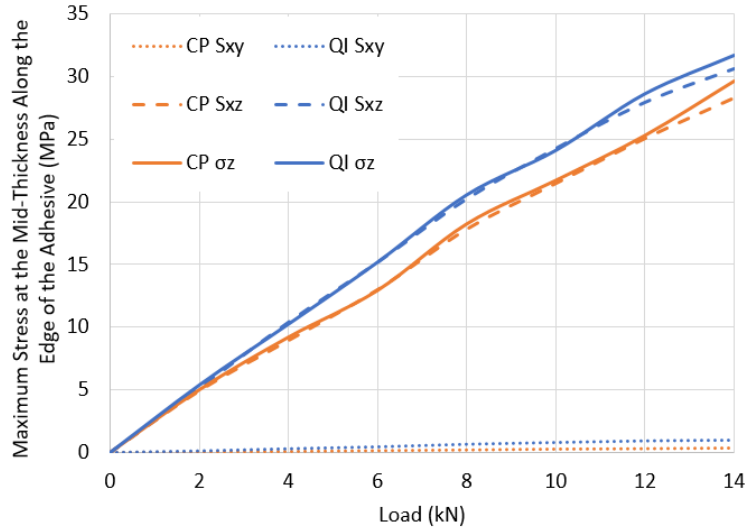


Figure 50: Comparison of Stresses in the Adhesive Layer for QI and CP HBB Joints

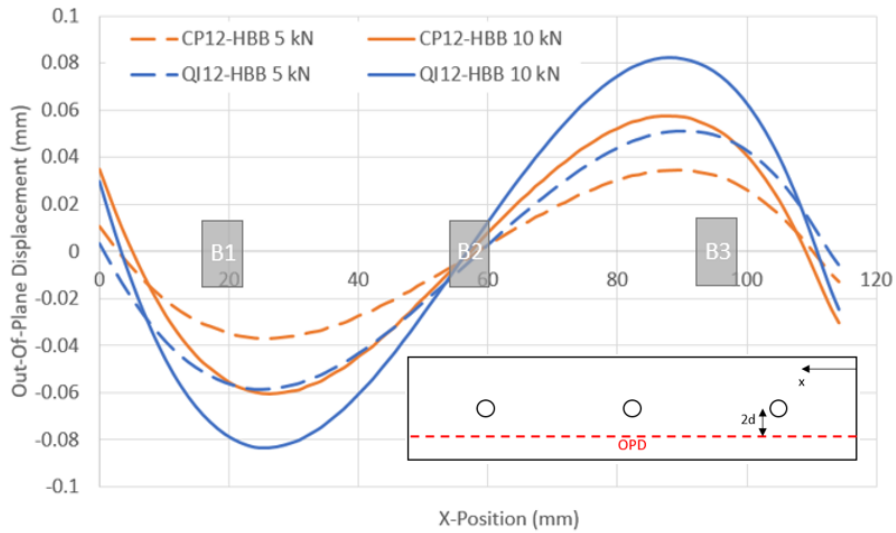


Figure 51: Comparison of the Out-of-Plane Displacement for QI and CP HBB Joints

Additionally, the increased shear stresses  $S_{xz}$  in the adhesive for QI layups can be attributed to another phenomenon also influenced by the laminate stiffness: the relative displacement between the two laminates. As shown in Figure 52, due to their lower stiffness, QI HBB joints display more significant relative displacements between the laminates, increasing the shear stress levels  $S_{xz}$  in the adhesive at the overlap ends.

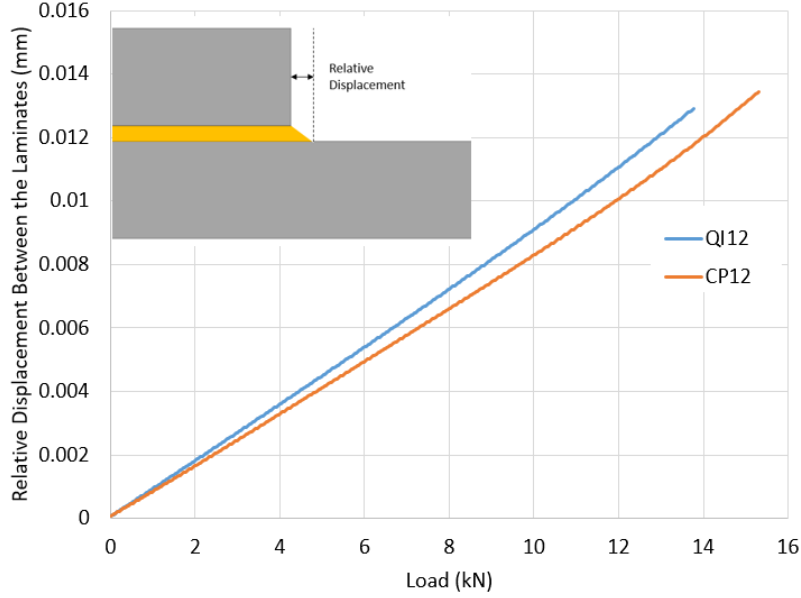


Figure 52: Relative Displacement Between the Laminates for QI and CP HBB Joints

### 6.1.3 Summary of Effect of Hybridization

From this investigation, the key benefits of hybridization for a bolted joint have been highlighted by the reduction in shear stresses as well as the reduction of tensile stress at the holes provided by the adhesive layer. However, while this may seem interesting, the holes still generate considerable stress concentrations in the HBB joint. Thus, the HBB joint design must optimize the role of the bolts such that they contribute to a reduction of stresses in the adhesive layer to justify the presence of such discontinuity in the laminates. Still, preliminary results show that for a typical bolted joint configuration  $e/d=3$  to which a stiff adhesive layer is added (corresponding to the ASTM-D5961 standard geometry tested experimentally); the bolts did not influence the stress state at the overlap ends in the adhesive where stresses are high. Thus, the next section will focus on potential parameters that could permit stress reduction in the adhesive layer by the bolts.

## 6.2 Investigation of Design Parameters to Optimize HBB Joints

### 6.2.1 Role of Middle Bolt in 3-Bolts HBB Joints

Improvements in HBB joint design may take the form of an increase of the joint load-carrying capability, but also a joint weight reduction for the same load carrying capability. The latter will be investigated first as Gamdani and al. [7] indicated a potential redundancy of the middle bolt in 3-bolt HBB joints. For that reason, models were developed with the same overlap length, but one had three bolts and the other two bolts. Simulations were run for CP and QI layouts, and it was found that the removal of the middle bolt did not influence the failure load of the joint, as shown in Table 12.

Table 12: Failure Load for Different HBB Joint With and Without Middle Bolts

Model	Failure Mode	Load at Failure (kN)
CP12		
3-Bolts $e/d=3$	Fibre Failure	15.41
2-Bolts $e/d=3$	Fibre Failure	15.30
QI12		
3-Bolts $e/d=3$	Adhesive Failure	13.78
2-Bolts $e/d=3$	Adhesive Failure	13.94

In order to understand the reason for the similar joint strength upon the removal of the middle bolt, stresses around the critical hole were monitored for the HBB joint using CP and QI laminates. It was shown previously that at B3, located on the grip side, the longitudinal tensile stresses were much higher than at the hole on the free side, making this location the focus for the stress levels comparison. It is found that the presence of the middle bolt does not alleviate the stresses at the critical hole, as shown in Figure 53 for the CP case. For a configuration where the bolts transfer loads between the laminates, increasing the number of bolts effectively decreases the load fraction transferred by each bolt, reducing the bearing load applied at each hole. However, in this case, the load is being transferred uniquely by the adhesive, a common phenomenon when using a stiff adhesive in HBB joints, which means that the stress levels are independent of the presence of the middle bolts.

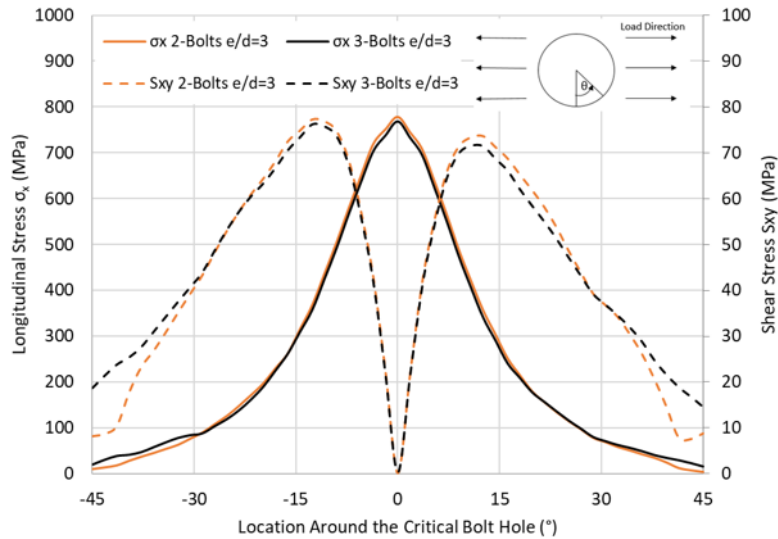


Figure 53: Tensile  $\sigma_x$  and Shear Stress  $S_{xy}$  Distribution Around the Critical Hole in CP-HBB Joints at 14 kN

Similarly, the stresses were monitored in the adhesive at the overlap ends. As was the case for stresses at the critical hole, there is no significant difference between each configuration. The stress distribution shown in Figure 54, for the CP case taken as a basis for this comparison, highlights that although slight discrepancies are observed, the removal of the middle bolt did not significantly affect the stresses in the adhesive layer. This result further emphasizes that the middle bolt in HBB joints is redundant.



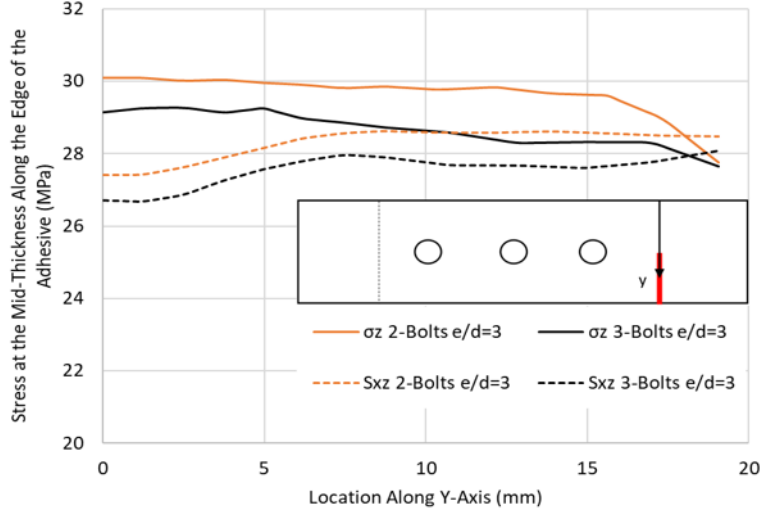


Figure 54: Peel  $\sigma_z$  and Shear Stress  $S_{xz}$  at the Overlap Ends in CP-HBB Joints at 14 kN

Although not captured by the simulation, crack propagation due to initial flaws must be discussed in this section. Crack stopping provided by the bolts is a great advantage of hybridization as determined experimentally [7, 8]. Even when removing the middle bolt, it is unlikely that this crack-stopping advantage would be reduced as cracks should initiate in the highly stressed regions (the overlap end for the adhesive). Thus, cracks would be drawn towards the outer bolts and stopped at that point. Even if a middle bolt was present, cracks should not reach their location. Also, upon manufacturing HBB joints, bolts are typically installed after applying the adhesive layer. As such, bolts do not help control the bondline and adhesive quality upon application. Additionally, considering a potential load sharing between the bolts and the adhesive, although increasing the number of fasteners reduces the load levels of the individual holes in 3OB joints, this is unlikely to translate for HBB joints. The reason is that researchers have suggested that load sharing may occur only when high plastic deformation is observed in the adhesive. While this will be confirmed in the next section, the development of high stresses in the adhesive layer is required to trigger the plastic behaviour. However, as shown previously, the critical regions in the adhesive are at the overlap ends, with the adhesive in the middle section of the overlap being very lightly stressed. Thus, plasticity should develop only at the outer bolts leaving the middle bolt unable to transfer any loads.

It is observed that the removal of the middle bolt did not affect the stress levels at the critical hole nor at the overlap ends in the adhesive and that any potential enhancing behaviour would not rely on the presence of the middle bolt, such as the load-sharing phenomenon and crack stopping. As such, for an overlap length requiring more than one bolt to maintain an  $e/d=3$ , it is recommended that only two bolts are used. These bolts between the outer bolts are considered redundant and will only add weight to the joint.

### 6.2.2 Load-sharing

Experimental studies have demonstrated that simultaneous load-sharing between the bolts and the adhesive in HBB joints can increase its performance compared to bonded joints. With a 3-bolt HBB joint configuration having a 10  $\mu\text{m}$  bolt-hole clearance using the Araldite® LY 8601/Aradur® 8602 Epoxy as the adhesive, it was determined that no load-sharing was observed as the bolt shank never initiated contact with the laminate. Thus, parameters such as the overlap length and the adhesive properties were explored to see if load-sharing is possible before the first significant failure

event (fibre damage/adhesive damage initiation) in HBB joints. For this section, Adhesive 1 is the Araldite® LY 8601/Aradur® 8602 Epoxy, a stiff, brittle adhesive used in the experimental tests, and adhesive 2 is the EA 9361 Epoxy, a high plastic deformation, low stiffness adhesive commonly used in load-sharing studies. The tensile stress-strain curves for both adhesives are shown in Figure 55.

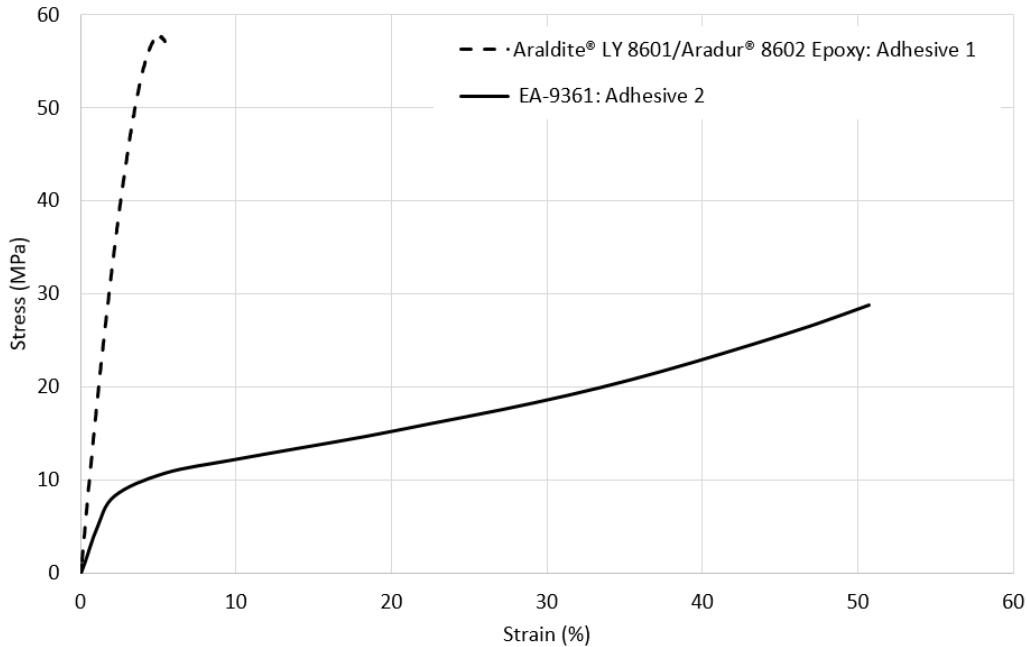


Figure 55: Tensile Stress-Strain Curves of the Adhesives Used in the load-sharing Study

Simulations were run for three different overlap lengths (OL) of 38.1 mm, 76.2 mm and 114.3 mm, all using the CP12 layup with an  $e/d$  ratio of 3. The bolts were removed from the models to see how the top and bottom laminate holes close up as the tensile load is applied to the laminates. An overclosure of 0 would mean that the holes from the top and bottom laminates are perfectly aligned, and as such, the clearance between the bolt shank and the laminate is equivalent to the initial bolt-hole clearance. Additionally, two adhesives were tested to see how high plastic deformation may help increase the hole overclosure. In order to achieve load-sharing between the bolts and the adhesive, the overclosure must be at least the value of the initial bolt-hole clearance. In the aerospace industry, the typical bolt-hole clearance used is 0 to 80  $\mu\text{m}$  for composite bolted joint as a reference [18].

Figure 56 shows the hole overclosure for the different configurations simulated. For adhesive 1, a brittle adhesive, very slight hole overclosure is achieved before joint failure. Therefore, this adhesive, independently of the overlap length, shows no promise of potential load-sharing between the bolts and the adhesive. On the other hand, adhesive 2, which displays high plastic deformation, has more hole overclosure, especially at medium to high load levels. It can be noted that adhesive 2 has a Young's Modulus around four times lower than adhesive 1. Initially, even in the absence of plastic deformation, the hole overclosure for the stiffer adhesive is lower than for adhesive 2. The lower adhesive stiffness permits greater shear deformations of the adhesive layer, increasing the relative displacement between the top and bottom laminates. However, it appears that the adhesive Modulus has a negligible impact on load-sharing in HBB joints as the hole overclosure in the absence

of plasticity is still very small. Thus, relying on a low Young's Modulus adhesive would unlikely permit simultaneous load transfer between the bolts and the adhesive. For shorter overlap lengths, hole overclosure is higher at the same load compared to longer overlap lengths. This is because hole overclosure is highly dependent on the plasticizing of the adhesive. Significant hole overclosure occurs only when plastic deformation in the adhesive, which starts at the overlap ends, reaches the hole. For that reason, shorter overlap lengths benefit from an increased hole overclosure at lower load levels, as the shorter overlap length increases the stresses in the adhesive layer resulting in premature plastic deformation, as shown in Figure 57. However, even though significant hole overclosure occurs at a lower load level, the load interval during which significant hole overclosure is observed is similar for the different overlap lengths. Thus, changing the overlap length would not necessarily optimize the load-sharing process.

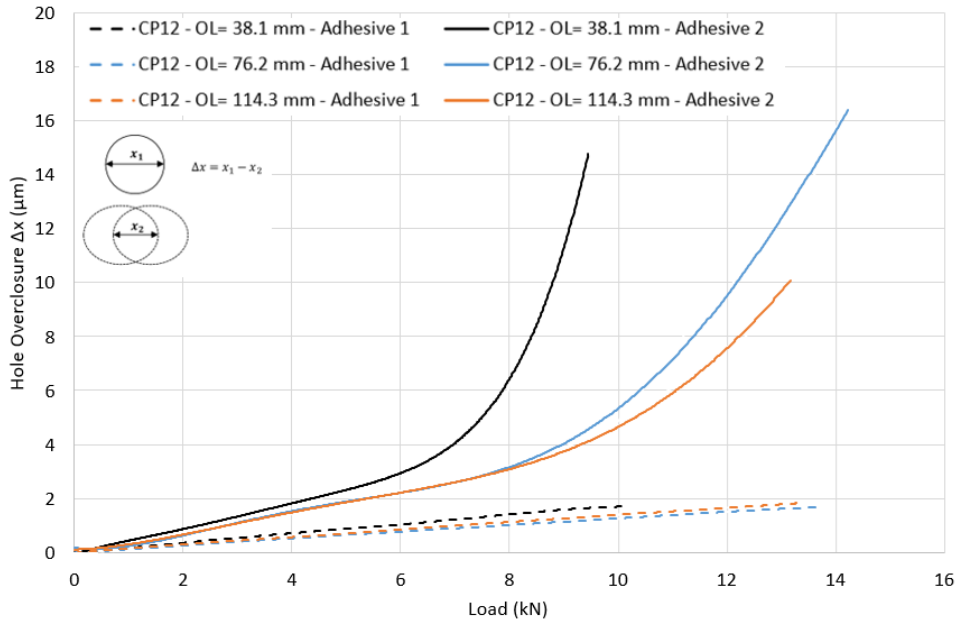


Figure 56: Hole Overclosure for Different Overlap Length and Adhesive

As mentioned earlier, the peel stresses increased drastically at the overlap ends when reducing the overlap length. The shear stresses had the same trend of increasing for shorter overlap ends. It is shown in Table 13 that as the overlap length increases, the joint's design failure load is increased because of the lower stresses in the adhesive layer. However, increasing the overlap length is more beneficial in reducing peel stresses as the difference between shear and peel stresses is more significant for shorter overlap lengths. Still, it can be seen in Figure 57 that, for longer overlap lengths, increasing it becomes less efficient at reducing stresses, especially in shear, in the adhesive layer.

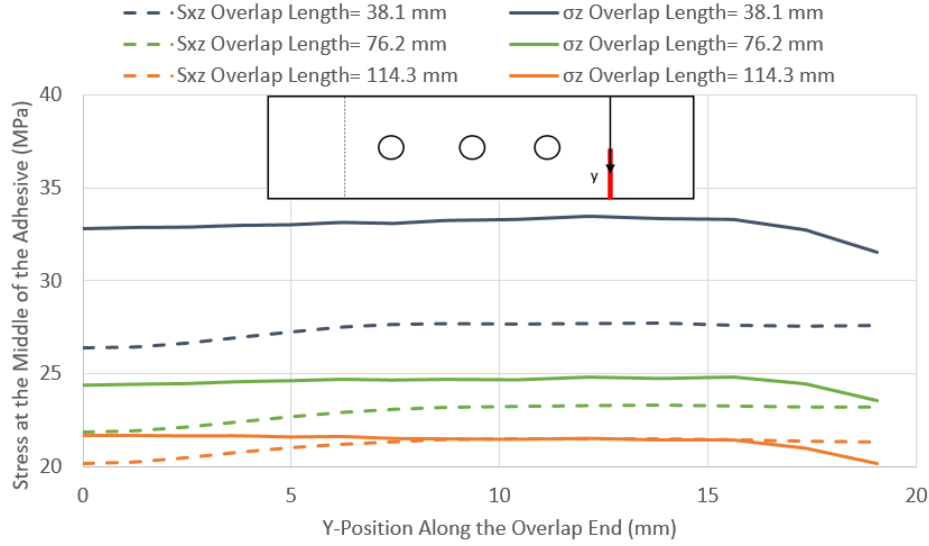


Figure 57: Peel  $\sigma_z$  and Shear  $S_{xz}$  Stresses at the Overlap End in CP-HBB Joints Using Araldite® LY 8601/Aradur® 8602 Epoxy at 10 kN

Table 13: Failure Load of HBB Joint Using Araldite® LY 8601/Aradur® 8602 Epoxy for Different Overlap Length

Overlap length (mm)	Failure Load (kN)	
	CP12	QI12
38.1	10.42	9.74
76.2	13.79	12.74
114.3	15.41	13.78

As mentioned earlier, plastic deformation plays a crucial role in the level of hole overclosure displayed by the joint. To highlight this, the maximum principal plastic strain was monitored from the hole edge to the overlap end, as shown in Figure 58. Plastic strain develops initially at the overlap ends as they are the most stressed regions in the adhesive. As expected, when the applied load increases, the plastic strains in the adhesive increase. However, this increase and even the apparition of plasticity depend highly on the overlap length and the adhesive used. As the overlap length increases, the stresses developing in the adhesive are reduced, and as such, the development of plastic behaviour is delayed.

Also, adhesive 1 was qualified earlier as brittle and did not display significant hole overclosure. In Figure 58, it can be seen that very little plasticity is developed in the adhesive, even at higher load levels (note the scale 10 times smaller compared to adhesive 2). Significant overclosure occurs only when plastic deformation reaches the vicinity of the hole. Significant hole overclosure is observed at 7 kN for an overlap length of 38.1 mm and at 9 kN for an overlap length of 76.2 mm, both using adhesive 2. Plastic deformation in the two configurations has reached the same location along the x-axis at these load levels. Thus, this suggests that plastic deformation is required to achieve considerable hole overclosure. Thus, high stresses in the adhesive layer may seem desirable to trigger plastic deformation, but this will only allow load-sharing to occur at a lower load level, not over a larger interval of the applied load.

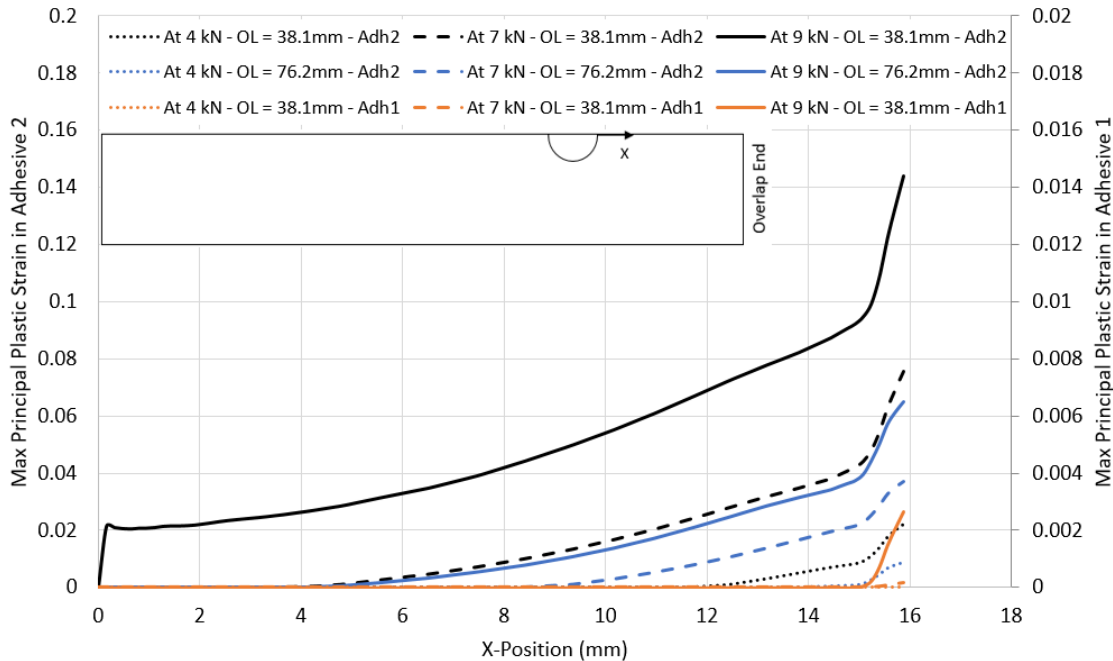


Figure 58: Hole Overclosure for Different Overlap Lengths and Adhesives

While the overlap length and the type of adhesive properties were investigated and it was determined that plastic deformation was vital in achieving load-sharing in HBB joints, other parameters were identified as impacting load-sharing. Two additional parameters were monitored: the laminate thickness and the layup type. As shown in Figure 59, thinner laminates produced slightly lower hole overclosure of the joint. This is explained by the lower stresses developing in the adhesive resulting from the lower secondary bending generated by the reduction of the eccentricity in the load path. This result suggests that thicker laminates are preferable for achieving greater hole overclosure. Due to the increased bearing area, it is also well known that thicker laminates perform better in bolted joints. As such, in the event of a load-sharing occurrence, the thicker laminate would perform better than a thinner one.

Additionally, the greater hole overclosure of QI layups can be explained by two main differences between CP and QI layups: the relative displacement between the laminates and the hole elongation. It was shown in sub-section 6.1.2.4 that QI layups display higher relative displacements between the laminates, which would more rapidly de-align the holes and thus generate higher hole overclosure. The other important factor affecting the difference in hole overclosure between the layup types is the greater longitudinal hole elongation exhibited by the CP layups, as shown in Figure 60. Even if the relative displacement were the same between the laminates, the greater hole elongation would mean that it would be more challenging to close the gap between the holes. These differences in behaviour between CP and QI layups are the main contributors to the increased overclosure displayed by the joints using the stiff adhesive, as no significant plastic deformation is displayed by them. Thus, when using a highly plastically deformable adhesive, it is anticipated that the effect of using a QI layup will be greater as it was shown earlier that QI layups generated more stresses in the adhesive layer than CP layups, which would increase plastic deformation, resulting in greater hole overclosure.

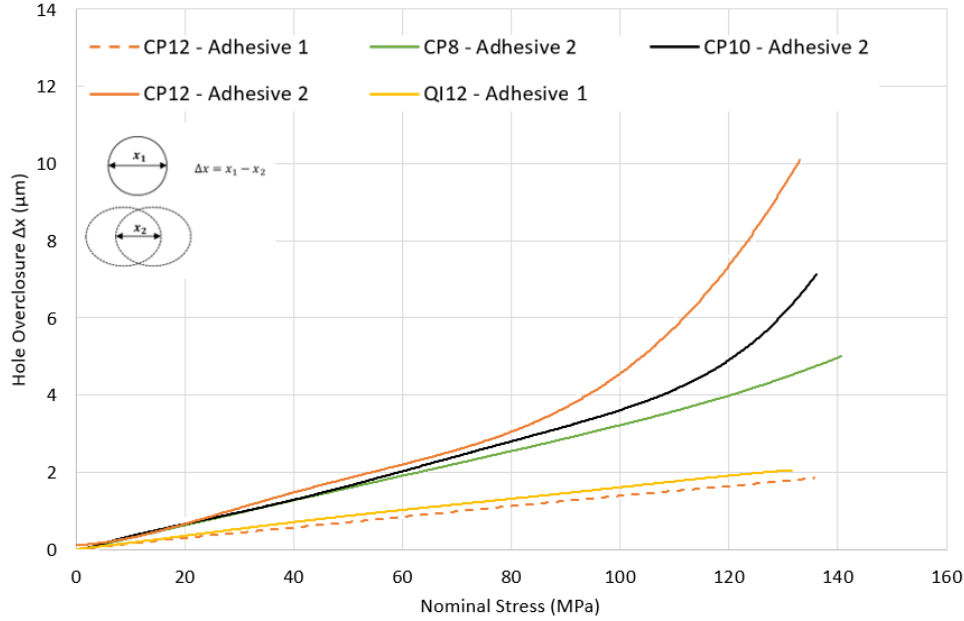


Figure 59: Hole Overclosure for Different Joint Parameters and Adhesive With an Overlap Length of 114.3 mm

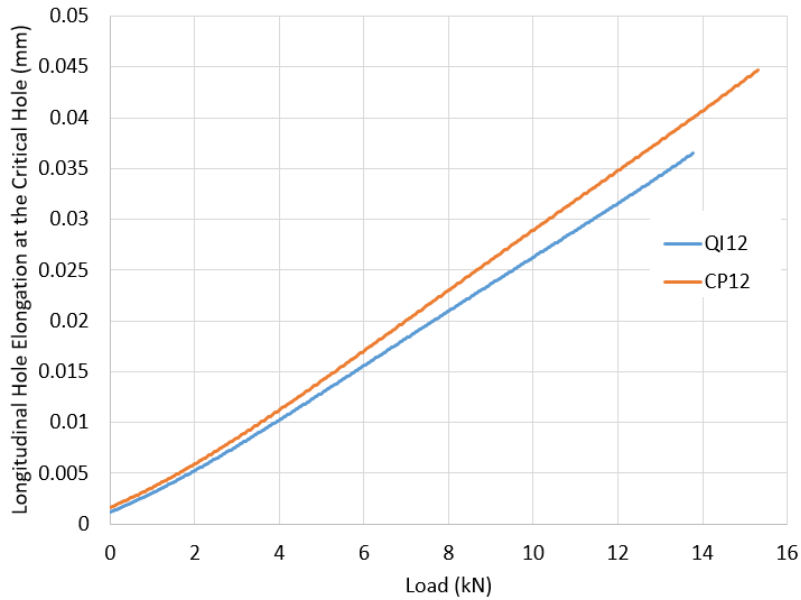


Figure 60: Longitudinal Elongation of the Critical Hole in HBB Joints For Different Layouts

Although some configurations showed more promise in achieving simultaneous load-sharing between the bolts and the adhesive, the hole overclosure remained relatively small. For the studied parameters, decreasing the adhesive yield strength, decreasing the adhesive modulus and using QI layouts instead of CP layouts increased the load-sharing potential of the joint. While other parameters did increase the hole overclosure at lower load levels, such as the decrease of overlap length and increase of laminate thickness, these were deemed inefficient means to trigger hole overclosure as they relied on increasing the stress levels in the adhesive layer. This is considered unproductive

as while greater hole overclosure is achieved at lower load levels, joint failure is decreased. Thus, the load-sharing window is not necessarily increased (interval between significant overclosure and failure load). Still, due to the small overclosure achieved very small manufacturing tolerances would be required to achieve small bolt-hole clearance, which may not be realistic. Thus, other means of increasing the design failure load of HBB joints should be explored.

### 6.2.3 Influence of $e/d$

In HBB joints, for an overlap length under 114.3 mm, almost independently of the layup (CP or QI), adhesive damage initiation was the design limit for the joint. As such, a study on the variation of the  $e/d$  ratio was conducted to see if placing the bolts closer to the overlap ends would delay adhesive failure and increase the design failure load of the joint. Interesting results were observed as shown in Table 14 where a reduction of the  $e/d$  ratio resulted in a lower failure load of the joint for CP and QI layups. Furthermore, not only the failure stress was reduced with decreasing  $e/d$  ratio, but in the case of the CP layup, it changed the failure mode from fibre failure to adhesive failure. Thus, a lower  $e/d$  ratio is suspected of increasing stress in the adhesive layer.

Table 14: HBB Joint Failure Load for Various  $e/d$  Ratio

Model	Failure Mode	Load at Failure (kN)
CP12		
2-Bolts $e/d=3$	Fibre Failure	15.30
2-Bolts $e/d=2$	Fibre Failure	14.86
2-Bolts $e/d=1.5$	Adhesive Failure	14.24
QI12		
2-Bolts $e/d=3$	Adhesive Failure	13.94
2-Bolts $e/d=2$	Adhesive Failure	13.21
2-Bolts $e/d=1.5$	Adhesive Failure	12.73

To verify the hypothesis of a stress increase in the adhesive layer for a shorter  $e/d$  ratio, the peel and shear stresses are monitored at the overlap ends just before failure in CP and QI HBB joints. One would expect that the benefit of placing the bolts closer to the overlap ends would be a reduction of peel stresses. It was determined that the maximum/minimum OPD, occurring at approximately a 1/4 and 3/4 of the overlap length, was effectively reduced for a shorter  $e/d$  ratio, as shown in Figure 61. The bolts placed closer to the edge were able to limit the out-of-plane displacement variation angle, resulting in lower maximum OPD values.

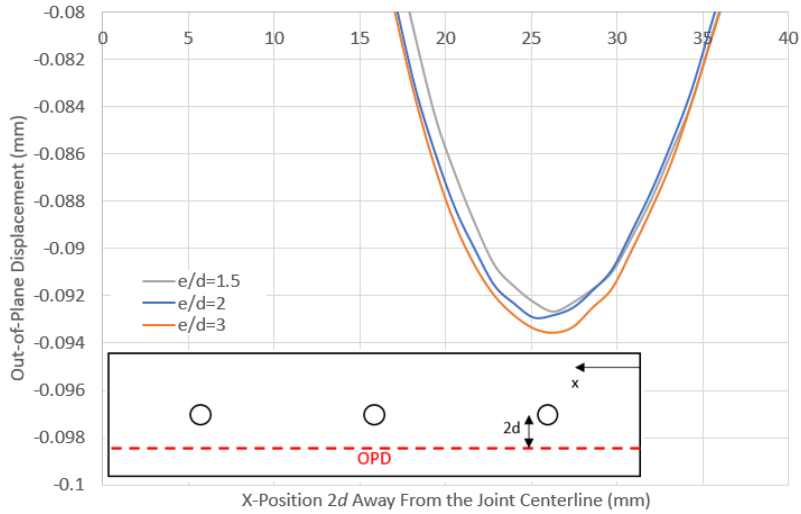


Figure 61: Out-of-Plane Displacement Near the Free Side in QI-HBB Joints With Different  $e/d$  ratio at 12.5 kN

However, this OPD min/max reduction did not translate to a reduction of peel stresses as it is noted that a lower  $e/d$  ratio results in a significant increase of peel stress for both CP and QI layups, as shown in Figure 62 for the QI layup. It appears that the bolt position influences greatly the undulation generated in the joint not only at the max/min location but also at the overlap end as shown in Figure 63 where the red arrows indicate the end position of the washer. The OPD behaviour impact on the stress state in HBB joints appears to be more significant at the overlap end, explaining why shorter  $e/d$  ratios generate higher peel stresses.

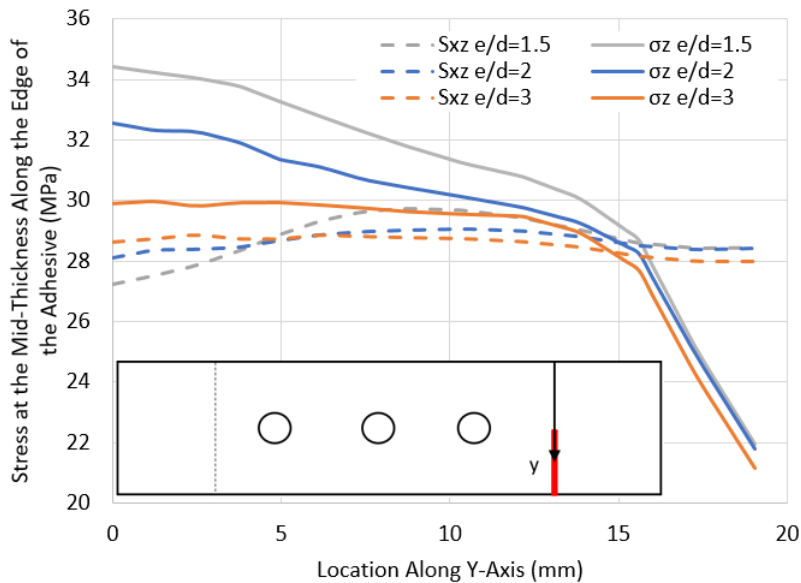


Figure 62: Peel  $\sigma_z$  and Shear  $S_{xz}$  Stresses at the Overlap End in QI-HBB Joints at 12.5 kN



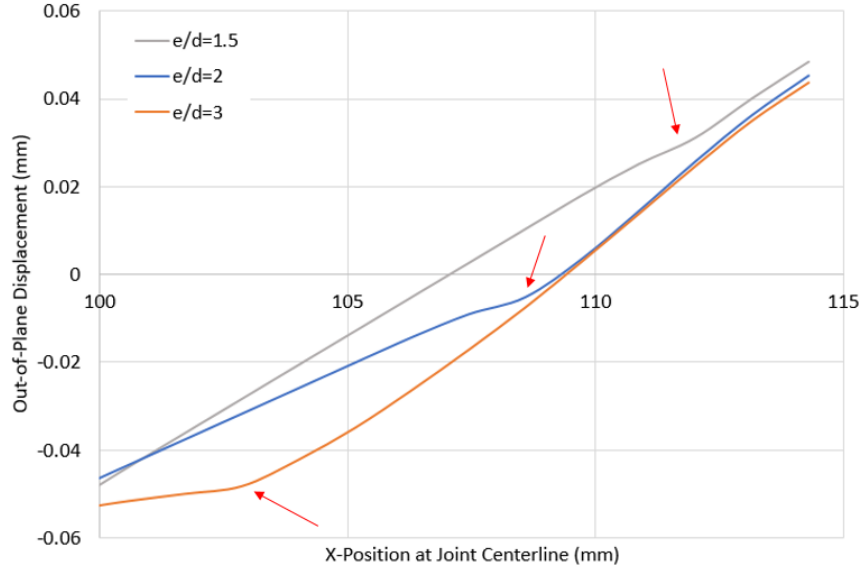


Figure 63: Out-of-Plane Displacement Near the Grip Side in QI-HBB Joints With Different  $e/d$  ratio at 12.5 kN

As shown in Figure 64, when the washer is moved closer to the overlap end, the rotation of the bolt increases the effect of secondary bending by forcing greater out-of-plane displacement at the end of the overlap. For larger  $e/d$  such as 3, the rotation of the bolt does not seem to affect the behaviour at the overlap end, as the effect of the bolts is mostly local. This also highlights that the peel stress reduction due to the clamping action of the bolts may well be only observed in the vicinity of the washer. Shear stresses in the adhesive remain unaffected by the change in  $e/d$  ratio, which can be surprising when looking at the effect on stresses at the hole where the increased proximity with the overlap acts as a significant stress riser. Ultimately, the change in the position of the hole does not influence the shear stresses  $S_{xz}$  in the adhesive as the same overlap length is conserved, and the stress concentration region around the hole does not reach the overlap ends even for an  $e/d$  of 1.5.

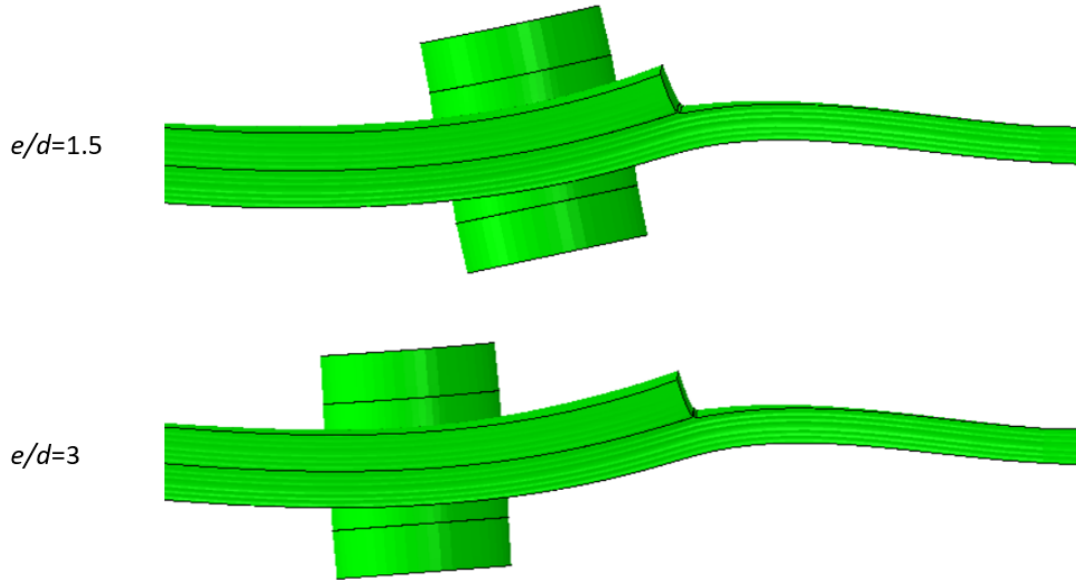


Figure 64: Effect of Bolt Rotation on QI-HBB Joint with Different  $e/d$  Ratio at 12.5 kN (Deformation Scale 30x)

Not only are peel stresses increased in the adhesive for shorter  $e/d$  ratios, but the stresses at the hole are also increased significantly for both QI and CP layups, as shown in Figure 65 for the QI case. The longitudinal and shear stress increase for a lower  $e/d$  ratio for both CP and QI layups. It appears that for an  $e/d$  ratio of less than 3, stress concentrations due to overlap end proximity become more significant, and this increase is mainly apparent from a change of  $e/d$  between 3 and 2. Not only does reducing the edge distance result in more peel stresses in the adhesive, but it also significantly increases stress concentrations at the hole. It is interesting to see these results as some would be tempted to decrease the edge distance to decrease peel stresses in the adhesive at the expense of increased stress concentration at the hole. However, this strategy would be detrimental to the joint, while this investigation highlights the design complexity of HBB joints.

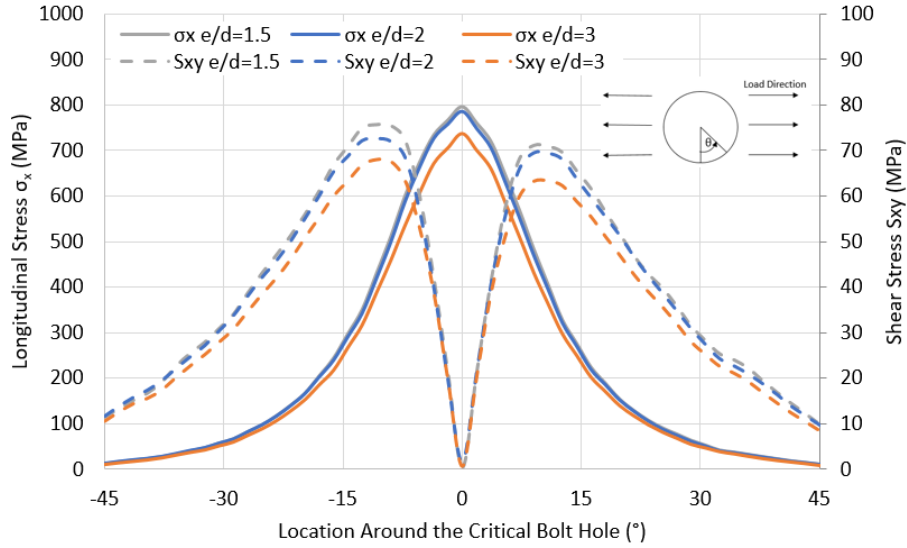


Figure 65: Tensile  $\sigma_x$  and Shear Stress  $S_{xy}$  Distribution Around the Critical Hole in QI-HBB Joints at 12.5 kN

It is observed that an  $e/d$  ratio of 3 or more will not affect the stress state at overlap ends since the stress state in the adhesive is the same as for a bonded joint, as shown in section 6.1.1. Thus, HBB joints should be designed to have an  $e/d$  ratio of 3 to be optimal regarding the stress distribution at the overlap ends in the adhesive. Still, while the  $e/d$  ratio influences the strength of HBB joints, no  $e/d$  ratio can lower the stresses in the adhesive layer of HBB joints under that of a bonded joint as, at best, the stress state compared to a purely bonded joint will remain unchanged.

#### 6.2.4 Influence of Washer Size

The study of the influence of the  $e/d$  ratio suggested that the effect of the bolt clamping is limited to the region under the washer. Initial failure can only be delayed if the bolt is positioned properly for a given washer's external diameter. Figure 66 show the compression zone for the joint tested experimentally ( $e/d=3$ ). It can be seen that the compression zone is effectively limited to the region almost directly under the washer.

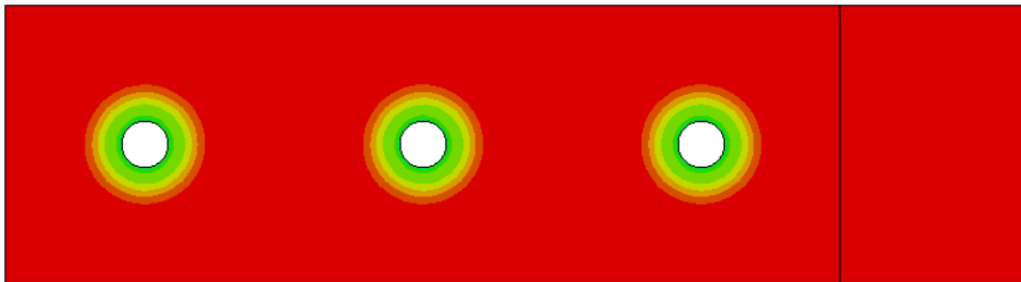


Figure 66: Effect of Bolt Clamping at the End of the Preload Application

In order to study the effect of the washer on the stresses in the adhesive and considering that it was observed that the affected region of compression is limited to the area under the washer, a configuration was analyzed for a QI12 HBB joint with an  $e/d=2$  and a washer with a diameter equivalent to twice the edge distance, as shown in Figure 67, such as the overlap end is partly covered.

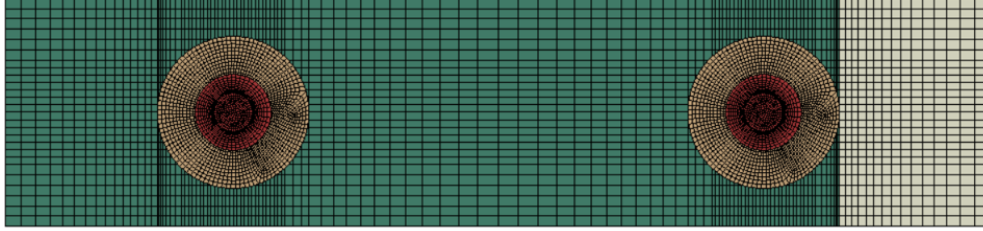


Figure 67: QI12-HBB ( $e/d=2$ ) Large Washer Configuration

This configuration was tested, and the stresses in the adhesive layer were compared with the HBB joint, with an  $e/d$  ratio of 2, but using the initial washer size. Figure 68 shows that the increase in washer size did not affect the shear stress distribution in the adhesive layer. However, a peel stress reduction of around 13% was noted for the region directly under the washer. As the washer curved away from the overlap end, the washer edge was further from the overlap ends, which reduced its effect on peel stress reduction significantly to a point where no difference can be noted between the value of peel stresses in the two joints using different washer sizes. To produce a significant impact on peel stress reduction, it was determined that the washer must be 1 mm away from the overlap ends, corresponding to a position along the Y-Axis of around 5 mm. Additionally, no peel stress reduction occurs when the washer edge is more than 2.7 mm away from the overlap ends. This highlights that to reduce peel stress in the adhesive using bolts, the clamped area must be directed at the overlap ends, or no peel stress reduction will be observed.

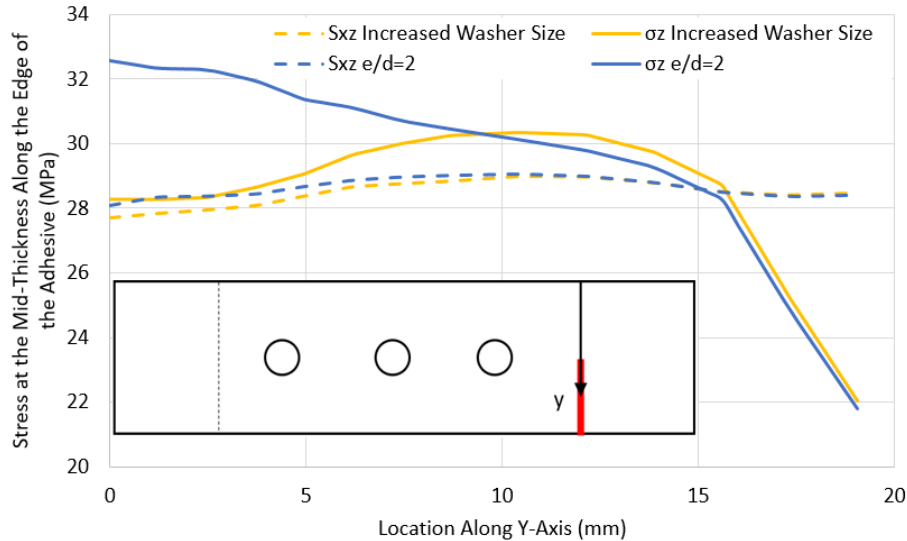


Figure 68: Peel  $\sigma_z$  and Shear  $S_{xz}$  Stresses at the Overlap End in QI-HBB Joints with Different Washer Sizes at 12.5 kN

This study highlights the fact that the clamping effect of the bolts is limited to the area under the washer. Nevertheless, this effect can be significant on damage progression and, ultimately, damage initiation if a washer is appropriately designed. In an ideal situation, the area covered by the washer should be around the bolt hole and at the overlap ends. However, doing this will most likely be at the cost of a high weight penalty. Therefore, washer designs should be developed to focus the clamping action at the overlap ends while maintaining a  $e/d$  ratio of 3 and optimizing for weight. It is expected that, even without clamping load in the vicinity of the holes, cracks will be

drawn towards the stress-concentrated regions (the holes). This would still slow their propagation compared to a bonded joint where cracks can freely progress in any direction without being slowed.

## 7. Conclusions

A finite element investigation of the mechanics of hybrid bolted/bonded joints was carried out by analyzing the stresses in the critical regions of the joint. It was identified that the stresses were concentrated at the hole closer to the grip side in the laminates and at the overlap ends in the adhesive. HBB joints can carry significantly more load than 3OB joints when considering the first significant failure event (fibre and adhesive damage initiation). An improvement of 76.8% was noted for CP layups and 52.8 % for QI layups, mainly attributed to the shear stress reduction provided by the adhesive. However, the HBB joint's maximum strength potential is limited to the bonded joint strength as the stresses in the adhesive layer are the same for bonded and HBB joints. For longer overlap lengths typically requiring more than two bolts, it was identified that the middle bolts did not contribute to increasing the strength of the HBB joints since the critical regions are at the overlap ends. QI layups were identified as having higher stresses in the adhesive for the same load level than CP layups, leading to a lower HBB joint strength due to their lower stiffness allowing greater peel stresses and greater laminate relative displacement, increasing shear stresses.

A demonstration of the effect of the choice of adhesive on the load-sharing potential of an HBB joint was done, highlighting the fact that a low modulus, highly plastic deformable adhesive was required to achieve such load-sharing as a high level of plastic deformation must occur to have significant hole overclosure. The overlap length also proved to affect the load-sharing potential of HBB joints as longer overlap lengths delay adhesive plastic behaviour, which in turn delays the moment of significant hole overclosure. Still, even though lower overlap lengths displayed higher hole overclosure at lower load levels, the interval between the high overclosure and adhesive damage initiation remained similar. Also, QI layups appeared to be more promising at achieving load-sharing as they contribute to higher hole overclosure. This was observed as the longitudinal hole deformation for QI layups is less than in CP layups, and the relative displacement between the laminates is greater for QI layups, allowing greater hole overclosure. The laminate thickness increase also contributes to an increase in the hole overclosure due to the higher stresses caused by the increase in load eccentricity triggering plasticity. Ultimately, these results showed that it is challenging to achieve simultaneous load-sharing between the bolts and the adhesive, and as such other ways of optimizing HBB joints should be explored.

The investigation on HBB joints was continued to find parameters that could optimize HBB joints using a stiff adhesive since load-sharing is difficult to achieve even with a plastically deformable adhesive. The effect of the  $e/d$  ratio and the washer size were studied for that matter. A decrease in the  $e/d$  ratio led to increased peel stresses in the adhesive. The change in the  $e/d$  ratio affected the natural shape of the undulation of the joint since the bolts influence the OPD of the joint. Thus, having the bolts closer to the overlap ends produced higher peel stresses in the adhesive layer due to the bolt's rotation. This also suggested that the effect of the clamping was limited to the region under the washer, which was verified by varying the washer size. The washer size was increased to cover parts of the overlap ends, and it was found that to have a significant peel stress reduction, the washer had to be 1 mm away from the overlap ends at most. This confirms that the effect of the preload is limited to the region under the washer. Also, the washer size increase did not affect the shear stresses developing in the adhesive layer.

## 7.1 Limitations

The FEA models considered a perfect adhesive with no initial flaws. Thus, the study did not consider cracks initiating from flaws before high stresses develop in the adhesive. Cracks seem to have a significant impact on bonded joints, while in HBB joints, they appear to have a less detrimental effect. This limitation prevents to conclude on whether damage initiation or propagation in the adhesive is more detrimental to the joint's performance. Still, this phenomenon was taken into consideration when discussing the influence of the various design parameters. Also, the material model has not considered an important failure mode. Delamination may occur, especially in the ply next to the adhesive in bonded and HBB joints. Due to the lack of available data, this phenomenon was not included, but this failure mode may represent a design limit in those joints. Still, the absence of delamination did not seem to influence the joint behaviour and ultimate strength when compared to experimental results. Additionally, a proper estimation of shear stresses in the adhesive layer was impossible as the spew fillet was not modelled. Researcher focused on this feature, and determined that the spew fillet reduced the shear stresses at the overlap ends [65]. Yet, even though the model did not capture the shear stress reduction effect, all configurations were compared for an adhesive without spew fillets which makes them similarly affected, making a comparison possible between configurations.

## 7.2 Recommendations

According to the quasi-static analysis performed, although significant, the role of the bolt assemblies in HBB joints compared to bonded joints is limited to a crack-arresting feature. Still, this advantage is significant as displayed by many experimental investigations, which indicates that HBB joint should be more widely used as an alternative to bolted and bonded joints, especially when thin laminates are used and joints are highly loaded. This advantage may become even more significant in other regimes such as under fatigue conditions but also impact.

It would be interesting to do a finite element analysis studying the joint behaviour in fatigue when the adhesive has fully plasticized in HBB joints, which is required to achieve load-sharing. Under static loading, the plasticization of the adhesive layer helped achieve load-sharing between the bolts and the adhesive. However, during repetitive load cycles, the plastic deformation in the adhesive may be detrimental to the joint's strength and reduce its fatigue life. Therefore, a change in load-sharing initiation may also be noted when the adhesive is initially fully plasticized. Additionally, the addition of initial flaws in the model would allow researchers to focus on the effect of delaying damage initiation and damage progression. This study monitored damage initiation as the adhesive was assumed to be perfect. However, in real-life applications, tiny flaws in the adhesive layer can be present, and cracks will initiate from them, maybe even before adhesive damage initiation at the overlap ends. Thus, these cracks may be more concerning than adhesive damage initiation, but only a proper understanding of the effect of adhesive damage initiation and progression will permit a proposition on the design requirements for HBB joints.

Additionally, impact is a regime of concern with composite laminates. Even low energy impacts can lead to barely visible damage in laminates. This concern may extend to the joint configuration where degradation of the adhesive or the adhesive-laminate interface could be affected by damage caused by impact. Thus, an impact analysis of HBB joints would be interesting to capture the effect of sudden damage initiation on the integrity of the joint configuration under such loading conditions. The scope of such study may also consider suddenly applied loading which may also cause similar concerns for HBB joints.

# References

- [1] A. Baker S. Dutton D. Kelly. *Composite Materials for Aircraft Structures*. Second edition. American Institute of Aeronautics and Astronautics, 2004.
- [2] Agung Efriyo Hadi, Mohammad Hazim Mohamad Hamdan, Januar Parlaungan Siregar, Ramli Junid, Cionita Tezara, Agustinus Purna Irawan, Deni Fajar Fitriyana, and Teuku Rihayat. Application of micromechanical modelling for the evaluation of elastic moduli of hybrid woven jute-ramie reinforced unsaturated polyester composites. *Polymers*, 13(15):2572, Aug 2021.
- [3] Usman Ahmed, Asra Tariq, Yasir Nawab, Khubab Shaker, Zubair Khaliq, and Muhammad Umair. Comparison of mechanical behavior of biaxial, unidirectional and standard woven fabric reinforced composites. *Fibers and Polymers*, 21(6):1308–1315, Jun 2020.
- [4] Antonio J. Gamez, Severo R. Fernandez-Vidal, Alvaro Gomez-Parra, Pedro F. Mayuet, and Ana P. Valerga. Mechanical joining of stacks. In Dermot Brabazon, editor, *Encyclopedia of Materials: Composites*, pages 403–419. Elsevier, Oxford, 2021.
- [5] Sadik Omairey, Nithin Amirth Jayasree, and Mihalis Kazilas. Defects and uncertainties of adhesively bonded composite joints. *SN Applied Sciences*, 3, 09 2021.
- [6] G. Jeevi, Sanjay Kumar Nayak, and M. Abdul Kader. Review on adhesive joints and their application in hybrid composite structures. *Journal of Adhesion Science and Technology*, 33(14):1497–1520, 2019.
- [7] Farid Gamdani, Rachid Boukhili, and Aurelian Vadean. Tensile behavior of hybrid multi-bolted/bonded joints in composite laminates. *International Journal of Adhesion and Adhesives*, 95:102426, 2019.
- [8] Masoud Mehrabian and Rachid Boukhili. 3d-dic strain field measurements in bolted and hybrid bolted-bonded joints of woven carbon-epoxy composites. *Composites Part B: Engineering*, 218:108875, 2021.
- [9] Kobyé Bodjona, Sean Fielding, Mohammad Heidari-Rarani, and Larry Lessard. Effect of adhesive layer compliance on strength of single-lap hybrid bonded-bolted joints. *Composite Structures*, 261:113324, 2021.
- [10] Gordon Kelly. Load transfer in hybrid (bonded/bolted) composite single-lap joints. *Composite Structures*, 69(1):35–43, 2005.
- [11] Gordon Kelly. Quasi-static strength and fatigue life of hybrid (bonded/bolted) composite single-lap joints. *Composite Structures*, 72(1):119–129, 2006.
- [12] Kobyé Bodjona and Larry Lessard. Load sharing in single-lap bonded/bolted composite joints. part ii: Global sensitivity analysis. *Composite Structures*, 129:276–283, 2015.
- [13] E. Armentani, M. Laiso, F. Caputo, and R. Sepe. Numerical fem evaluation for the structural behaviour of a hybrid (bonded/bolted) single-lap composite joint. *Procedia Structural Integrity*, 8:137–153, 2018. AIAS2017 - 46th Conference on Stress Analysis and Mechanical Engineering Design, 6-9 September 2017, Pisa, Italy.
- [14] Valentin S. Romanov, Mohammad Heidari-Rarani, and Larry Lessard. A parametric study on static behavior and load sharing of multi-bolt hybrid bonded/bolted composite joints. *Composites Part B: Engineering*, 217:108897, 2021.
- [15] Pedro Lopez-Cruz, Jeremy Laliberté, and Larry Lessard. Investigation of bolted/bonded composite joint behaviour using design of experiments. *Composite Structures*, 170:192–201, 2017.
- [16] George H. Staab. 6 - laminate analysis. In George H. Staab, editor, *Laminar Composites (Second Edition)*, pages 189–284. Butterworth-Heinemann, second edition edition, 2015.
- [17] NPTEL. Module 5: Laminate theory. <https://nptel.ac.in/content/storage2/courses/>



- 
- [101104010/downloads/Lecture16.pdf](#). Online, accessed 13 December 2021.
- [18] P. Camanho L. Tong. *Composite joints and connections; Principles, modelling and testing*. Woodhead Publishing, 2011.
- [19] V.G. Belardi, P. Fanelli, and F. Vivio. Analysis of multi-bolt composite joints with a user-defined finite element for the evaluation of load distribution and secondary bending. *Composites Part B: Engineering*, 227:109378, 2021.
- [20] V Lawlor, Walter Stanley, and Michael McCarthy. Characterisation of damage development in bolted composite joints. 04 2001.
- [21] Rikard Heslehurst and L.J. Hart-Smith. The science and art of structural adhesive bonding. *SAMPE Journal*, 38:60–71, 03 2002.
- [22] Georges Fourche. An overview of the basic aspects of polymer adhesion. part i: Fundamentals. *Polymer Engineering and Science*, 35:957–967, 1995.
- [23] G. Dillingham L. C. Dorworth. Fundamentals of Adhesive Bonding of Composite Materials. <https://www.aerodefevent.com/wp-content/uploads/2017/03/AeroDef-2017-Fundamentals-of-Adhesive-Bonding-of-Composite-Materials.pdf>, 2017. Online, accessed 19 August 2020.
- [24] Ana Loureiro, L.F.M. Silva, Chiaki Sato, and Miguel de Figueiredo. Comparison of the mechanical behaviour between stiff and flexible adhesive joints for the automotive industry. *Journal of Adhesion - J ADHES*, 86:765–787, 07 2010.
- [25] G. Kolks and K.I. Tserpes. Efficient progressive damage modeling of hybrid composite/titanium bolted joints. *Composites Part A: Applied Science and Manufacturing*, 56:51–63, 2014.
- [26] Jinxin Ye, Ying Yan, Jie Li, Yang Hong, and Ziyang Tian. 3d explicit finite element analysis of tensile failure behavior in adhesive-bonded composite single-lap joints. *Composite Structures*, 201:261–275, 2018.
- [27] MIT. Choosing between implicit and explicit analysis. <https://abaqus-docs.mit.edu/2017/English/SIMACAEGSARefMap/simagsa-c-absadvexp.htm>. Online, accessed 10 November 2021.
- [28] B. Egan, M.A. McCarthy, R.M. Frizzell, P.J. Gray, and C.T. McCarthy. Modelling bearing failure in countersunk composite joints under quasi-static loading using 3d explicit finite element analysis. *Composite Structures*, 108:963–977, 2014.
- [29] Simulia. Abaqus version 6.6 documentation. <https://classes.engineering.wustl.edu/2009/spring/mase5513/abaqus/docs/v6.6/books/usb/default.htm?startat=pt06ch21s01aus90.html>. Online, accessed 10 November 2021.
- [30] Feixia Pan, Jiansen Zhu, Antti O. Helminen, and Ramin Vatanparast. Three point bending analysis of a mobile phone using ls-dyna explicit integration method. 2006.
- [31] Abaqus. Contact modeling. <http://ftp.demec.ufpr.br/disciplinas/TM738/14-contact.pdf>. Online, accessed 15 September 2021.
- [32] Bibekananda Mandal and Anupam Chakrabarti. Numerical failure assessment of multi-bolt frp composite joints with varying sizes and preloads of bolts. *Composite Structures*, 187:169–178, 2018.
- [33] Haris A. Khan, Abid Hassan, M.B. Saeed, Farrukh Mazhar, and Imran A. Chaudhary. Finite element analysis of mechanical properties of woven composites through a micromechanics model. *Science and Engineering of Composite Materials*, 24(1):87–99, 2017.
- [34] Ch. Hochard, P.-A. Aubourg, and J.-P. Charles. Modelling of the mechanical behaviour of woven-fabric cfrp laminates up to failure. *Composites Science and Technology*, 61(2):221–230, 2001.
- [35] Xiaofan Zhang, Yanrong Xiao, Christopher S. Meyer, Daniel J. O’Brien, and Somnath Ghosh. Impact damage modeling in woven composites with two-level parametrically-upscaled continuum damage mechanics models (pucdm). *Composites Part B: Engineering*, page 109607, 2022.

- [36] Yanneck Wielhorski, Arturo Mendoza, Marcello Rubino, and Stéphane Roux. Numerical modeling of 3d woven composite reinforcements: A review. *Composites Part A: Applied Science and Manufacturing*, 154:106729, 2022.
- [37] Jiaying Gao, Modesar Shakoor, Gino Domel, Matthias Merzkirch, Guowei Zhou, Danielle Zeng, Xuming Su, and Wing Kam Liu. Predictive multiscale modeling for unidirectional carbon fiber reinforced polymers. *Composites Science and Technology*, 186:107922, 2020.
- [38] G. Giuntoli. Hybrid cpu/gpu implementation for the fe2 multi-scale method for composite problems. 2020.
- [39] S. Gordon. Tolérance aux dommages des matériaux composites aéronautiques. 2008. Thèse de doctorat, École Polytechnique de Montréal.
- [40] Y. Thollon and C. Hochard. A general damage model for woven fabric composite laminates up to first failure. *Mechanics of Materials*, 41(7):820–827, 2009.
- [41] Marjorie Jauffret, Aldo Cocchi, Naïm Naouar, Christian Hochard, and Philippe Boisse. Textile Composite Damage Analysis Taking into Account the Forming Process. *Materials*, 13(23):5337, 2020.
- [42] Y. Shi, T. Swait, and C. Soutis. Modelling damage evolution in composite laminates subjected to low velocity impact. *Composite Structures*, 94(9):2902–2913, 2012.
- [43] 900GPa. Worldwide hub for composite materials. <https://www.900gpa.com/en>. Online, accessed 10 June 2021.
- [44] Boling He and Yingguang Pan. Failure mechanism of single lap, adhesively bonded composite-titanium joints subjected to solid projectile impact. *Journal of Adhesion Science and Technology*, 0(0):1–22, 2021.
- [45] John Wang, Evan Pineda, V Ranatunga, and SS Smeltzer. 3d progressive damage modeling for laminated composite based on crack band theory and continuum damage mechanics. 09 2015.
- [46] Andrea Gilioli, Andrea Manes, and Marco Giglio. Evaluation of the effects of the numerical modelling choices on the simulation of a tensile test on cfrp composite. *Procedia Structural Integrity*, 8:33–42, 01 2018.
- [47] Kobyé Bodjona, Karthik Raju, Gyu-Hyeong Lim, and Larry Lessard. Load sharing in single-lap bonded/bolted composite joints. part i: Model development and validation. *Composite Structures*, 129:268–275, 2015.
- [48] M.Z. Sadeghi, J. Weiland, A. Preisler, J. Zimmermann, A. Schiebahn, U. Reisgen, and K.U. Schroeder. Damage detection in adhesively bonded single lap joints by using backface strain: Proposing a new position for backface strain gauges. *International Journal of Adhesion and Adhesives*, 97:102494, 2020. Special issue on Joint design.
- [49] J. Weiland, M.Z. Sadeghi, J.V. Thomalla, A. Schiebahn, K.U. Schroeder, and U. Reisgen. Analysis of back-face strain measurement for adhesively bonded single lap joints using strain gauge, digital image correlation and finite element method. *International Journal of Adhesion and Adhesives*, 97:102491, 2020. Special issue on Joint design.
- [50] S. Sugiman, A.D. Crocombe, and I.A. Aschroft. Modelling the static response of unaged adhesively bonded structures. *Engineering Fracture Mechanics*, 98:296–314, 2013.
- [51] John Tomblin, Waruna p. Seneviratne, Paulo Escobar, and Yap Yoon-Khian. Shear stress-strain data for structural adhesives. 2002.
- [52] Nader Fanaie, Farzaneh Ghalamzan Esfahani, and Soheil Soroushnia. Analytical study of composite beams with different arrangements of channel shear connectors. *Steel and Composite Structures*, 19:485–501, 08 2015.
- [53] 2 - finite element analysis of beams. In Xiaoshan Lin, Y.X. Zhang, and Prabin Pathak, editors, *Nonlinear Finite Element Analysis of Composite and Reinforced Concrete Beams*, Woodhead Publishing Series in Civil and Structural Engineering, pages 9–27. Woodhead Publishing, 2020.

- [54] Farid Gamdani, Rachid Boukhili, and Aurelian Vadean. Tensile strength of open-hole, pin-loaded and multi-bolted single-lap joints in woven composite plates. *Materials Design*, 88:702–712, 2015.
- [55] R. Budynas. *Shigley’s Mechanical Engineering Design*. McGraw-Hill series in mechanical engineering. McGraw-Hill Higher Education, 2014.
- [56] Peifei Xu, Zhengong Zhou, Tianzhen Liu, Shidong Pan, Xiaojun Tan, Shiming Zu, and Yanfeng Zhang. Propagation of damage in bolt jointed and hybrid jointed glare structures subjected to the quasi-static loading. *Composite Structures*, 218:79–94, 2019.
- [57] Brendan O’Toole, Kumarswamy Karpanan, and Masoud Feghhi. *Experimental and Finite Element Analysis of Preloaded Bolted Joints Under Impact Loading*.
- [58] A. J. Lakis. Experimental and analytical stress and strain characterization of notched composite plates. 2020. Mémoire de maîtrise, École Polytechnique de Montréal.
- [59] Masoud Mehrabian and Rachid Boukhili. Quantifying of secondary bending effect in multi-bolt single-lap carbon-epoxy composite joints via 3d-dic. *Composites Science and Technology*, 200:108453, 2020.
- [60] Dantec Dynamics. Measurement principles of dic. <https://www.dantecdynamics.com/solutions-applications/solutions/stress-strain-espi-dic/digital-image-correlation-dic/measurement-principles-of-dic/>. Online, accessed 02 February 2022.
- [61] Wenbin Huang, Xiang Yan, Seol Ryung Kwon, Shujun Zhang, Fuh-Gwo Yuan, and Xiaoning Jiang. Flexoelectric strain gradient detection using ba0.64sr0.36tio3 for sensing. *Applied Physics Letters*, 101(25):252903, 2012.
- [62] Lotfi Toubal, Moussa Karama, and Bernard Lorrain. Stress concentration in a circular hole in composite plate. *Composite Structures*, 68(1):31–36, 2005.
- [63] Kobyé Bodjona and Larry Lessard. Hybrid bonded-fastened joints and their application in composite structures: A general review. *Journal of Reinforced Plastics and Composites*, 35(9):764–781, 2016.
- [64] L.J. Hart-Smith. Mechanically fastened joints for advanced composites - phenomenological considerations and simple analyses. <http://pdf-s3.xuebalib.com:1262/ou7YjVePFGH.pdf>, 1980. Online, accessed 12 July 2021.
- [65] Salih Akpınar, Muhammet Onur Doru, Adnan Özel, Murat Demir Aydın, and Hamed Ghafarzadeh Jahanpasand. The effect of the spew fillet on an adhesively bonded single-lap joint subjected to bending moment. *Composites Part B: Engineering*, 55:55–64, 2013.
- [66] T.R.C. Chuaqui, M.W.D. Nielsen, J. Colton, R. Butler, and A.T. Rhead. Effects of ply angle and blocking on open-hole tensile strength of composite laminates: A design and certification perspective. *Composites Part B: Engineering*, 207:108582, 2021.
- [67] MIT. Total energy output. <https://abaqus-docs.mit.edu/2017/English/SIMACAEOUTRefMap/simaout-c-exp-totalenergyoutput.htm>. Online, accessed 27 April 2021.

# A. Appendix

## A.1 Model Validation

In order to verify that the sub-routine contains no error and is well implemented in Abaqus, some validation steps are done by comparing the tensile behaviour to what is predicted by the CLT. A 3D FEA model was developed using the same VUMAT and modelling strategies used for the other geometries in the report. A CP laminate with a stacking sequence of  $[0^\circ/90^\circ/0^\circ/90^\circ]_s$  and a QI laminate  $[\pm 45^\circ/0^\circ/90^\circ]_s$  with the material properties shown in Table 15 are used for the subroutine validation. The geometry of the laminates is shown in Figure 69.

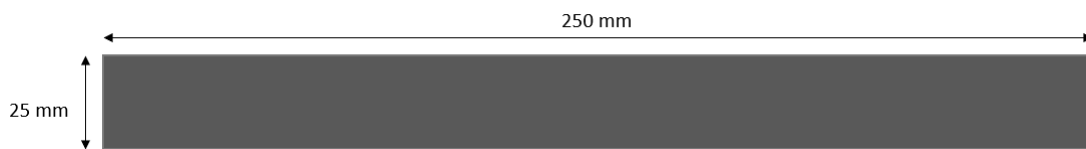


Figure 69: FEA Specimens Geometry Used for the Comparison with the CLT

Table 15: Ply properties of AS4/8552 unidirectional prepreg [66]

Property	Units	Value
$t_p$	mm	0.195
Density	kg/m <sup>3</sup>	1800
$E_1$	GPa	137.1
$E_2=E_3$	GPa	8.8
$G_{12}=G_{13}=G_{23}$	GPa	4.9
$\nu_{12}=\nu_{13}$	-	0.314
$\nu_{23}$	-	0.487

Table 16: Predicted Material Properties Using CLT

Property	Units	Value	
		CP	QI
Layup			
$E_x$	GPa	73.31	52.65
$E_y$	GPa	73.31	52.65
$G_{xy}$	GPa	4.9	20.11
$\nu_{xy}$	-	0.0379	0.3091

The stress-strain curves for the CP and QI laminates are shown in Figure 70. The FEA models accurately predicted the laminate longitudinal stiffness when compared to the CLT. A discrepancy of 0.6% for the CP model and 0.04% for the QI model on the initial longitudinal modulus was observed. This result indicates that the VUMAT is providing good results and that the models properly capture the effect of varying ply angles.

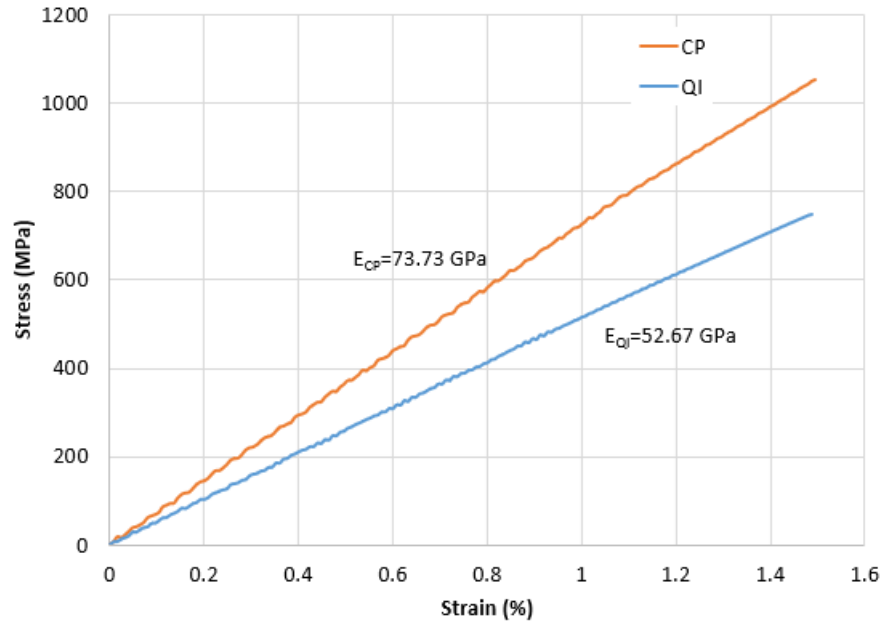


Figure 70: Stress-Strain Curve For Different Layups Under Tensile Loading

## A.2 Abaqus Energy Outputs

Below you will find a list of the energy outputs monitored during the simulation along with their respective definitions [67].

- ALLAE: “Artificial” strain energy associated with constraints used to remove singular modes (such as hourglass control) and with constraints used to make the drill rotation follow the in-plane rotation of the shell elements.
- ALLCD: Energy dissipated by viscoelasticity. (Not supported for hyperelastic and hyperfoam material models with linear viscoelasticity.)
- ALLIE: Total strain energy. ( $ALLIE = ALLSE + ALLPD + ALLCD + ALLAE + ALLDMD + ALLDC + ALLFC$ .)
- ALLKE: Kinetic energy.
- ALLPD: Energy dissipated by rate-independent and rate-dependent plastic deformation.
- ALLSE: Recoverable strain energy.
- ALLDMD: Energy dissipated by damage.
- ALLDC: Energy dissipated by distortion control.
- ALLFC: Fluid cavity energy, defined as the negative of the work done by all fluid cavities. (Available only for the whole model.)

### A.3 Mesh Convergence Studies

Mesh convergence study is a crucial part of any finite element analysis. It ensures that the level of discretization is high enough to achieve reliable results of a continuum model. A convergence study was performed for the various models studied in this Thesis. The convergence was monitored in terms of the load at which tensile fibre damage initiation occurs.

#### A.3.1 OHT

For the OHT models, it was found that convergence was achieved for the same mesh independently of the layup. Mesh refinement occurred around the hole, where high stress gradient was observed. The results converged for a mesh size at the hole of 0.002 mm, as shown in Figure 71.

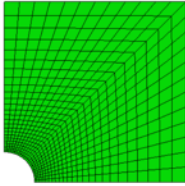
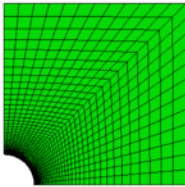
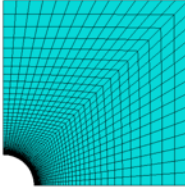
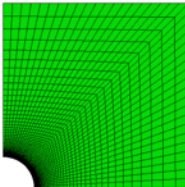
Minimum Element Size (mm)	Load at Fiber Damage Initiation (kN)	Mesh
0.2	16.57	
0.02	12.65	
0.002	10.97	
0.001	10.85	

Figure 71: Mesh Convergence Study for OHT Models

#### A.3.2 OB and HBB Joints

For the 3OB and HBB joints, it was determined that the mesh did not have to be refined around the bolt hole, as this was done during the OHT mesh convergence study. However, due to the presence of the adhesive in HBB joints, high stresses develop at the overlap ends. Therefore, the mesh had to be refined at this location to capture this high stress gradient. In the case of HBB joints, the mesh convergence study was monitored for the cohesive damage initiation, a function of the stress state at the adhesive cohesive interaction interface. As every layup has the same geometry, the mesh convergence study was only performed for the CP12 layup, and the converged mesh was used for all models. The mesh convergence study for HBB joints is shown in Table 17.

Table 17: Mesh Convergence Study at The Overlap Ends in HBB Joints

Element Size	Applied Load at Damage Initiation (kN)	Difference (%)
0.845	18.93	16.0
0.420	16.33	4.1
0.280	15.68	0.8
0.140	15.56	

## A.4 Model Energies

As mentioned in Section 4.2, since Abaqus/Explicit is used to run these simulations, the internal and the kinetic energies must be monitored. Therefore, the simulation results can only be considered reliable if the kinetic energy (ALLKE) is kept under 5% of the internal energy (ALLIE) throughout the simulation. This would indicate that no dynamic phenomenon impacts the quasi-static simulation.

### A.4.1 OHT

For the OHT models, very low levels of kinetic energies are observed, as shown in Figure 72a and 72b for CP and QI layups respectively, meaning the results are unaffected by kinematic effects induced by mass scaling. Kinetic energy is low mainly because the model is very stable as it is composed of one part only.

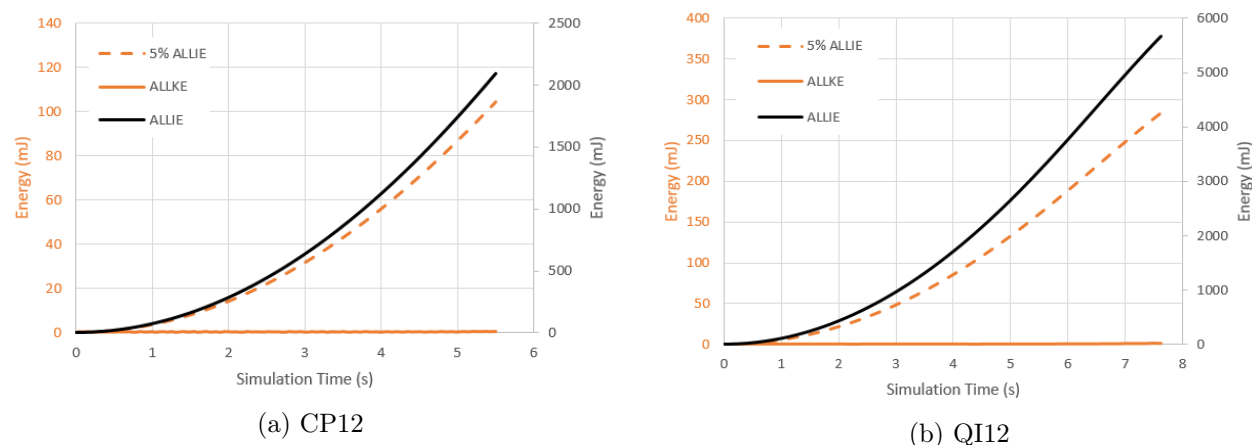


Figure 72: Energy Monitoring in OHT Models

### A.4.2 3OB Joints

For the 3OB joint models, the kinematic energy remained relatively low (under 5% of ALLIE) as shown in Figure 73a and 73b for CP and QI layups respectively. It is observed that while kinematic energy remained low, it is higher for 3OB joint models than for OHT models. This is attributed to the contacts taking place in the bolted joints, causing more movement in the model. This is shown by the increase in kinetic energy, which is located at the moment when contact is initiated with the bolts. Also, at the end of the simulation, a drastic increase in kinetic energy is observed as extensive damage occurs in the laminate making the assembly slightly unstable. QI models display much more kinetic energy than CP layups as they have more mass due to the full-width representation of the geometry when using the QI layup. Since the kinematic energy remained this low throughout the simulation, it can be concluded that the results are unaffected by kinematic effects induced by mass scaling.



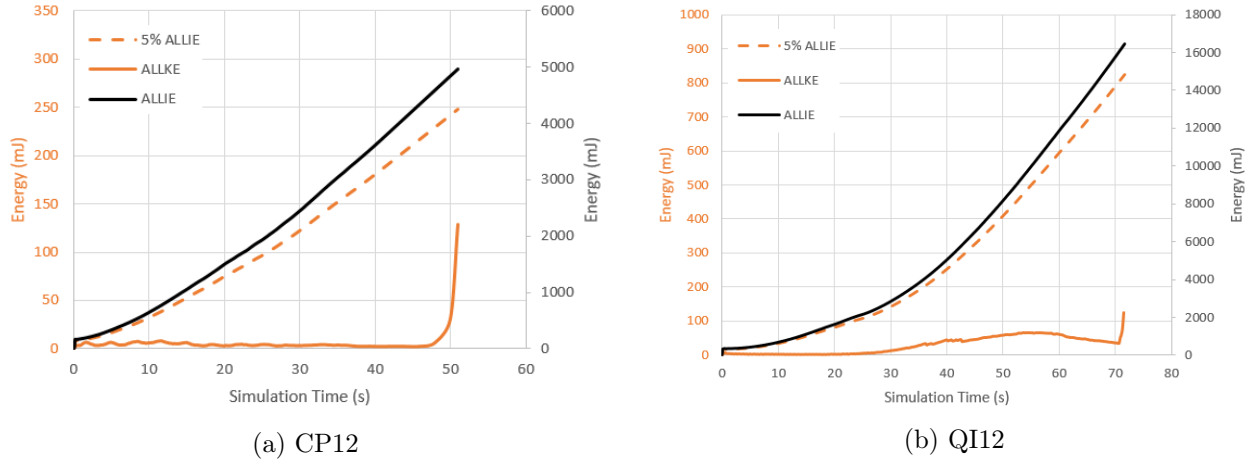


Figure 73: Energy Monitoring in 3OB Joints Models

### A.4.3 HBB Joints

For the HBB joints model, kinetic energy was not problematic as the adhesive layer made the joint very stable by keeping the two laminates stuck with each other. Figure 74a and 74b show the energies throughout the simulation in HBB joints. For the HBB joint configuration, the respective energy levels are similar to that of the OHT models, where higher assembly stability is observed.

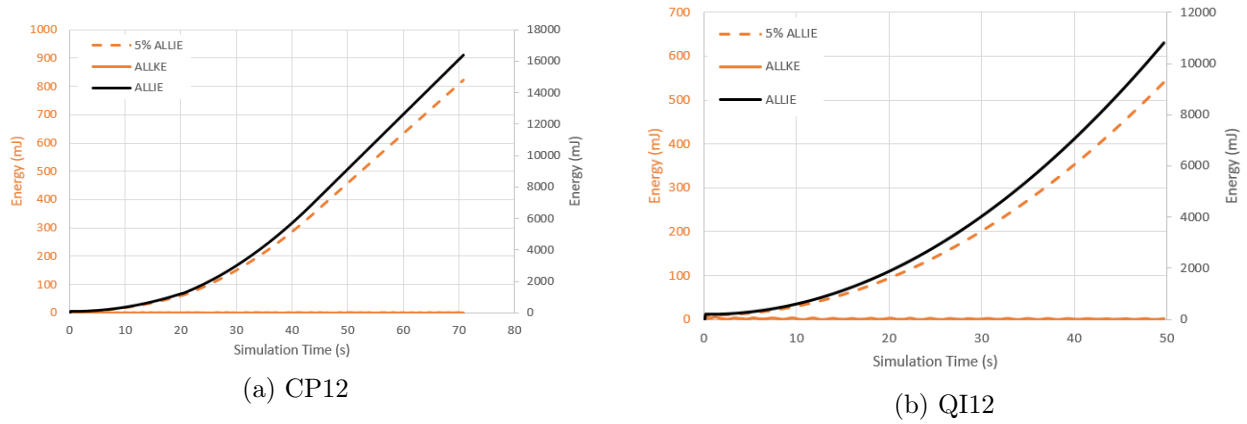


Figure 74: Energy Monitoring in HBB Joints Models